2015

Reconfigurable photonic crystal

Depeng Mao
Iowa State University

Reconfigurable photonic crystal

by

Depeng Mao

A dissertation submitted to the graduate faculty

in partial fulfillment of the requirements for the degree of

DOCTOR OF PHILOSOPHY

Major: Electrical Engineering

Program of Study Committee:
Liang Dong, Major Professor
Jiming Song
Santosh Pandey
Sumit Chaudhary
Tim Bigelow

Iowa State University

Ames, Iowa

2015

TABLE OF CONTENTS

NOMENCLATURE

BOE	Buffered Oxide Etch
DBR	Distributed Bragg Reflectors
DMD	Digital Micromirror Devices
FDTD	Finite Difference Time Domain
FWHM	Full Width Half Maximum
IC	Integrated Circuit
LC	Liquid Crystal
MEEP	MIT Electromagnetic Equation Propagation
MEMS	Microelectromechanical Systems
MPB	MIT Photonic-Bands
OSA	Optical Spectrum Analyzer
PC	Photonic Crystal
PC^3	Photonic Crystal-cantilever Cavity
PML	Perfectly Matched Layer
PMMA	Poly(methyl methacrylate)
PWE	Plane-wave Expansion
RIE	Reactive Ion Etching
SEM	Scanning Electron Microscope
SOI	Silicon on Insulator
SWN	Subwavelength Nanostructure
TIR	Total Internal Reflection

ACKNOWLEDGMENT

This thesis summarizes my research work during my graduate study in Iowa State University. I would like to take the time to thank the people who guided, instructed and supported me during this process.

Firstly and foremost, I want to give my deep gratitude to my advisor, Dr. Liang Dong. It was great fortune to have him as my advisor who shares his insight and patience. Secondly, I owe my deep gratitude to Dr. Jiming Song, who always takes his time to have discussions with me about my confusion in research. Meanwhile, I am also deeply grateful to other professors who are on my committee, Dr. Santosh Pandey, Dr. Sumit Chaudhary and Dr. Tim Bigelow for their time and efforts spent on my work.

Special thanks are given to Dr. Gray Tuttle, Dr. Wai Leung and Robert Mayer in Microelectronics Research Center for their trainings and help about fabrication processes. Also it was wonderful and inspiring time working with the colleagues in Laboratory for MEMS & Lab-Chips: Peng Liu, Qiugu Wang, Zhen Xu, Huawei Jiang, Xuan Qiao and Yueyi Jiao.

Last but not least, I want to thank my parents, who take my progress as their most important thing. I could not express my gratitude for their love and support with words. I also thank my wife Xiaofeng and my son Andy for their support, encouragement and persistent love.

ABSTRACT

Tunability and programmability are highly demanded for silicon photonic integrated circuits (PICs) to expand their applications in the next-generation photonics. The main objective of this thesis is to develop several reconfigurable and programmable photonic crystal (PC) devices.

In Chapter 2, we developed a relatively general nanofabrication process for integrating PC devices with movable mechanical components on silicon-on-insulator (SOI) wafers. We also investigated grating coupling technology, to facilitate coupling lights into and out of PC devices.

In Chapter 3, we developed an all-optical programmable PC device that integrates digital micromirror device (DMD), photo-responsive LC, and PC technologies. We demonstrated the functionality and programmability of the device, by forming a point-defect cavity, a straight waveguide, and a waveguide bend on the single device.

In Chapter 4, we developed two types of reconfigurable PC devices by leveraging the strengths of optical nanobeam and nano-electro-mechanical systems (NEMS) technologies. The first device consists of an array of movable nanobeams. Each nanobeam is an electrostatically tunable photonic element in a PC waveguide. We demonstrated the capability of the device to engineer different photonic bandgaps, by tuning one unit in group of two neighboring nanobeam units, tuning one or two in group of three units, and forming two reconfigurable PCs, on the single device. To achieve a higher-level integration, we also theoretically studied another reconfigurable PC integrating an array of mechanical tunable nanobeams with an array of fixed pillars into the top silicon layer of a SOI wafer.

In Chapter 5, we developed two tunable photonic crystal-cantilever cavity (PC^3) resonators. The first device has an NEMS cantilever embedded into a L6 cavity in a PC slab. The second device has a similar cantilever to insert into a nanobeam-base waveguide. We studied bending characteristics of the cantilever and optical characteristics of these two devices at different applied voltages.

In Chapter 6, we conducted theoretical investigation on a nano-opto-mechanical reconfigurable PIC device consisting of an array of silicon plugs and a 2D PC slab. We theoretically demonstrated that a point-defect cavity, a line-defect waveguide, and a waveguide bend can be configured in the PC slab, by inserting different plugs into an air hole, a straight line of holes, and an L-shape line of holes.

CHAPTER 1. INTRODUCTION TO PHOTONIC CRYSTAL

1.1 Background

One of the greatest technological innovations in the twentieth century is electronic integrated circuit (IC). During the last three decades, the outcome of Moore's law as the reduction in feature sizes of electronic devices continued to lead to denser and faster electronic circuits. However, many challenges emerge as we continue to shrink device dimensions further. In particular, due to the high power consumption and electromagnetic interference (EMI), metal interconnects pose a fundamental problem for the next generation of electronic circuits [1].

In recent years, silicon photonics has become an attractive alternative to electronics due to the advantages of information processing in optical domain [2-3]. High-speed photonic ICs [4] are likely candidates to replace the standard electronic ICs. On-chip and chip-to-chip optical interconnects offer a solution to the problem of ICs and promise a higher bandwidth to keep pace with transistors, while lowering power consumption and being immune to EMI. On the other hand, the realization of optical interconnects requires the development of high-speed modulation and low power light sources, optical switches, waveguides, and their compact integration.

Fortunately, advances in semiconductor fabrication make it possible to produce nanophotonic devices that can manipulate and control the flow of light at the nanometer scale. Generally, large-scale integration silicon photonic devices are designed on the silicon-on-insulator (SOI) platform. The SOI fabrication is compatible with CMOS technology and hence is highly accurate and mature, thus leading to a robust, high yield, and reproducible

technology. SOI-based photonic integrated circuits (PICs) operate well in the telecommunication window around wavelength of 1.55 μm [5].

Silicon photonic crystals (PCs) play an important role in nanophotonics and PICs. These specially designed periodic nanostructures can be implemented by using CMOS fabrication technology [6-7]. Two-dimensional (2D) PCs often result from drilling of periodic air hole lattices or making periodic pillars in a silicon slab. This simple photonic structure can confine light in both planar and vertical directions [6]. Its optical properties can be engineered by altering the lattice geometry, introducing defects in the lattice, and changing the index contrast between the constituent materials. PC slab allows for the realization of various photonic devices, such as waveguides with sharp bends [8], spectral filters [9], add-drop multiplexers [10], and lasers [11].

In this chapter, we first introduce basic principle of PC and PC-based resonant nanocavity. Then, we discuss major simulation methods for PC design, including plane-wave expansion (PWE) and finite-difference time-domain (FDTD) methods.

1.2 Photonic Crystal Types

PC is one of the most promising platforms for optical information processing as it can enable compact and efficient photonic devices and their large-scale integration on silicon chips [6-7]. These are structures with periodic dielectric modulation on the order of the wavelength of light. Because of this periodicity, their study is analogous to the study of semiconductors in solid-state physics. The periodicity of the electronic potential in semiconductors, which is due to the regular arrangement of atoms in a lattice, gives rise to the electronic bandgaps, which are forbidden energy bands for electrons. Similarly, the

periodicity of the refractive index (dielectric constant) gives rise to photonic bandgaps, forbidden energy bands for photons.

Depending on the dimensionality of the periodicity, PCs can be classified into three types, as shown in Fig. 1.1a. One-dimensional (1D) PCs are also known as the distributed Bragg reflectors (DBRs) [12]. They have been used mostly as mirrors, particularly in vertical cavity surface emitting lasers (VCSELs) [13]. The periodicity of dielectric constant in more than one dimension was proposed by Yablonovitch [14] and John [15] in late 1980s. As shown in Fig. 1.1b, in nature butterfly wings and opals have three-dimensional periodicity. In the recent years, scientist have developed many manmade PC structures, such as PC fiber and woodpile PC (Fig. 1.1c). PC fibers utilize the photonic bandgap of 2D periodic hollow holes to confine the light propagating along the axial direction [16]. Woodpile PC structure is first proposed by scholars in the Iowa State University and Department of Energy's Ames Laboratory [17]. This structure has a complete photonic bandgap, which has been experimentally demonstrated in microwave range [17]. Although 3D PCs can control light propagation in all directions due to a complete bandgap, fabrication of these structures at the nanometer scale is significantly challenging, especially when one wants to make them work in optical or telecommunication wavelengths.

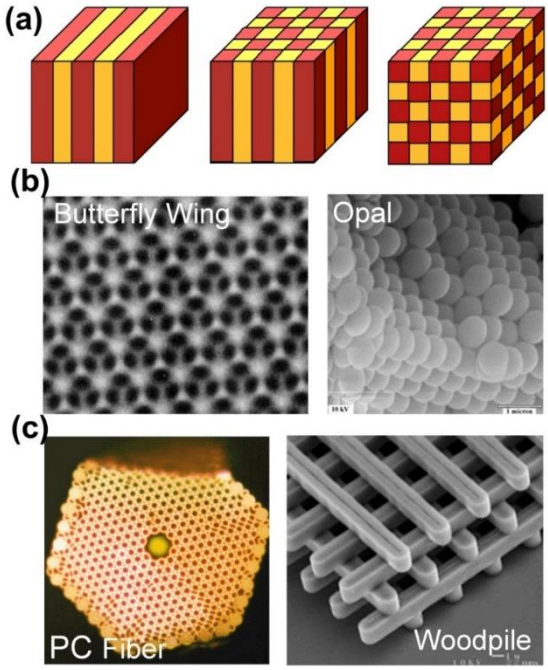

Figure 1.1 Photonic crystal structures (a) schematic (b) natural structures: butterfly wing and opal (c) manmade structures: PC fiber and woodpile.

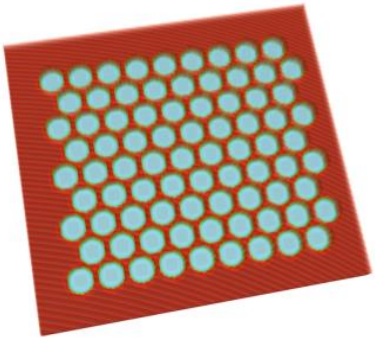

Figure 1.2 Photonic crystal slab structure with a triangular lattice.

In recent years, 2D PC structure has received significant attention. It is made in a thin semiconductor (i.e., silicon, III-V materials) slab perforated with a 2D periodic structures (such as holes), as shown in Fig. 1.2. Triangle lattice is more popular than square lattice due to its wider in-plane bandgap. Although the lattice structure is periodic in two dimensions, it has most of the important features of 3D PCs. In a PC slab, the localization of light in the vertical or thickness direction is handled by the total internal reflection (TIR), which is due to

the high index contrast between semiconductor material and air. Meanwhile, the light confinement in the planar direction is handled by in-plane photonic bandgap of the 2D lattice.

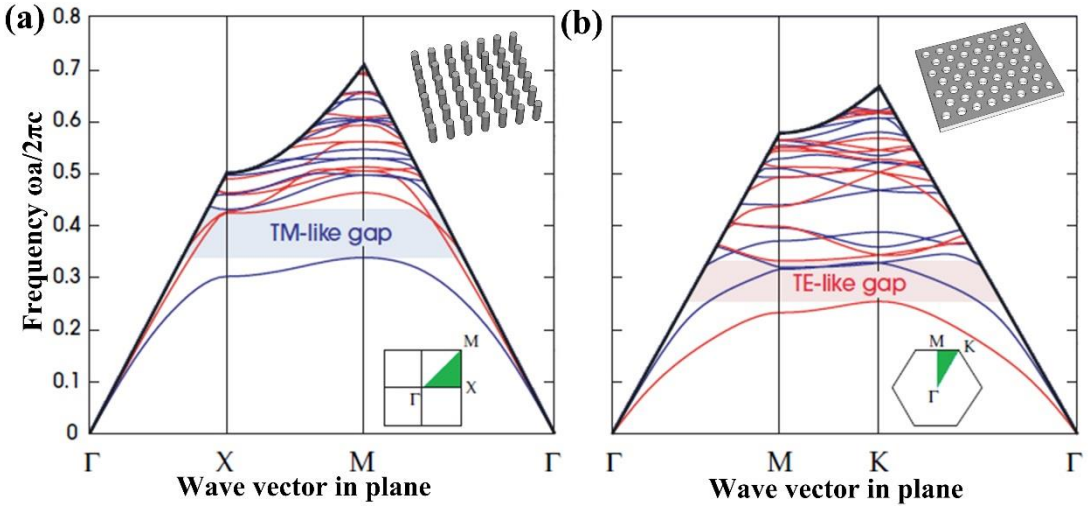

Figure 1.3 Band (dispersion) diagram of modes of (a) pillar slab with 2D square lattice and (b) silicon slab perforated with a 2D triangular lattice (lattice periodicity: *a*). The horizontal axis represents different wave vector (*k*) in the reciprocal space, and the vertical axis represents normalized frequency in the units of a/λ (λ is the wavelength). The solid black line represents the light line. The inset shows the first Brillouin zone (green) in the reciprocal space. TM-like photonic bandgap exists for pillar slab while TE-like photonic bandgap exists for hole slab. Both of them are shaded in the figures [18].

Band (dispersion) characteristic determines optical properties of PC slab. One dispersion curve $\omega(k)$, corresponds to one band of modes in the structure as a function of the in-plane wave vector. The first Brillouin zone in the reciprocal space of the 2D lattice is shown in the insets of Fig. 1.3. High symmetry points, such as Γ, X, M and K, in Brillouin zone of rectangular and triangular lattices follow conventional terminology of semiconductor. Since PC slab is not periodic and with finite thickness in vertical direction, light incident to the surface between the slab and environment with angles larger than TIR critical angle can be confined vertically. Other light with smaller incident angles will be refracted from the slab into environment, resulting lossy modes. To consider this type of loss in the analysis of band diagram of PC slab, we use the notion of the light line, indicated by

the black solid line in Fig. 1.3. The region below light line is called light cone and modes in light cone can be confined in the slab. All other modes out of light cone correspond to leaky modes, although they are not shown in the Fig. 1.3.

Figure 1.3 shows the band diagram for the transverse-magnetic (TM)-like modes of pillar slab with a square lattice and transverse-electric (TE)-like modes in hole slab with a triangular lattice, simulate with PWE method [18]. TE-like modes have dominant E_x, E_y and H_z components while TM-like modes have dominant H_x, H_y and E_z components. For pillar PC slab, photonic bandgap for TM-like modes exists between frequencies of M point of the first band and X point of the second band, as shown in Fig. 1.3a, while for hole PC slab photonic bandgap for TE-like modes exists between frequencies of K point of the first band and M point of the second band. In the photonic bandgaps, guided modes cannot exist with any in-plane wave vector. PC slab's band (dispersion) characteristics including width and location of TE-like or TM-like photonic bandgap, is determined by lots of structure parameters such as refractive index of the slab, refractive index of hole/pillar, type of the 2D lattice (triangular, rectangular, etc.), relative thickness of the slab to periodicity and relative hole/pillar radius to periodicity.

Most schemes studied in this thesis take silicon PC slab as a basic platform. By optically, electrostatically or mechanically tuning the effective refractive index of one unit or multiple units in PC slab, we propose various and versatile reconfigurable PC-based structures.

1.3 Photonic Crystal Resonant Cavity and Waveguide

As discussed in last section, PC slab can confine light in the slab with TE-like or TM-like photonic bandgap. How can these bandgaps be utilized for photonic integrated circuit applications? By inducing point and line defects into a PC slab, the two most basic building blocks, i.e., PC resonant cavity and PC waveguide [19-20], can be formed.

PC resonant cavities are able to localize light with a small mode volume for a long period of time, which is proportional to quality factor Q. The strong light localization in PC cavities significantly amplifies the light-matter and photon-photon interactions, which is important for a wide range of applications, such as lasers, biosensors, and PICs. PC resonant cavities can be easily generated by introduce point defect into PC slab. By tuning the effective refractive index of the defect, we can control the frequency of resonant mode. Also engineering mode volume and quality factor Q for PC resonant cavities is very critical for specified applications such as laser. In PC cavities the localized resonant mode is confined by TIR in vertical direction and photonic bangap in plane direction. However the resonant mode may have vertical radiation losses due to its coupling to radiation modes within the light cone. This part of loss can be described by quality factor $Q_{vertical}$. Meanwhile, the light can leak in plane direction due to the finite number of lattices surrounding the defect. We consider this part of loss by Q_{plane}. Then the overall Q of the cavity can be determined by these two quality factors as follows: $1/Q = 1/ Q_{vertical} + 1/ Q_{plane.}$ If we increase number of PC lattices around the defect in plane direction, Q_{plane} can be improved significantly. In this case $Q_{vertical}$ can dominate the overall Q of the PC resonant cavity. One PC resonant cavity can support different types of defects modes in terms of frequency, Q and field distribution, such as dipole and monopole, which makes its application more versatile. The optimization of Q

in PC cavity has been an active research topic [21], and many research groups have experimentally demonstrated advanced cavities with Q factors greater than 10^6 [22].

Beside PC resonant cavity, PC waveguide is another important building block for PIC application [6]. By performing a line of defects in terms of effective refractive index in PC slab, we can obtain compact low-loss straight waveguide. Even configuring two lines of defects with sharp bend can generate waveguide bend with relatively low loss. These PC-based cavities and waveguides can easily integrated with other on-chip photonic components. This capability benefits the development of compact and wide-bandwidth PICs. Furthermore, PC-based cavities and waveguides can be fabricated with standard semiconductor media and fabrication techniques, facilitating integration with electronics for CMOS-compatible optoelectronic devices.

1.4 Plane-wave Expansion Method

In a solid-state semiconductor material, periodic potential distribution causes electronic bandgap where no electronic states exist. Similarly, PCs have periodic dielectric constant distribution in the material generates a photonic bandgap, where no photonic states exist. Especially when periodicity of dielectric constant distribution is at the same order of wavelength of electromagnetic wave, the photonic bandgap will affect electromagnetic wave propagating in the material.

In order to describe and understand the propagation of light in a periodic structure, the Maxwell's equations are major theoretical equation such as Schrödinger equation for semiconductor physics. Maxwell's equations relate the time- and space-dependent electric

field (**E**), magnetic field (**H**), and the density of free charges (ρ) and currents (**J**), through differential equations. They are written in following form (Equations 1.1-1.4):

$$\nabla \cdot \varepsilon \mathbf{E}(\mathbf{r},t) = \rho(\mathbf{r},t) \quad (1.1)$$
$$\nabla \cdot \mu \mathbf{H}(\mathbf{r},t) = 0 \quad (1.2)$$
$$\nabla \times \mathbf{E}(\mathbf{r},t) = -\mu \frac{\partial \mathbf{H}(\mathbf{r},t)}{\partial t} \quad (1.3)$$
$$\nabla \times \mathbf{H}(\mathbf{r},t) = \mathbf{J}(\mathbf{r},t) + \varepsilon \frac{\partial \mathbf{E}(\mathbf{r},t)}{\partial t} \quad (1.4)$$

where μ and ε are respectively the permeability and the permittivity of the media. Here in this thesis we use silicon as media. And silicon can be taken as dispersionless, non-magnetic, isotropic and lossless around communication wavelength. Then μ and ε are scalar functions independent of field magnitude, direction, and wavelength. Furthermore, no free current and charge are present in the meida ($\rho = 0$, $\mathbf{J} = \mathbf{0}$). Therefore Maxwell's equations can be reduced to Equations 1.5-1.8:

$$\nabla \cdot \varepsilon \mathbf{E}(\mathbf{r},t) = \nabla \cdot \epsilon_0 \epsilon_r(\mathbf{r}) \mathbf{E}(\mathbf{r},t) = 0 \quad (1.5)$$
$$\nabla \cdot \mu_0 \mathbf{H}(\mathbf{r},t) = 0 \quad (1.6)$$
$$\nabla \times \mathbf{E}(\mathbf{r},t) = -\mu_0 \frac{\partial \mathbf{H}(\mathbf{r},t)}{\partial t} \quad (1.7)$$
$$\nabla \times \mathbf{H}(\mathbf{r},t) = \varepsilon \frac{\partial \mathbf{E}(\mathbf{r},t)}{\partial t} = \epsilon_0 \epsilon_r(\mathbf{r}) \frac{\partial \mathbf{E}(\mathbf{r},t)}{\partial t} \quad (1.8)$$

where ϵ_0 is the permittivity in free space and $\epsilon_r(\mathbf{r})$ is the dielectric constant of the material. Since PC has periodic structure, its dielectric constant distribution is invariant under translation of distances that are a multiple of a fixed length, which is the lattice constant **a**. Due to this symmetry, the dielectric constant can be written as:

$$\epsilon_r(\mathbf{r}) = \epsilon_r(\mathbf{r} + l\mathbf{a}) \quad (1.9)$$

where l is an integer.

We use two different numerical methods used to solve Equations 1.5-1.8 for PC structures. The PWE method gives the modal distribution of the field and the dispersion

diagram of PC structure, while the FDTD method is used to obtain the propagation in time and space of the electromagnetic fields. In this section we introduce the PWE method.

Since one set of solutions of Maxwell's equations is monochromatic electromagnetic wave, which is harmonic function of time t of a given angular frequency ω. Thus spatial-dependent and time-dependent parts of electric and magnetic fields in this solution can be separated:

$$\mathbf{E}(\mathbf{r},t) = \mathbf{E}(\mathbf{r})e^{i\omega t} \quad (1.10)$$
$$\mathbf{H}(\mathbf{r},t) = \mathbf{H}(\mathbf{r})e^{i\omega t} \quad (1.11)$$

where $\mathbf{E}(\mathbf{r})$and $\mathbf{H}(\mathbf{r})$ are electric and magnetic fields respectively as function of position $\mathbf{r}$, and $e^{i\omega t}$ describes the harmonic time dependence of the fields. Substituting ∂/∂t by iω in Equations 1.5-1.8, dividing last one of Equation 1.8 by $\epsilon_r(\mathbf{r})$, and taking the curl of them, we get Equations 1.12-1.13:

$$\nabla \times \nabla \times \mathbf{E}(\mathbf{r}) = \left(\frac{\omega}{c}\right)^2 \epsilon_r(\mathbf{r})\mathbf{E}(\mathbf{r}) \quad (1.12)$$
$$\nabla \times \left(\frac{1}{\epsilon_r(\mathbf{r})}\nabla \times \mathbf{H}(\mathrm{r})\right) = \left(\frac{\omega}{c}\right)^2 \mathbf{H}(\mathbf{r}) \quad (1.13)$$

where $c = 1/\sqrt{\epsilon_0\mu_0}$ the speed of light in free space. Unlike Equation 1.12, Equation 1.13 is an eigenvalue equation that governs the propagation of monochromatic light of frequency ω in a dielectric material described by $\epsilon_r(\mathbf{r})$. Therefore it is convenient to solve for $\mathbf{H}(\mathbf{r})$ and then determine $\mathbf{E}(\mathbf{r})$ via Equation 1.3. The master equation (Equation 1.13) has orthogonal solutions each having real eigenvalues $\left(\frac{\omega}{c}\right)^2$.

If we apply Bloch's theorem, for any kind of periodic dielectric constant distribution, the solutions to the master equation has the form $\mathbf{H}(\mathbf{r}) = e^{i\mathbf{k}\cdot\mathbf{r}}\mathbf{u}_{n,\mathbf{k}}(\mathbf{r})$ with eigenvalues $\omega_n(\mathbf{k})$. $\mathbf{u}_{n,\mathbf{k}}(\mathbf{r})$ is an envelope function with the periodicity of the photonic crystal lattice satisfying Equation 1.14:

$$(\nabla + i\mathbf{k}) \times \frac{1}{\epsilon_r(\mathbf{r})} (\nabla + i\mathbf{k}) \times \mathbf{u}_{n,\mathbf{k}}(\mathbf{r}) = \left(\frac{\omega_n(\mathbf{k})}{c}\right)^2 \mathbf{u}_{n,\mathbf{k}}(\mathbf{r}) \qquad (1.14)$$

where **k** is the Bloch wave vector and n=1, 2, . . . is an index that labels the discrete eigenvalues. These eigenvalues $\omega_n(\mathbf{k})$ are continuous functions of **k**, forming discrete bands in a dispersion diagram.

To numerically get the solutions of Equation 1.14, number of plane waves are truncated to a large and finite number. In this thesis freeware MIT Photonic-Bands (MPB) [23] is used to do numerical calculation for band (dispersion) diagrams and corresponding mode distributions. It is a fully-vector eigenmode solver of Equation 1.14 with periodic boundary conditions.

Plane-wave expansion method can also be applied to simulate PC structures with defects. Figure 1.4 shows a typical 2D photonic crystal waveguide, generated by removing one rows of holes in 2D photonic crystal with triangular lattice. A supercell approximation is adopted to model this structure and labeled by dash line in Fig. 1.4. The supercell consists of 1x8 unit cells. The missing hole in center of the supercell corresponds to one unit of a row of missing holes. If we infinitely repeat the supercell in two directions of the plane, we can get infinite number of waveguides with gap of 8 unit cells. Thus by simulating band (dispersion) diagram and corresponding modes of the supercell with PWE, we can approximately obtain the propagation mode of the PC waveguide. Larger supercell will make the simulation more accurate since coupling between the waveguides becomes less due to larger gap.

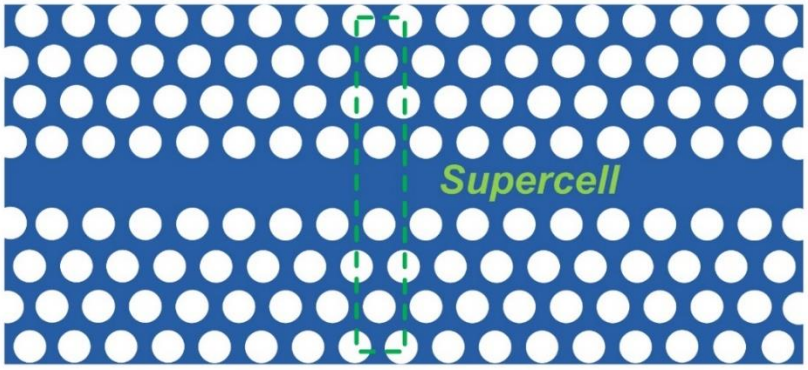

Figure 1.4 A typical 2D PC waveguide with triangular lattice. Supercell with 1x8 unit cell for PWE method is labeled by dash line.

1.5 Finite-difference Time-domain Method

To get fields of electromagnetic wave in space and time with a fixed wavelength, FDTD method can be used for modeling [24]. This method is widely used to model photonic structures since it can handle arbitrary geometry of structures with relatively large refractive index variation. The idea was first proposed by Yee in 1966 [25]. Maxwell's equations are discretized using central-difference approximations to the space and time partial derivatives. The modeled structure is divided into finite lattices of grid points as shown in Fig. 1.5.

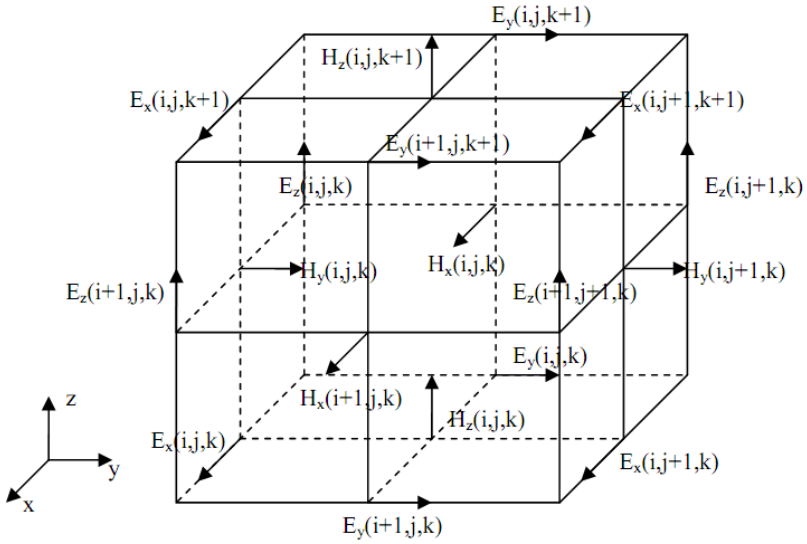

Figure 1.5 A unit cell of 3D FDTD mesh using Yee's method [25].

By applying a simple centered difference approximation to the Maxwell's equations, We can get the following finite difference equations:

$$\mathrm{H}_x\big|_{i,j,k}^{n+1/2} = \mathrm{H}_x\big|_{i,j,k}^{n-1/2} - \frac{\Delta t}{\mu_{i,j,k}}\left(\frac{\mathrm{E}_z\big|_{i,j+1,k}^{n} - \mathrm{E}_z\big|_{i,j,k}^{n}}{\Delta y} - \frac{\mathrm{E}_y\big|_{i,j,k+1}^{n} - \mathrm{E}_y\big|_{i,j,k}^{n}}{\Delta z}\right) \quad (1.15)$$

$$\mathrm{H}_y\big|_{i,j,k}^{n+1/2} = \mathrm{H}_y\big|_{i,j,k}^{n-1/2} - \frac{\Delta t}{\mu_{i,j,k}}\left(\frac{\mathrm{E}_x\big|_{i,j,k+1}^{n} - \mathrm{E}_x\big|_{i,j,k}^{n}}{\Delta z} - \frac{\mathrm{E}_z\big|_{i+1,j,k}^{n} - \mathrm{E}_z\big|_{i,j,k}^{n}}{\Delta x}\right) \quad (1.16)$$

$$\mathrm{H}_z\big|_{i,j,k}^{n+1/2} = \mathrm{H}_z\big|_{i,j,k}^{n-1/2} - \frac{\Delta t}{\mu_{i,j,k}}\left(\frac{\mathrm{E}_y\big|_{i+1,j,k}^{n} - \mathrm{E}_y\big|_{i,j,k}^{n}}{\Delta x} - \frac{\mathrm{E}_x\big|_{i,j+1,k}^{n} - \mathrm{E}_x\big|_{i,j,k}^{n}}{\Delta y}\right) \quad (1.17)$$

$$\mathrm{E}_x\big|_{i,j,k}^{n+1} = \frac{\varepsilon_{i,j,k} - \sigma_{i,j,k}\Delta t/2}{\varepsilon_{i,j,k} + \sigma_{i,j,k}\Delta t/2}\mathrm{E}_x\big|_{i,j,k}^{n} + \frac{\Delta t}{\varepsilon_{i,j,k} + \sigma_{i,j,k}\Delta t/2}\left(\frac{\mathrm{H}_z\big|_{i,j,k}^{n+1/2} - \mathrm{H}_z\big|_{i,j-1,k}^{n+1/2}}{\Delta y} - \frac{\mathrm{H}_y\big|_{i,j,k}^{n+1/2} - \mathrm{H}_y\big|_{i,j,k-1}^{n+1/2}}{\Delta z}\right) \quad (1.18)$$

$$\mathrm{E}_y\big|_{i,j,k}^{n+1} = \frac{\varepsilon_{i,j,k} - \sigma_{i,j,k}\Delta t/2}{\varepsilon_{i,j,k} + \sigma_{i,j,k}\Delta t/2}\mathrm{E}_y\big|_{i,j,k}^{n} + \frac{\Delta t}{\varepsilon_{i,j,k} + \sigma_{i,j,k}\Delta t/2}\left(\frac{\mathrm{H}_x\big|_{i,j,k}^{n+1/2} - \mathrm{H}_x\big|_{i,j,k-1}^{n+1/2}}{\Delta z} - \frac{\mathrm{H}_z\big|_{i,j,k}^{n+1/2} - \mathrm{H}_z\big|_{i-1,j,k}^{n+1/2}}{\Delta x}\right) \quad (1.19)$$

$$\mathrm{E}_z\big|_{i,j,k}^{n+1} = \frac{\varepsilon_{i,j,k} - \sigma_{i,j,k}\Delta t/2}{\varepsilon_{i,j,k} + \sigma_{i,j,k}\Delta t/2}\mathrm{E}_z\big|_{i,j,k}^{n} + \frac{\Delta t}{\varepsilon_{i,j,k} + \sigma_{i,j,k}\Delta t/2}\left(\frac{\mathrm{H}_y\big|_{i,j,k}^{n+1/2} - \mathrm{H}_y\big|_{i-1,j,k}^{n+1/2}}{\Delta x} - \frac{\mathrm{H}_x\big|_{i,j,k}^{n+1/2} - \mathrm{H}_x\big|_{i,j-1,k}^{n+1/2}}{\Delta y}\right) \quad (1.20)$$

where superscript n indicates the number step and subscripts *i*, *j*, and *k* indicate the location of the field in the computational domain. The time step Δt is related to the spatial increments Δx, Δy, and Δz by the stability condition:

$$\Delta t \leq \frac{1}{c_0\sqrt{\Delta x^{-2} + \Delta y^{-2} + \Delta z^{-2}}} \quad (1.21)$$

where c_0 is the light speed in vacuum. We can define a coefficient as the relation between the actual time step and the maximum time step allowed. This coefficient is commonly known as the Courant-Friedrichs-Lewy (CFL) number. Common CFL numbers are 0.866, 0.9, and 0.95.

The finite difference equations are solved at grid points for at each time step, and FDTD updates the field components using the values obtained from previous time step. Commonly excitation sources include plane waves, point or line Gaussian pulses and waveguide modes. Special boundary conditions, such as perfectly matched layer (PML),

need to be applied on the surface of the modeled structure to absorb light and avoid unwanted reflections. In this thesis, MIT freeware MEEP [26] was used to conduct FDTD simulations, to gain transmission of wave propagation in the designed PC structures. Due to the size of the modeling structure, parallel computation with MEEP is performed on workstation in Linux with eight Central Processing Units (CPU) and memory of 48 Gigabytes.

1.6 Problem Statement

As mentioned earlier, high-speed PICs are a promising candidate to replace the present electronic ICs. There has been increasing interest in using 2D planar PCs as a promising PIC platform. The specific properties of a PC slab structure can be tailored by altering the lattice geometry, introducing defects in the lattice, and changing the index contrast between the constituent materials. PC slabs provide the ability to confine light at the wavelength scale on a planar architecture, and hence, allow the realization of various photonic devices such as waveguides with sharp bends, spectral filters, add-drop multiplexers, lasers, etc.

Most of the existing PICs reported to date, however, are static. Their appearance and functionality are fixed by fabrication. As their complexity and functionality continue to increase, more photonic building blocks and interconnections are required to implement functions with stringent requirements on device size, weight, and power consumption (SWP). A relatively universal PIC platform, where different photonic building blocks and their interconnections could be configured/reconfigured dynamically and even programmably at any location(s) of the platform to form complex photonic circuits on demand, would considerably reduce and even eliminate the need for designing and manufacturing a large

number of different specialized photonic building blocks, saving great cost and SWP. Furthermore, if one were able to individually tune the optical properties of those configured/reconfigured photonic components further, it would no doubt provide an additional dimension of versatility and adaptability. Therefore, implementing the innovative concept of a programmable, reconfigurable, and tunable photonic integrated circuit platform is appealing to the photonics community.

So far, the concept of the programmable, reconfigurable, and tunable PIC platform is not realized yet. As mentioned, PC slab is promising candidates for a PIC platform. However, for a planar PC to become a fully dynamic platform, three main barriers exist: 1) insufficient capability to significantly modulate the dielectric properties of the PC structure with a relatively fast response time, thus low tunability; 2) a lack of a simple mechanism to individually address each unit cell of the PC, thus low reconfigurability; and 3) difficulty in integrating the PC structure with electronic ICs on a single chip, thus low programmability.

1.7 Research Objectives

The main mission of this thesis is to overcome the aforementioned barriers, leading to the discovery of several programmable, reconfigurable, and tunable PC devices.

The first objective is to develop an optical programmable PIC platform that integrates digital micromirror device (DMD), photo-responsive liquid crystals (LCs), and PC technologies. Periodic air holes in a photonic crystal slab are infiltrated with photo-responsive LCs. The refractive index of each hole can be individually modulated by projecting light patterns into the hole using a DMD. In the Chapter 3 we first theoretically

investigate the functionality of a LC-infiltrated PC slab, and then, discuss the fabrication and characterization of the device.

The second objective is to discover two types of reconfigurable PC devices using nanobeams and nano-electro-mechanical systems (NEMS) technologies. The first device consists of an array of electrostatically tunable nanobeams. We demonstrated the capability of the device to engineer different photonic bandgaps. To achieve a higher-level integration, we also theoretically studied another reconfigurable PC integrating an array of tunable nanobeams with an array of fixed pillars into the top silicon layer of a SOI wafer.

The third objective is to study two tunable PC-cantilever cavity (PC^3) resonators. The first device has an NEMS cantilever embedded into a L6 cavity in a PC slab. The second device has a similar cantilever to insert into a nanobeam-base waveguide. We studied bending characteristics of the cantilever and optical characteristics of these two devices at different applied voltages. These resonators are theoretically and experimentally studied in Chapter 5.

The last objective is to investigate a programmable 2D PC slab. In Chapter 6, we theoretically demonstrated the possibility of forming a highly reconfigurable PC device by individually introducing a different number of nanoplugs into corresponding air holes of a PC slab.

References

[1] F. Fiori, "Integrated circuit susceptibility to conducted RF interference," *Compliance Engineering* 17, pp. 40−49, 2000.

[2] G. T. Reed, *Silicon Photonics: The State of the Art*, Wiley-Interscience, 2008.

[3] X. Chen, C. Li, and H. K. Tsang, "Device engineering for silicon photonics," *NPG Asia Materials*, Vol. 3, pp. 34−40, 2011.

[4] G. T. Reed, G. Mashanovich1, F. Y. Gardes, and D. J. Thomson, "Silicon optical modulators," *Nature Photonics* Vol. 4, 518−526 2010.

[5] M. J. R. Heck, H.-W. Chen, A. W. Fang, B. R. Koch, D. Liang, H. Park, M. Sysak, and J.E. Bowers, "Hybrid silicon photonics for optical Interconnects*," IEEE J. Sel. Topics Quantum Electron.*, Vol. 17, pp. 333–346, 2011.

[6] J. D. Joannopoulos, S. G. Johnson, J. N.Winn, and R. D. Meade, *Photonic Crystals: Molding the Flow of Light*, 2nd ed. Princeton, NJ: Princeton Univ. Press, 2008.

[7] L. Thylen, M. Qiu, and S. Anand, "Photonic crystals - a step towards integrated circuits for photonics," *ChemPhysChem*, Vol. 5, pp. 1268−1283, 2004.

[8] V. Liu and S. Fan, "Compact bends for multi-mode photonic crystal waveguides with high transmission and suppressed modal crosstalk," *Opt. Express*, Vol. 21, pp. 8069−8075, 2013.

[9] G. Shambat, M. S. Mirotznik, G. Euliss, V. O. Smolski, R. A. Athale, E. G. Johnson, "Photonic crystal filters for multi-band optical filtering on a monolithic substrate," *J. Nanophoton.*, Vol. 3, pp. 031506−1−11, 2009.

[10] Y. Akahane, T. Asano, H. Takano, B. S. Song, Y. Takana and S. Noda, "Two-dimensional photonic-crystal-slab channel-drop filter with flat-top response," *Opt. Express*, Vol. 13, pp. 2512−2530, 2005.

[11] H. Altug, D. Englund and J. Vuckovic, "Ultrafast photonic crystal nanocavity laser," *Nature Physics*, Vol. 2, pp. 484−488, 2006.

[12] R. Chen, A. Yan, M. Li, T. Chen, Q. Wang, J. Canning, K. Cook, and K. P. Chen, "Regenerated distributed Bragg reflector fiber lasers for high-temperature operation," *Optics Letters*, Vol. 38, pp. 2490−2492, 2013.

[13] C. Gierl, T. Gruendl, P. Debernardi, K. Zogal, C. Grasse, H. A. Davani, G. Bohm, S. Jatta, F. Kueppers, P. Meissner, and M.-C. Amann, "Surface micromachined tunable 1.55 μm-VCSEL with 102 nm continuous single-mode tuning," *Opt. Express*, Vol. 19, pp. 17336−17343, 2011.

[14] E. Yablonovitch, "Inhibited spontaneous emission in solid-state physics and electronics," *Phys. Rev. Lett.*, Vol. 58, pp. 2059–2062, 1987.

[15] S. John, "Strong localization of photons in certain disordered dielectric superlattices," *Phys. Rev. Lett.*, Vol. 58, 2486−2489, 1987.

[16] H. K. Tyagi, M. A. Schmidt, L. P. Sempere and P. St. J. Russell, "Optical properties of photonic crystal fiber with integral micron-sized Ge wire," *Opt. Express*, Vol. 16, pp. 17227−17236, 2008.

[17] J. G. Fleming, S. Y. Lin, I. El-Kady, R. Biswas and K. M. Ho, "All-metallic three-dimensional photonic crystals with a large infrared bandgap," *Nature*, Vol. 417, pp. 52–55, 2002.

[18] R. D. Meade, A. M. Rappe, K. M. Brommer, J. D. Joannopoulos, and O. L. Alerhand, "Accurate theoretical analysis of photonic bandgap materials," *Phys. Rev. B*, Vol. 48, pp. 8434–8437, 1993.

[19] S. Noda, A. Chutinan and M. Imada, "Trapping and emission of photons by a single defect in a photonic bandgap structure," *Nature*, Vol. 407, 608−610, 2000.

[20] E. Chow, S. Y. Lin, J. R. Wendt, S. G. Johnson and J. D. Joannopoulos, "Quantitative analysis of bending efficiency in photonic-crystal waveguide bends at $\lambda = 1.55$ μm wavelengths," *Opt. Lett.*, Vol. 26, pp. 286–288, 2001.

[21] J. Vuckovic, M. Loncar, H. Mabuchi, and A. Scherer, "Optimization of the Q factor in photonic crystal microcavities," *IEEE J. Quantum Elect.*, Vol. 38, pp. 850−856, 2002.

[22] Y. Akahane, T. Asanol, B. S. Song and S. Noda, "High-Q photonic nanocavity in a two-dimensional photonic crystal," *Nature*, Vol. 425, pp. 944−947, 2003.

[23] http://ab-initio.mit.edu/wiki/index.php/MIT_Photonic_Bands

[24] A. Taflove, *Advances in Computational Electrodynamics: The Finite Difference Time Domain Method*, Artech House Publishers, 1998.

[25] K. Yee, "Numerical solution of initial boundary value problems involving Maxwell's equations in isotropic media," *IEEE T. Antenn. Propag.*, Vol. 14, pp. 302–307, 1966.

[26] A. F. Oskooi, D. Roundy, M. Ibanescu, P. Bermel, J. D. Joannopoulos, and S. G. Johnson, "MEEP: A flexible free-software package for electromagnetic simulations by the FDTD method," *Comput. Phys. Commun.*, Vol. 181, pp. 687−702, 2010.

CHAPTER 2. NANOFABRICATION AND OPTICAL COUPLING TECHNIQUES FOR SILICON PHOTONIC DEVICES

2.1 Overview

SOI is a key platform for silicon-based photonic circuits. Main fabrication techniques includes e-beam lithography, reactive ion etching, dry and wet oxidation, ion diffusion, wet etching, and e-beam evaporation. Some main equipment used in this research is shown in Fig. 2.1.

Figure 2.1 Major fabrication equipment used in this research. (a) Raith e-beam lithography system. (b) Reactive ion etching system. (c) Oxidation and ion diffusion furnaces. (d) E-beam evaporator system.

Figure 2.2 shows the fabrication steps for SOI based photonic devices. Firstly, the top silicon layer of a SOI wafer is thinned down to a desired thickness by dry/wet oxidation of silicon and wet etching of oxide if the initial thickness is larger than a desired one. Wet oxidation results in a coarse thickness, while dry oxidation helps fine tuning the thickness of the top silicon layer. Wet chemical etching removes the generated oxide layer from the top silicon layer. After thinning down, the top silicon layer is doped with boron or phosphorus ions to increase its electrical conductivity such as the top silicon layer can serve as an electrical ground or electrode material. Secondly, e-beam resist poly(methyl methacrylate)

(PMMA) is deposited on the SOI wafer by spin-coating. Note that the original size of the SOI wafer is six inches in diameter. We dice the wafer into small pieces (one centimeter square) after prebaking the PMMA resist. Thirdly, the PMMA layer is patterned using Raith e-beam lithography. Fourthly, the patterns are transferred from the PMMA layer into the top silicon layer using reactive ion etching. In this step, the PMMA layer serves as a protection layer. Fifthly, lateral wet chemical etching was used to release mechanical structures (e.g., cantilever, membrane), while other parts of the devices are not released, but still anchored to the oxidation layer underneath these parts). Lastly, the PMMA layer is stripped off by PMMA remover.

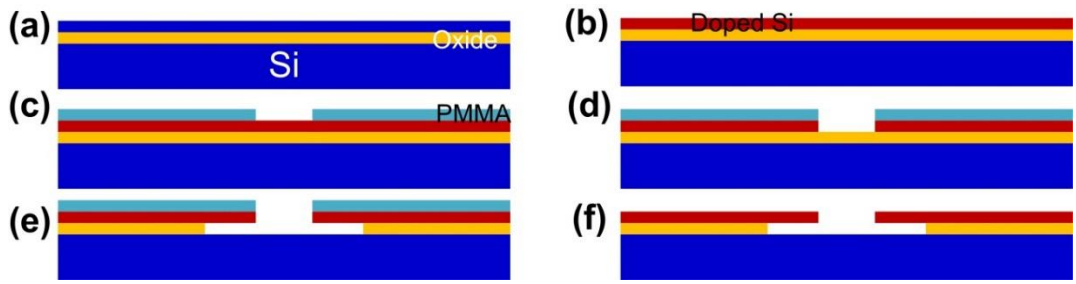

Figure 2.2 Fabrication processes for development of silicon photonic devices on a SOI wafer. (a) Thinning of the top silicon layer by dry/wet oxidation and wet etching. (b) Conductivity adjustment in the top silicon layer by ion diffusion. (c) E-beam lithography for creating patterns in a PMMA resist layer; (d) Reactive ion etching for transferring patterns to the top silicon layer; (e) Releasing mechanical structures by wet etching (f) Stripping off the PMMA resist.

In following sections we will describe technical details of these fabrication processes. Also, we will discuss the design and fabrication of grating couplers, which are critical components in silicon photonic devices to couple light into and out of the devices. The devices discussed in the following chapters use grating couplers.

2.2 E-beam Lithography

Raith e-beam lithography uses high-energy (typically 10 kV) electron beams to generate nanoscale patterns on a thin (~ 100 nm) e-beam resist layer [1-3]. The main advantage of e-beam lithography over conventional photolithography comes from the fact that de Broglie wavelength of election is much smaller than that of ultraviolet light and diffraction limit of light is overcome. E-beam lithography can be used to make high-resolution masks for photolithography or generate high-resolution patterns for semiconductor and photonic devices.

Raith electron beam scans back and forth over the surface to generate patterns. At each fixed magnification during exposure of electron beam, the exposed area on sample surface is called write field. Inside a write field, the electron beam can cover the whole area by changing only electron optics (lens) without shifting sample stage. Exposure (scanning) of electrons could be very time-consuming with high cost if size of pattern is more than twenty times of the write field since the system needs to move stage block by block with accurate alignment. Generally, we select magnification of 1000 for exposure, which corresponds to a write field with size of 100 μm×100 μm. Figure 2.3 shows a pattern designed by Raith editor for a typical PIC containing two grating couplers and a PC structure. The pattern is automatically divided into seven write fields during exposure. Exposure of e-beam starts at the most left write field first and stitch all other write fields together.

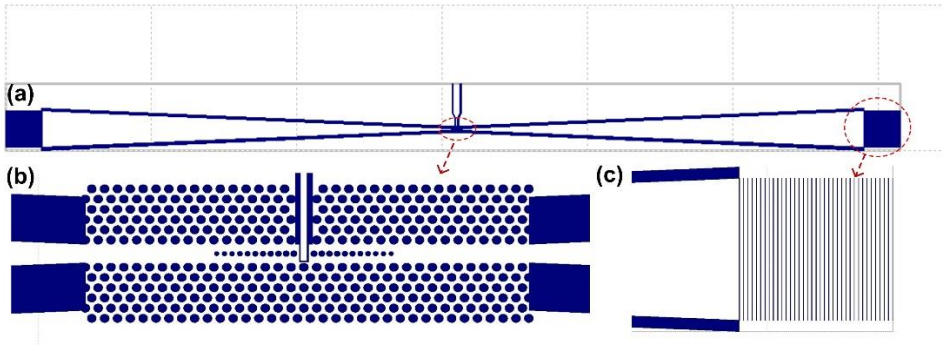

Figure 2.3 (a) Overview of pattern for an integrated photonic crystal-cantilever configuration designed by Raith editor; (b) Pattern for photonic crystal-cantilever structure; (c) Pattern for 1D grating coupler.

Many factors determine the spatial resolution of patterns created by e-beam lithography, including the system operation parameters (e.g., accelerating voltage, working distance, and scanning step size of beam), and e-beam resist properties (e.g., sensitivity, contrast, and process stability). For most e-beam resists, it is difficult to realize area patterns with feature size below 30 nm, while for line patterns (such as gratings) the minimum feature size is about 10 nm with step size of 20 nm [4]. When the feature size is small and the structure is relatively unconventional, structural distortion can happen to some extent. Figure 2.4a is a scanning electron microscope (SEM) picture for a patterned 1D PC with a defect plate in one photonic unit. The plate is designed to be hexangular. However, due to the distortion of limited step size, the final pattern has a round shape. Figure 2.4b corresponds to a similar but larger defect structure. Fortunately, the air hole structures of PCs, such as those shown in Figs. 2.4a and 2.4b, have almost zero distortion.

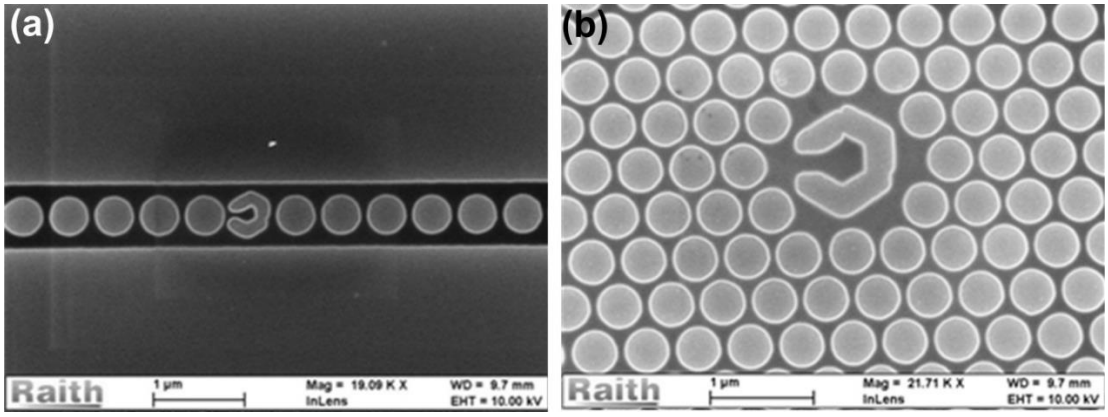

Figure 2.4 SEM pictures of distorted plate structure embedded in 1D (a) and 2D PC structures after e-beam lithography.

Compared to the original design, the patterns formed in e-beam resist may also get expanded. The expansion rate depends on both dose factor and feature size. As shown in Fig. 2.5a, the dose factor is one and the area dose of 100 C/cm^2. The expansion rate of a U-shaped pattern with a feature size of 100 nm can be two. However, a long cantilever, which is embedded inside a 2D PC structure patterned with the same dose parameters, has a limited expansion rate of 1.1 (Fig. 2.5b). By carefully considering the feature size and corresponding expansion rate, we are able to integrate our PC-cantilever structures with an accurate size after exposure (Fig. 2.6).

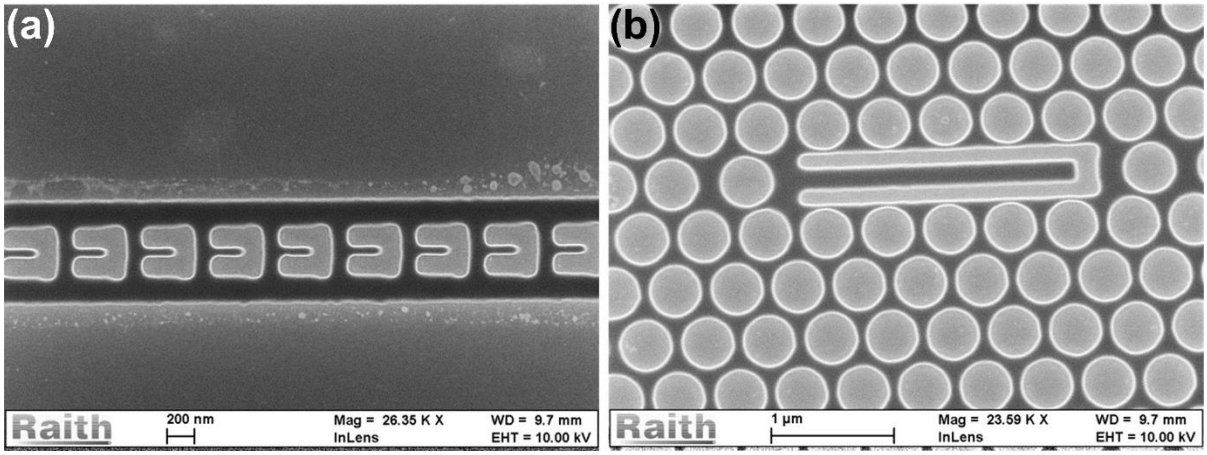

Figure 2.5 SEM pictures of expanded patterns after e-beam lithography.

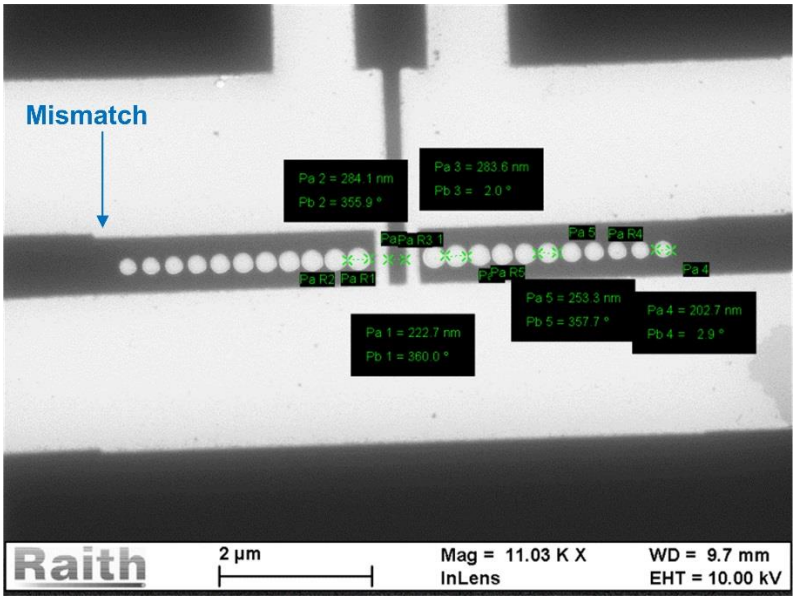

Figure 2.6 SEM picture of a PC-cantilever structure after e-beam lithography.

There are other two important issues with e-beam lithography, i.e., stitching error and proximity effect. As mentioned above, the write-filed alignment is critical to obtain the best possible e-beam lithographic result. Essentially, it is the adjustment of the electron optics inside the column to the high precision X-Y-Z laser-controlled stage. For large-area patterning, the pattern has to be divided into several write-fields. This is called the stitching of write-fields. The stitching often gives rise to stitch errors, because there is no perfect matching between adjacent write-fields. These errors can be minimized by careful write-field alignment, increasing junction pattern areas and including over-exposed patches. However, there is no guarantee that stitch errors would be eliminated each time. In most cases, stitch error is caused by the random precision errors when the laser-controlled stage moves. Depending on the working condition, this error can cause pattern mismatch ranging from a few to hundreds of nanometers. In Fig. 2.6, we can see a mismatch of a few nanometers at the interface between the PC waveguide and the tapered input waveguide.

There are two types of e-beam resist. Positive resist undergoes chain-scission upon e-beam exposure and the exposed part becomes soluble. Negative resist reacts to electrons by cross-linking and becomes insoluble after exposure. We used positive resist PMMA for our lithography. By careful write-field alignment and applying patches, the stitch error is barely noticeable. We have developed a general patterning protocol for Raith e-beam lithography, which is listed as follows:

- Set the spin speed to 4000 rpm and spin time to 45 seconds, and coat the sample with 950 PMMA A2 (from Microchem). The final thickness of PMMA is ~100 nm.
- Prebake at 170 °C for 30 min.
- Load the sample into the chamber. Set the local coordinates.
- Set the accelerating voltage at 10 kV and select 30 μm aperture in Raith system. Choose 100 μm write-field size and 30 μm aperture.
- Adjust the aperture alignment, stigmation and focus to maximize SEM image quality until you can burn a contamination dot with size less than 20 nm.
- Do write-field alignment manually based on the small contamination dots.
- Choose area scan mode for all patterns and set stage step size to 20 nm.
- Measure the current at farad cup. Set the area dose to 100 C/cm^2 and calculate the dwelling time.
- After exposure (scanning) develop the sample in MIBK to IPA 1:3 for 35 seconds.
- Postbake at 170 °C.

2.3 Reactive Ion Etching

The silicon devices developed in this thesis are fabricated in a SOI wafer and the top silicon layer is 200 nm. E-beam resist (PMMA) is used as a protecting mask to transfer patterns into silicon. To achieve anisotropic etching of silicon, sulfur hexafluoride (SF_6), argon (Ar) and oxygen (O_2) are used as plasma source gases. SF_6 is the primary etchant. After development of patterns, silicon surfaces of the patterns are exposed to reactive fluorine radicals that isotropically etch the unprotected silicon. The remaining fluorocarbon polymer protects the vertical walls from etching. To obtain a good etching rate and optimum ratio of lateral to vertical etching, SF_6 flow is fixed at 18 sccm, O_2 flow at 6 sccm, and Ar flow at 10.6 sccm. Radio frequency (RF) power is set to 20 W. Note that for small trenches such as air holes in PC structures, the etching rate is significantly smaller than that for large openings. With this recipe, the etching rate of silicon is about 130 nm per minute for patterning structures with a feature size of larger than one micron. For our PC-cantilever structure, the etching rate in air holes is about 70 nm. To make sure the top silicon layer is completely etched, we set the etching time to be 2 minutes. This recipe provides an etching selectivity of 100:1 for silicon with respect to PMMA. Also lateral etching of silicon with respect to vertical etching of silicon is about one tenth, as shown in Fig. 2.7.

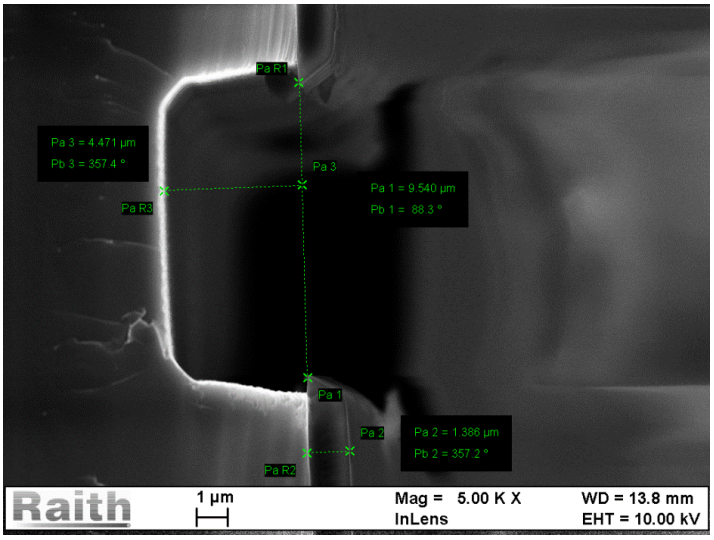

Figure 2.7 SEM picture of cross-section view for a silicon sample after RIE process.

Before dry etching starts, the sample is cleaned with low-power O_2 plasma. Some resist residues in the patterns are removed from the sample. This step also helps reduce the roughness in the resist side walls for a better profile. Pre-etching bake is recommended for an improved etching selectivity of silicon to resist. After dry etching, the resist is removed by high-power O_2 plasma. To further reduce the surface roughness, the sample can go through thermal oxidation, where a 20-30 Å thin silica layer helps smoothen out silicon surfaces. Figure 2.8 shows a PC-cantilever device after the dry etching process.

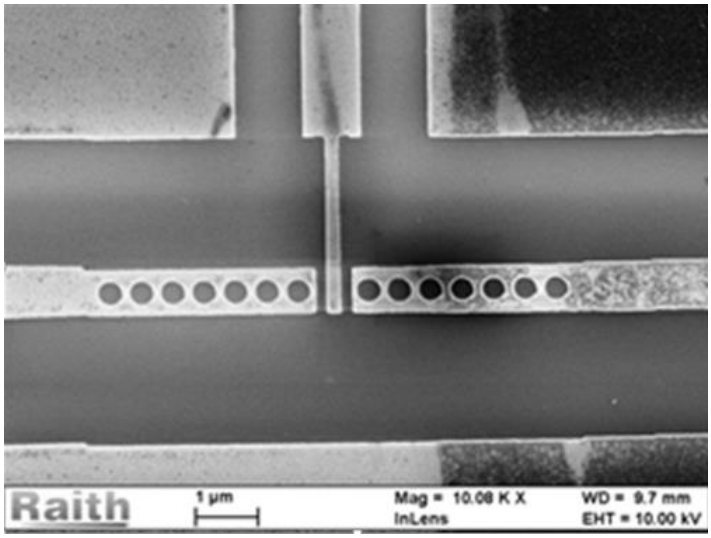

Figure 2.8 SEM picture of a PC-cantilever device after dry etching.

2.4 Wet Chemical Etching

To release a mechanical silicon structure from a PC slab, we use a buffered oxide etch (BOE) solution to etch the silicon dioxide underneath the mechanical structure. BOE is a mixture of a buffering agent, such as ammonium fluoride (NH_4F), and hydrofluoric acid (HF). Concentrated HF (typically 49% HF in water) is not recommended to etch silicon dioxide because of its high etching rate and thus poor process control.

Figure 2.9 and Figure 2.10 show two sample devices where the cantilevers need to be removed while the PC waveguides (both are broken at the tip of a sword-like cantilever) still need to be anchored on the oxide layer. The devices in Fig. 2.9 and Fig. 2.10 result from 1.5 min, and 2 min, respectively, of etching in a BOE solution. As we can see, the cantilevers are release while the anchors of the PC waveguides still remain on the substrate.

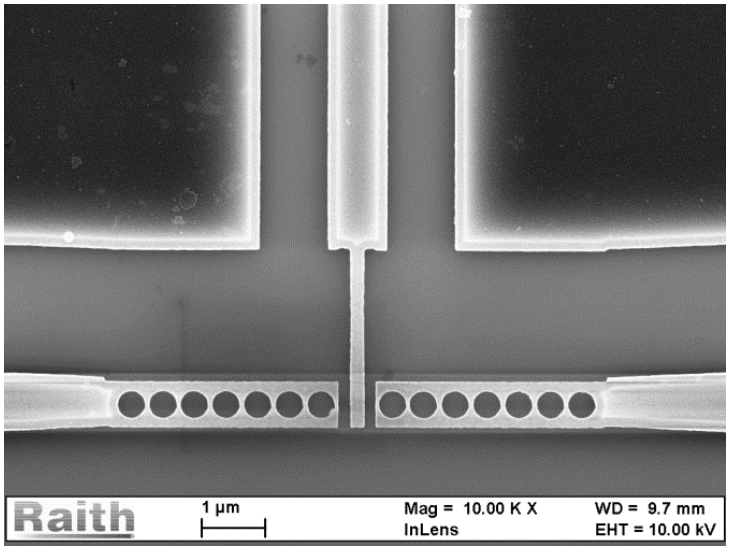

Figure 2.9 SEM picture of a PC-cantilever device after wet etching of silicon oxide in a BOE solution for 1.5 min.

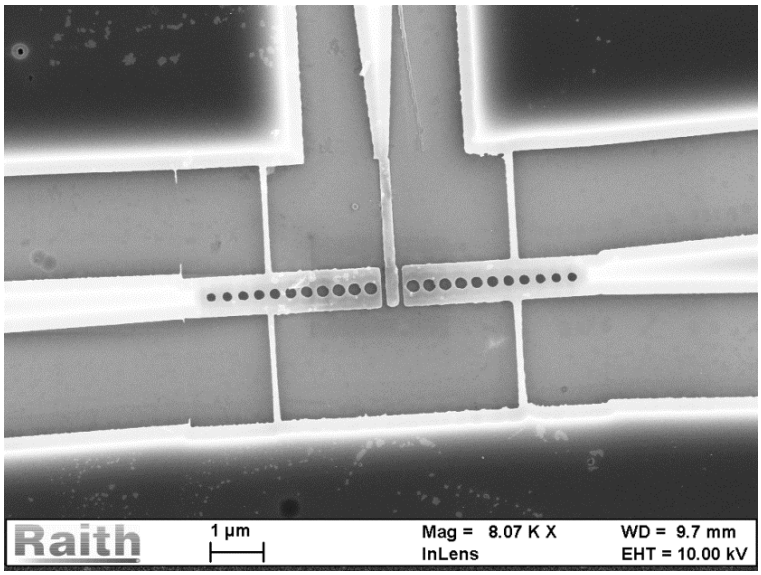

Figure 2.10 SEM picture of a PC-cantilever device after wet etching of silicon oxide in a BOE solution for 2 min.

2.5 Metallization and Lift-off

In Chapter 4, we need to fabricate gold nanoelectrodes on a glass substrate. The gold nanoelectrodes are formed by three subsequent processes, including e-beam lithography, metallization, and lift-off. E-beam evaporator is used to deposit gold thin films for metallization. To facilitate the following lift-off process for forming nanoelectrodes, thickness of gold film is controlled to be 20-50 nm. However, a thinner gold layer (i.e., 10 nm thick) provides a rough surface with visible grains. In our process, the deposition rate of gold by using e-beam evaporation is about 1.1 Å/s. To improve the adhesion of gold on a glass or silicon substrate, 3 nm thick titanium layer is first deposited.

As mentioned earlier, the thickness of PMMA resist is about 100 nm, which is 2-5 times larger than that of the deposited metal film. Therefore, the PMMA resist can be easily lifted off. The lift-off process is described as follows.

- Use e-beam lithography to define the pattern on a glass substrate. In this step, a 10 nm thick conductive polymer (PEDOT:PSS) is spun on the top surface of

a 100 nm thick PMMA resist, to improve the surface conductivity for better E-beam lithography.

- Clean the sample with low-power plasma.
- Metal evaporation: 3 nm Ti and 20 nm Au.
- Soak the sample in acetone for 2 minutes with ultrasonic at room temperature.
- Soak the sample PMMA remover for 40 minutes with ultrasonic at 80 degree.
- Rinse the sample in water for 2 minutes and blow dry with N_2.

2.6 Grating Coupler

When light is incident from an optical fiber to a silicon photonic chip through butt-coupling, high coupling losses may occur, due to significant size difference between the external optical fiber and a waveguide on the chip. Standard single-mode fiber core diameter is around 10 μm, while conventional single-mode photonic waveguide core is about 500 nm wide and 250 nm high. Geometric overlapping is only about 0.16 %, and thus, mode mismatch is also significant.

One of the most suitable solutions for efficient light coupling from an optical fiber to a silicon waveguide is to use on-chip grating couplers. Compared with other in-plane coupling techniques, the grating-based vertical coupling technique is advantageous in structure compactness and coupling efficiency. The dimensions of a grating coupler can be about 20 μm × 20 μm. Actually, the vertical grating coupling technique has been studied and implemented extensively by many research groups. More than 30% coupling efficiency has been demonstrated experimentally [5]. The coupling efficiency can be further increased by tuning the grating period, coating the substrate with a reflecting layer such as gold, adding

silica/polymer upper cladding, and etc. These gratings are formed in a 200-330 nm thick top silicon layer of a SOI wafer.

1D grating coupler is of the most common grating couplers. The coupler is a simple 1D grating structure etched through the top silicon layer. Since the length of grooves in the grating is at least 15 times of wavelength, 2D modeling is used for optical simulations. Using a commercial FEM software COMSOL Multiphysics, we simulate the mode profile in the grating when light is incident onto the grating surface at different incident angles. The model includes an input and an output grating and a slab waveguide. By fine tuning the groove width and periodicity of the grating, the grating works in a wavelength range from 1500 nm to 1700 nm. The optimized groove width is 95 nm and the periodicity is 920 nm. As seen in Fig. 2.11a, light at a wavelength of 1500 nm can be coupled into the slab waveguide at an incident angle between 20° and 30°. When the incident angle is fixed at 20°, light at the wavelength of 1500 nm and 1550 nm can also easily tunnel into the silicon slab waveguide, as shown in Fig. 2.11b. Figure 2.11c and Figure 2.11d respectively describe two cases: (1) the overall efficiency of light coupling into the slab waveguide with respective to wavelength at normal incidence, and (2) that with respective to an incident angle at wavelength of 1550 nm. The maximum efficiency with respect to wavelength is about 10%. For the wavelength range from 1500 nm to 1670 nm, the efficiency is always more than 5%. The full width at half maximum (FWHM) of efficiency with respect to incident angle is more than 20°, indicating a good tolerance for alignment. The through-etched air grooves make the grating's index contrast very high. As a result, the Fresnel reflection is very high, and the coupling efficiency lower than those 1D grating couplers involving multiple lithography and etch [6].

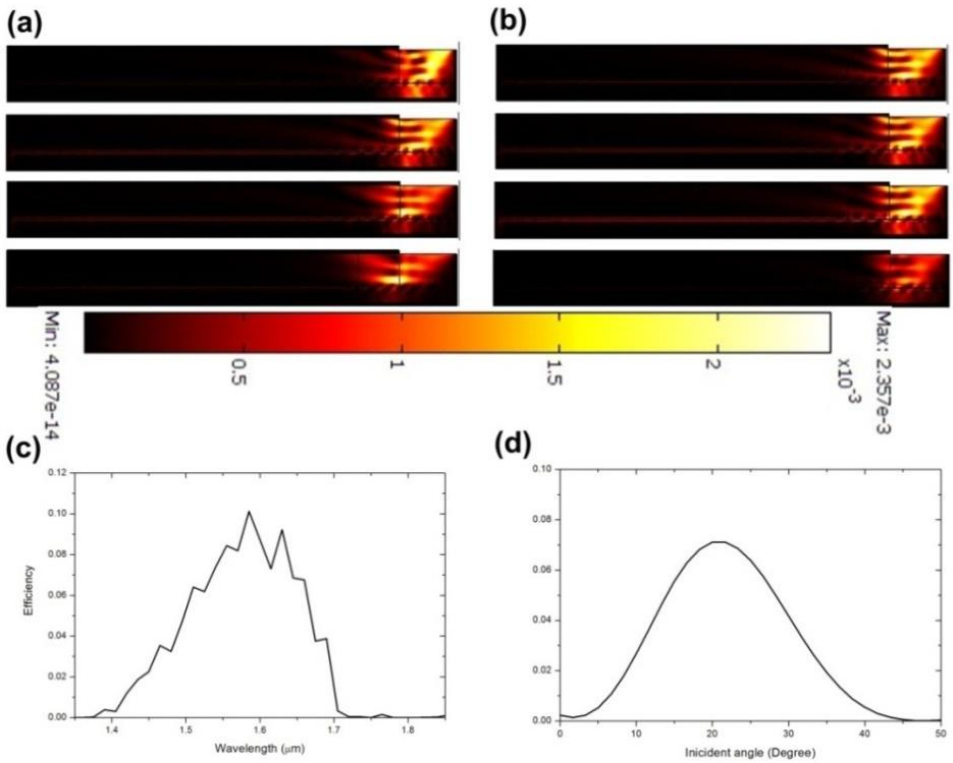

Figure 2.11 (a) Power flow distribution throughout the grating coupler at incident angle of 10°, 20°, 30° and 40° (from top to bottom) with wavelength of 1500 nm. (b) Power flow distribution throughout the grating coupler with wavelength of 1450 nm, 1500 nm, 1550 nm and 1700 nm at incident angle of 20° (from top to bottom). Efficiency of grating coupler with respect to wavelength at normal incidence (c) and incident angle with wavelength of 1550 nm (d).

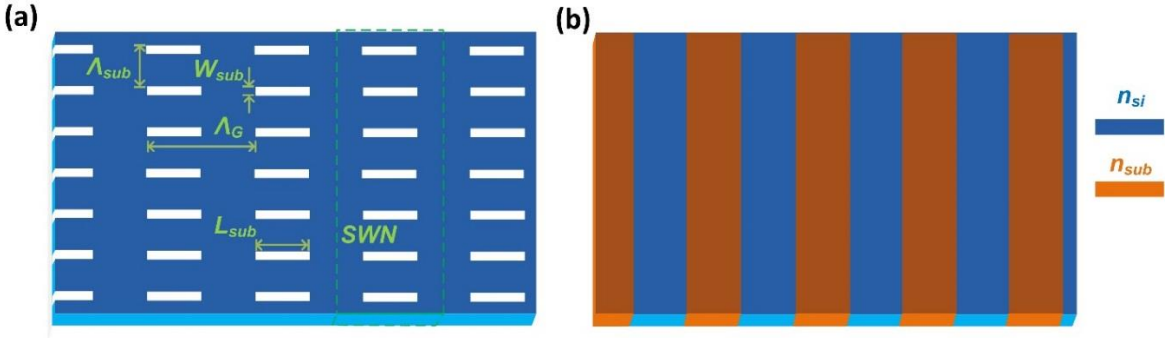

Figure 2.12 (a) Schematic of the subwavelength grating. SWN is labeled by dash line. (b) The equivalent conventional 1D grating coupler. Uniform strips replace SWN strips with refractive index n_{sub}. The refractive index n_{sub} can be controlled by tuning the width W_{sub} of the rectangular air hole and the period Λ_{sub} of the subwavelength structure.

To further improve coupling efficiency of the grating coupler, we should weaken Fresnel reflection. One method is decreasing the contrast of refractive index in the grating.

However for our through-etched grating, the contrast is fixed (silicon vs air). Fortunately, researchers in University of Texas recently proposed artificial materials with engineered indices of refraction that can meet these requirements [7]. The artificial material is the subwavelength nanostructure (SWN), taken as a low index material. Using SWN, one can engineer the refractive index of trench in grating coupler. A TE polarized grating coupler achieving a 79% coupling efficiency at 1550 nm, as reported in Ref. 6.

According to the effective medium theory, a composite medium comprising two different materials interleaved at the subwavelength scale can be approximated as a homogenous medium with an effective refractive index between these two materials [8]. Therefore, the subwavelength grating (SWG) is equivalent to the conventional one-dimensional grating coupler shown in Fig. 2.12b. The subwavelength region is regarded as a homogeneous material with an effective index n_{sub}. The uniform material is then replaced with a SWN, as labeled with dash line in Fig. 2.12a. In this configuration, the refractive indices of SWN n_{sub} for TE and TM can be calculated through equations below [7]:

$$\frac{\sqrt{n_{si}^2-n_{TE}^2}}{n_{si}^2}\tan\left[\frac{\pi\sqrt{n_{si}^2-n_{TE}^2}(\Lambda_{sub}-W_{sub})}{\lambda}\right]=-\frac{\sqrt{n_{hole}^2-n_{TE}^2}}{n_{hole}^2}\tan\left[\frac{\pi\sqrt{n_{hole}^2-n_{TE}^2}W_{sub}}{\lambda}\right] \quad (2.1)$$

$$\sqrt{n_{si}^2-n_{TM}^2}\tan\left[\frac{\pi\sqrt{n_{si}^2-n_{TM}^2}(\Lambda_{sub}-W_{sub})}{\lambda}\right]=-\sqrt{n_{hole}^2-n_{TM}^2}\tan\left[\frac{\pi\sqrt{n_{hole}^2-n_{TM}^2}W_{sub}}{\lambda}\right] \quad (2.2)$$

where n_{TE} and n_{TM} are the refractive indices of SWN for TE and TM polarizations, respectively. n_{si} and n_{hole} are the refractive indices of the silicon and the material in the holes, respectively. In our design, the holes are filled with air ($n_{hole}=1$). Λ_{sub} is the period of the SWN, and W_{sub} is the width of the rectangular air holes. The trench width W_{sub} is fixed to 80 nm with a corresponding Λ_{sub} of 388 nm. Using Matlab numerically calculate the

solution of the equations above, we get the effective index n_{TE} of 2.45 for TE polarization. Λ_G is set to 686 nm, and the duty cycle of the grating is 50%.

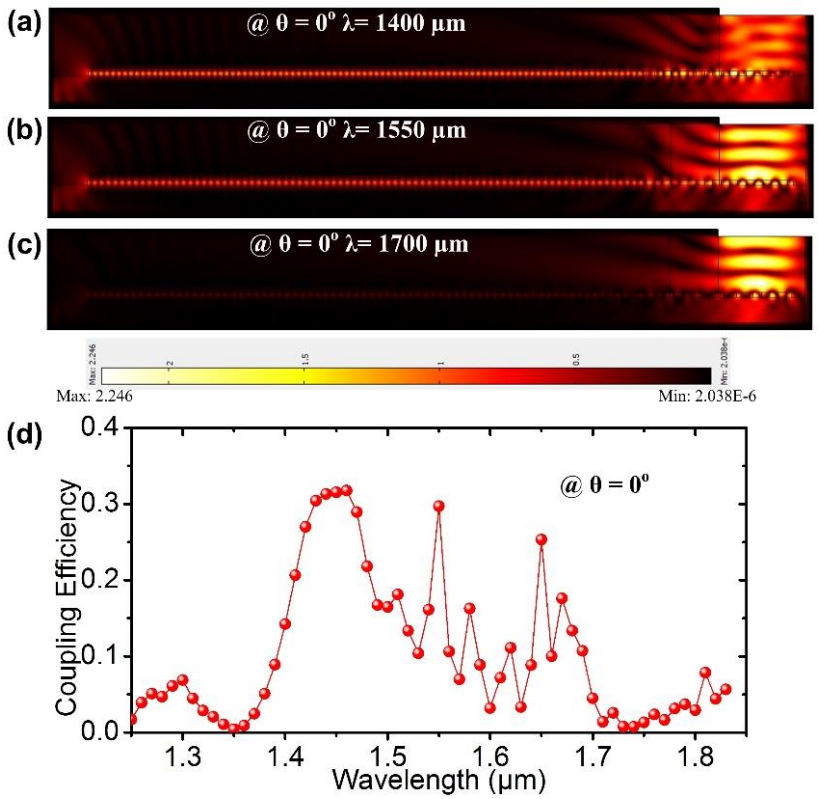

Figure 2.13 (a-c) Electric field distribution throughout the grating coupler at normal incident angle with a wavelength of 1400 nm (a), 1550 nm (b) and 1700 nm (c). (d) Efficiency of the grating coupler with respect to wavelength at normal incident angle.

Again, using the FEM software COMSOL Multiphysics, we have simulated the equivalent 1D grating with n_{TE} of 2.45. As shown in Fig. 2.13a and 2.13b, light with normal incidence can be coupled into the device with wavelength of 1400 and 1550nm. The range of working wavelength (with an efficiency more than 5%) spans from 1300 nm to 1600 nm. From Fig. 2.14, we can find that light with wavelength of 1550 nm can be coupled into the slab waveguide at incident angle from 0° to 20° with efficiency more than 5%. Therefore, the grating performs better than the simple 1D grating coupler in terms of coupling efficiency and optical alignment tolerance.

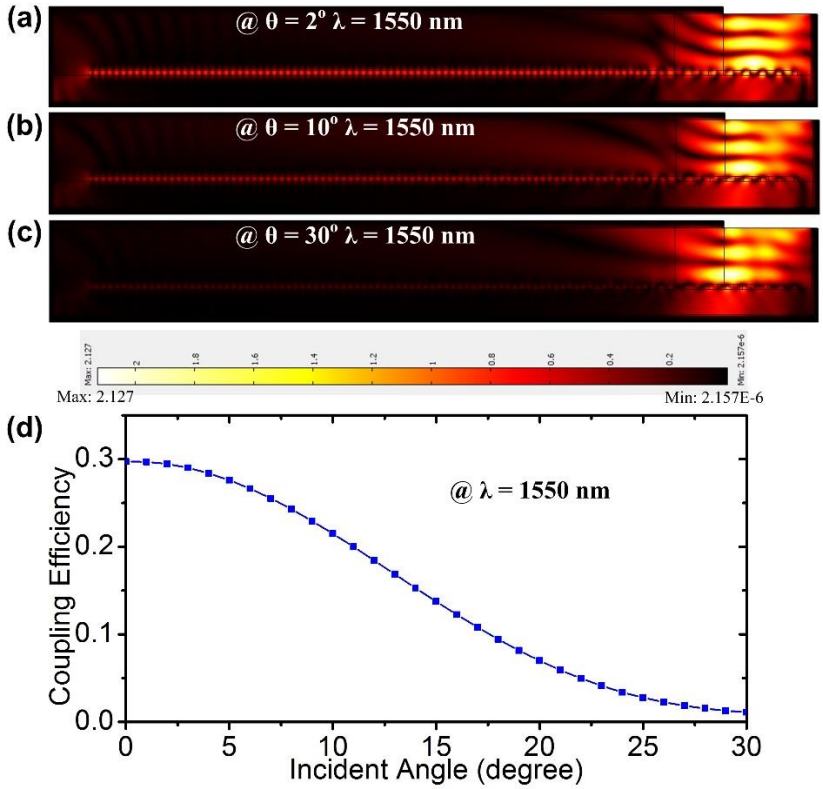

Figure 2.14 (a-c) Electric field distribution throughout the grating coupler with wavelength of 1550 nm at incident angle of 2° (a), 10° (b), and 30° (c). (d) Efficiency of the grating coupler with respect to incident angle with wavelength of 1550 nm.

2.7 Conclusion

In this chapter, we discussed the nanofabrication techniques used for silicon photonic devices, including e-beam lithography, reactive ion etching, we etching, metallization, and lift-off. We successfully demonstrated the realization of integrating a cantilever into a PC structure using the nanofabrication techniques. Also, we studied grating coupling technique for coupling light into and out of a silicon photonic device. A coupling efficiency of 5-30% was obtained.

References

[1] C. Vieu, F. Carcenac, A. Pepin, Y. Chen, et al, “Electron beam lithography: resolution limits and applications,” *Applied Surface Science*, Vol. 164, pp. 111−117, 2000.

[2] T. H. P. Chang, M. Mankos, K. Y. Lee, and L. P. Muray, “Multiple electron-beam lithography,” *Microelectronic Engineering*, Vol. 57, pp. 117−135, 2001.

[3] A. Tseng, K. Chen, C. D. Chen, and K. J. Ma, “Electron beam lithography in nanoscale fabrication: recent development,” *IEEE Transactions on Packaging Manufacturing*, Vol. 26, pp. 141−149, 2003.

[4] J. A. Liddle, G. M. Gallatin and L. E. Ocola, “Resist requirements and limitations for nanoscale electron-beam patterning,” *Mat. Res. Soc. Symp. Proc.*, Vol. 739, pp. 19−30, 2003.

[5] D. Taillaert, F. Van Laere, M. Ayre, W. Bogaerts, D. Van Thourhout, P.Bienstman, and R. Baets, “Grating couplers for coupling between optical fibers and nanophotonic waveguides,” *Jpn. J. Appl. Phys.*, Vol. 45, pp. 6071−6077, 2006.

[6] Chao Li, Huijuan Zhang, Mingbin Yu, and G. Q. Lo, “CMOS-compatible high efficiency double-etched apodized waveguide grating coupler,” *Opt. Express*, Vol. 21, pp. 7868–7874, 2013.

[7] X. Xu, H. Subbaraman, J. Covey, D. Kwong, A. Hosseini, et al., “Complementary metal–oxide–semiconductor compatible high efficiency subwavelength grating couplers for silicon integrated photonics,” *Appl. Phys. Lett.*, Vol. 101, pp. 031109–1–4, 2012.

[8] P. Yeh, A. Yariv, and C. S. Hong, “Electromagnetic propagation in periodic stratified media. I. General theory,” *J. Opt. Soc. Am.*, Vol. 67, pp. 423–438, 1977.

CHAPTER 3. OPTICAL PROGRAMMABLE PHOTONIC INTEGRATED CIRCUIT

3.1 Background

Generally, PICs are promising to construct photonic networks with low cost, low power consumption, and small device footprint. As introduced in Chapter 1, 2D PC possesses remarkable abilities to confine and propagate light at the wavelength scale [1]. There has been increasing interest in using PC slabs to develop various photonic devices, including waveguides, splitters, lasers, spectral filters, interferometers, mirrors, lenses, switches, and add-drop multiplexers. Most of existing PICs reported to date, however, are static or have very limit tunability. We are interested in developing a relatively universal PIC platform that can allow reconfiguring a variety of different photonic building blocks, interconnects, and even complex circuits dynamically at desired locations of a single photonic chip through digital programming.

In this Chapter, we develop an optical programmable PIC by leveraging the advantages of three technologies: PC, digital micromirror devices (DMD) [2], and photo-responsive liquid crystals (LC) [3]. Briefly, periodically distributed air holes of a 2D PC slab are infiltrated with photo-responsive LCs. The DMD is programmed to project different light patterns of a pump light onto the surface of the PC slab. The LC molecules trapped in the air holes respond to the light by changing their relative permittivity (refractive index). The use of the DMD allows individual addressing each hole and modulating the effective index of each cell. The most basic photonic element to build up various PC-based devices is single-defect cavity. A series of single defects can form a line defect PC waveguide with excellent light guiding capability. By projecting a spot of the pump light onto a LC-infiltrated hole or a group of neighboring holes, the effective refractive index of the illuminated region can be

changed, forming a point defect. Furthermore, by optically introducing multiple point defects to different regions of the PC slab, it is possible to configure different PIC devices, such as straight waveguide and waveguide bends on a single photonic chip (Fig. 3.1).

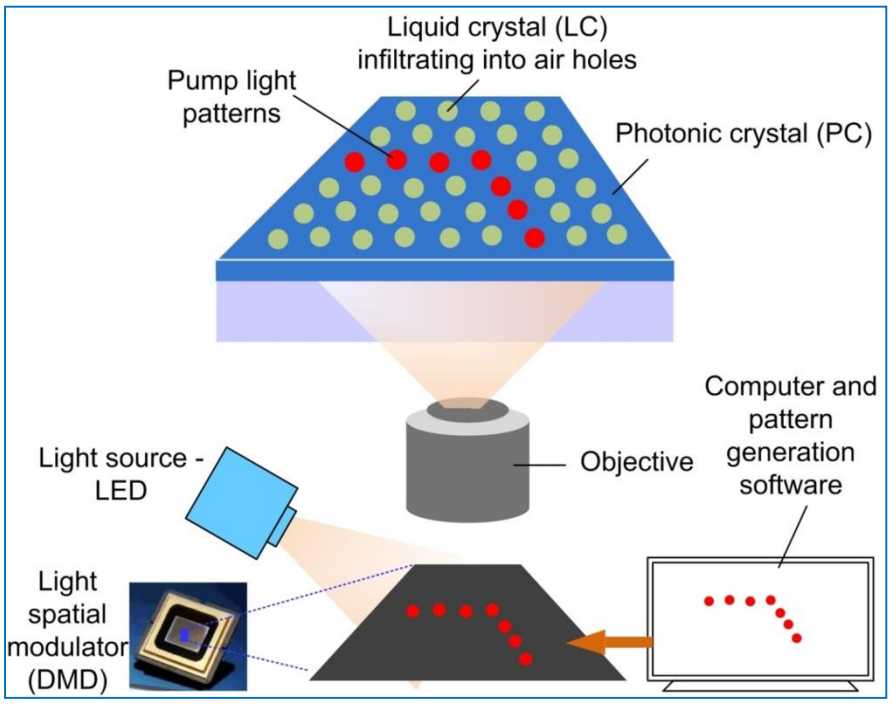

Figure 3.1. Schematic for an optical programmable PIC.

3.2 Light-sensitive Liquid Crystal

LC has a strong impact in the PC research field [4]. Nematic LC is a birefringent medium with a uniaxial symmetry. The molecule shape and its long-range order of nematic LC are at the origin of its optical anisotropy. The molecular order and refractive index of a LC can be easily modulated by means of different external stimuli, such as electric field, temperature, and light. When interacting with nematic LC, light experiences the ordinary refractive index (n_o) or the extraordinary refractive index (n_e) if the electric field is polarized perpendicular or parallel to the axis of LC molecules, respectively. Specifically, by applying an electric field, the molecular orientation of the LC with respect to the polarization direction

of a light beam propagating through it can be tuned. Moreover, when the temperature is increased above the nematic-isotropic phase transition temperature, the molecular order is destroyed and the LC is in its isotropic phase: its optical properties are thus characterized by an isotropic refractive index (n_i) that is independent of the molecule orientation. Finally, when nematic LCs are mixed with photosensitive molecules, the latter phase transition can be photoinduced isothermally by light irradiation at certain wavelengths. All these tuning mechanisms are reversible and they have been exploited to tune the optical properties of photonic crystal structures infiltrated with nematic LC [5]. Here in this chapter, we describe an optically reconfigurable PC infiltrated by photosensitive LCs and reconfigured by a DMD to maximize reconfigurability [6].

LC is characterized by ultrahigh constants of nonlinear refraction, $n_2 \sim 10^{-4} - 1$ cm^2/W and $\delta n \sim 0.3$ ($\delta n = n_2 I_0$ is the change in the effective refractive index of LC induced by a light beam of peak intensity I_0) [3]. These large constants of nonlinear refraction result from optically induced collective reorientation of LC molecules. The torque acting on the LC orientation is present for a particular component of light beam polarization and requires special geometrical conditions for its realization. Isotropic materials, including the isotropic phase of LCs, are free from these disadvantages. Constants of nonlinear refraction of photoinduced isotropic (PI) phase of azobenzene LCs are comparable to that of LC mesophases.

The basic process of obtaining the PI state of an azo LC consists in subjecting it to radiation in the blue-green region of wavelengths; trans-cis photoisomerization of azobenzene molecules reduces the order parameter of azo LCs thus driving them into their isotropic phase upon accumulation of a critical concentration of the non-mesogenic cis form

of azo molecules [3]. The PI state of azo LCs can last over tens of hours since dark relaxation is governed by the lifetime of cis isomers at fixed temperature.

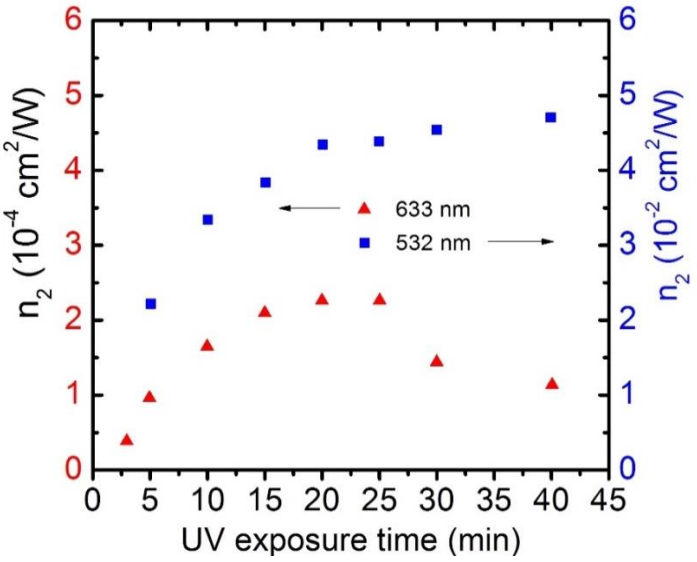

Figure 3.2 The constant of nonlinear refraction of azo LC 1205 as a function of UV-exposure time at the wavelengths λ = 633 nm and λ = 532 nm.

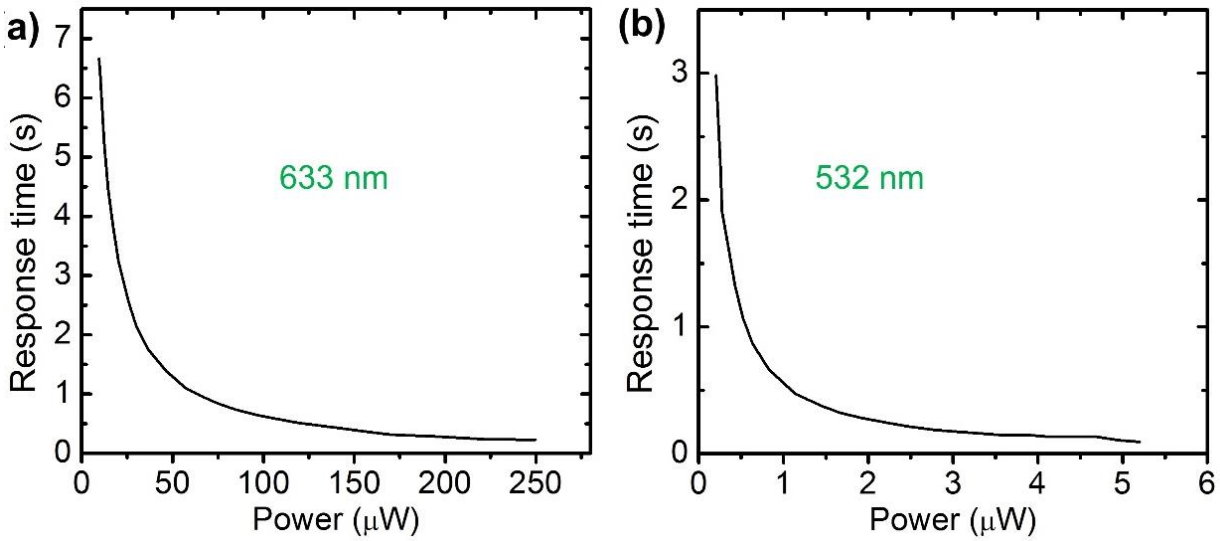

Figure 3.3 The response time vs laser beam power for (a) λ =633 nm and (b) λ = 532 nm.

The constant of nonlinear refraction n_2, as seen in Fig. 3.2a, increases with increasing UV-exposure time, hence with increasing cis content of the material. Values of n_2 exceeding 10^{-4} cm^2/W and 10^{-2} cm^2 /W for the wavelengths 633 nm and 532 nm were obtained with

UV-exposure time of about 30 min. One of the unusual features of the mechanism of the optical nonlinearity under discussion was the increase of n_2 with increasing radius of the laser beam acting on the material. The response time decreases with increasing power of radiation reaching $\tau \sim 100$ ms for P = 250 μW at $\lambda = 633$ nm and for P = 3 μW at $\lambda = 532$ nm (Fig. 3.3). In the following study, we choose UV exposure time to be 35 minutes and choose green light (532 nm) as actuation light with $n_2 \sim 2.3 \times 10^{-2}$ cm^2/W. The waist radius of the green beam is set to 50 μm. Thus if the power of condensed green beam is at or above 0.721 mW, relative permittivity ε_r of LC 1205 can be tuned from 3.2 to 4.

3.3 Digital Micromirror Devices

A digital micromirror device, or DMD, is an optical semiconductor device that is the core of Digital Light Processing (DLP) technology [2]. The DMD used in this study has one million of microsized mirrors arranged in a rectangular array which correspond to the pixels in the image to be displayed. The mirrors can be individually rotated ±10-12°, to an on or off state (Fig. 2). In the on state, light from the projector bulb is reflected into the lens making the pixel appear bright on the screen. In the off state, the light is directed elsewhere, making the pixel appear dark.

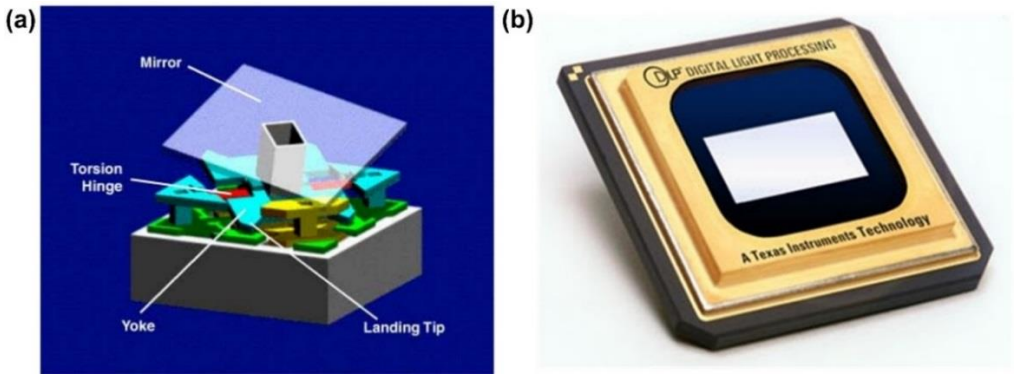

Figure 3.4 (a) Schematic of one pixel mirror of DMD; (b) A typical DMD product.

Each pixel mirror in DMD is a MEMS structure was monolithically integrated over a silicon address circuit. Thus by individually control the state of each unit pixel, DMD can project a beam with a desired pattern. Here in this chapter, we use the DMD to deliver optical patterns of a pump light onto the surface of PC, to modulate local refractive index of the light-responsive LC in the periodic holes of a PC. The size of each pix mirror of this DMD is 10.2 × 10.2 μm, and its resolution is 10 μm without optics. We use a reflective microscope objective to condense the beam, improving the resolution to 1-2 μm.

3.4 Theoretical Study on Liquid Crystal-based Photonic Crystal Slab

Our theoretical study on the LC-infiltrated PC slab begins with investigating its band diagram. The 2D PC slab has a triangular lattice with periodicity of $\boldsymbol{a}$. The thickness and diameter of holes are set to 0.6 $\boldsymbol{a}$ and 0.8 $\boldsymbol{a}$, respectively, which can bring a large bandgap and a wide range in the working wavelength. Normalized band diagram in plane for transverse-magnetic (TM)-like modes is shown in Fig 3.5. As mentioned in Chapter 1, the light line represents boundary condition for total internal reflection. All modes above light line have significant radiation loss while all other modes in the region below it (light cone) can be vertically confined in the slab. Figure 3.5 shows that for TM-like case, the band of modes in light cone can reach all the frequencies. Thus, there is no bandgap for TM-like modes. In the following study we just consider TE-like case.

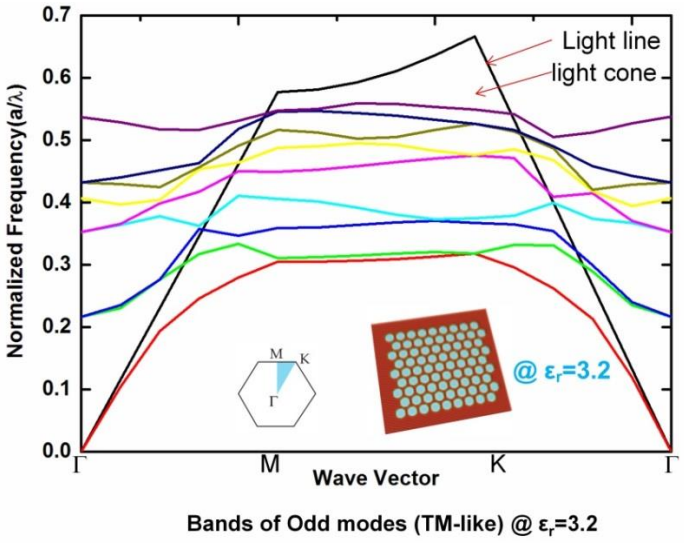

Figure 3.5 TM-like band diagram of PC slab when the dielectric constant of LC ε_r is 3.2.

LC's Photonic bandgaps of TE-like modes for ε_r = 3.2 and 4.0 are shown in Fig. 3.6. The result demonstrates that the TE-like bandgap ranges from 0.2643 $\boldsymbol{a}$ / λ to 0.3282 $\boldsymbol{a}$ / λ at ε_r = 3.2. The central frequency is 0.2963 $\boldsymbol{a}$ / λ, and we can fix the central wavelength at the communication wavelength 1550 nm, by setting the periodicity $\boldsymbol{a}$ to be 459 nm. The maximum ε_r can be 4.0, obtained by increasing power of the green actuation beam. At ε_r = 4.0 the bandgap spans from 0.2598 $\boldsymbol{a}$ / λ to 0.3034 $\boldsymbol{a}$ / λ. Correspondingly, the central wavelength shifts from 1550 nm to 1630 nm. The tuning range of working wavelength is thus 80 nm.

Without being actuated by the green beam, LC inside each unit hole in PC slab has initial relative permittivity of 3.2. To form a single point-defect resonant cavity in the PC slab, there will be only one hole changing its relative permittivity by DMD-patterned light. Suppose the relative permittivity is tuned to be 4.0. We conduct electromagnetic simulation using the 3D FDTD method with the freeware package MEEP [7]. A TE-polarized pulse line source with a Gaussian frequency distribution is placed vertically along the Z direction and

offset by 20 nm from the spatial center of the target hole. The line source is set at the same height as the PC slab. The resonance wavelength and Q factor of the resonant cavity are computed by the Harminv [8]. To record mode profiles, a continuous-wave line source at the specific resonance is used. For this single point-defect cavity, two modes are observed (Fig. 3.7). According to the field distribution, one is monopole and the other is dipole. The monopole mode works at 1670.1 nm with Q factor of 165 while the dipole one works at 1577.9 nm with Q factor of 195.

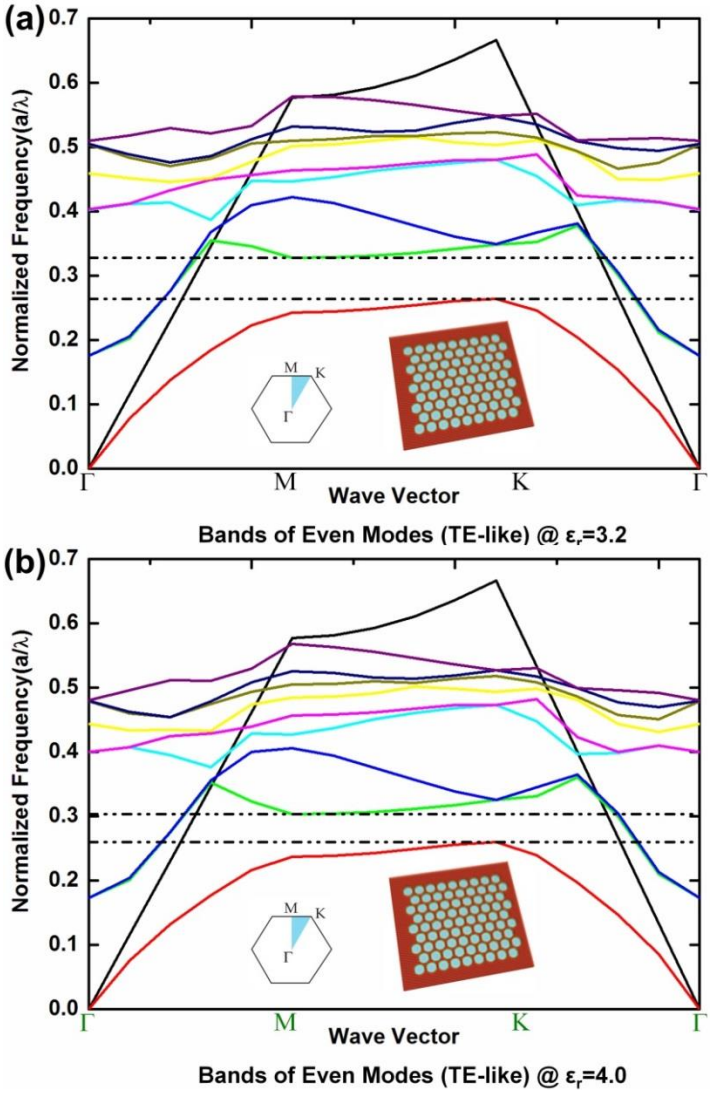

Figure 3.6 TE-like band diagrams of the LC-filtrated PC slab at ε_r = 3.2 (a), 4.0 (b).

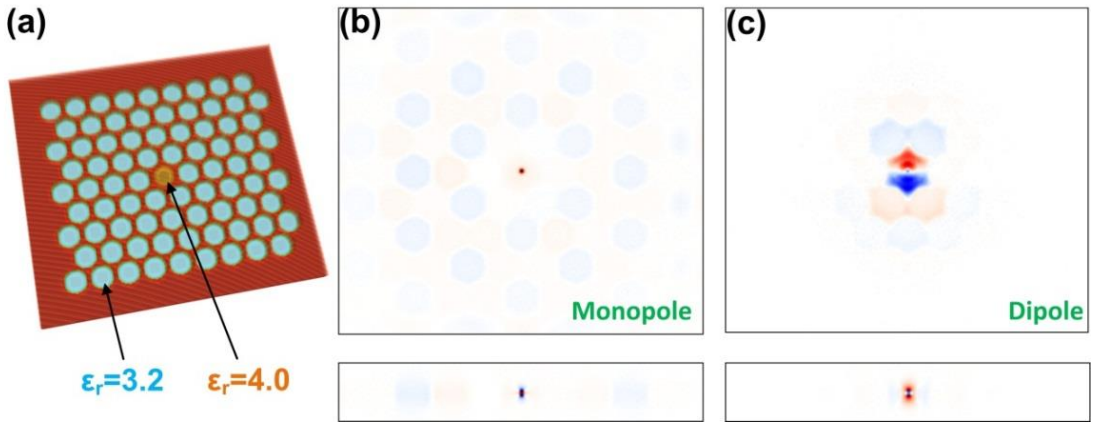

Figure 3.7 (a) Point-defect cavity with LC unit and its monopole (a) and dipole (b) resonant modes.

To configure a straight waveguide in the PC, the relative permittivity of the LC in one line of hole units is actuated to 4.0. We compute the band diagram (dispersion curves) for the waveguide along the Γ-X direction of the triangular lattice in wave-vector space, using the 3D PWE method. As shown in Fig. 3.8a, the supercell for this simulation contains one period in the Γ-X direction, six periods in the X-M direction (normal to the Γ-X direction), and only one period in the center has dielectric constant of 4.0. From Fig. 3.8b, we find a few bands of modes in the photonic bandgap, spanning from 0.2839 $\boldsymbol{a}$ / λ to 0.2964 $\boldsymbol{a}$ / λ. That means light with any frequency within this range could be guided along the straight waveguide. We select one frequency 0.296 $\boldsymbol{a}$ / λ which is close to the upper edge for further investigation. Figure 3.9 shows the mode profile of the straight waveguide at frequency of 0.296 $\boldsymbol{a}$ / λ. The electric field is confined in the center of the supercell in three dimensions. To further verify light propagation of straight waveguide, we use the FDTD method to simulate the mode profile at 0.296 $\boldsymbol{a}$ / λ. As shown in Fig. 3.10, the light can be guided well through both a line-defect waveguide and an L-shape waveguide bend.

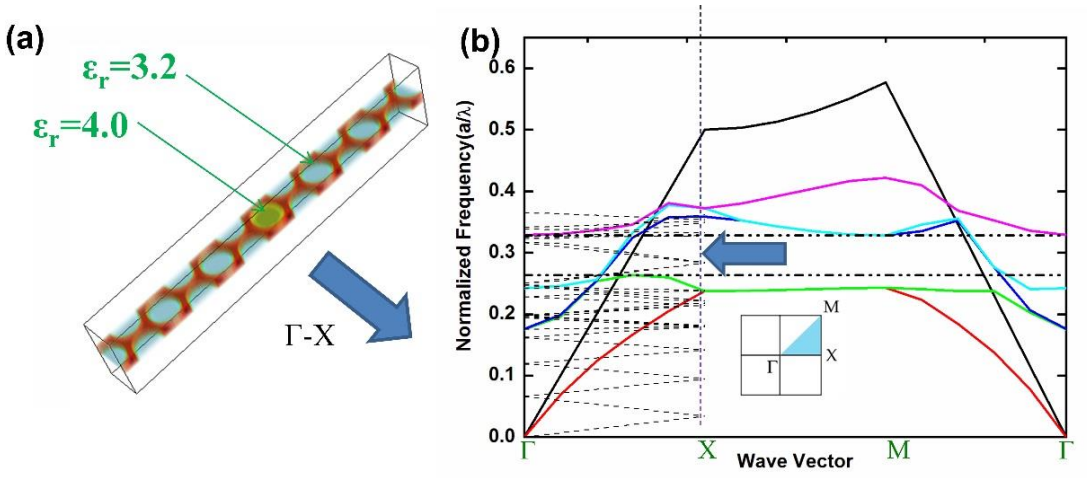

Figure 3.8 (a) Supercell used for simulating line-defect waveguide mode of an LC-infiltrated PC slab by PWE method. (b) Band diagram for line-defect waveguide mode.

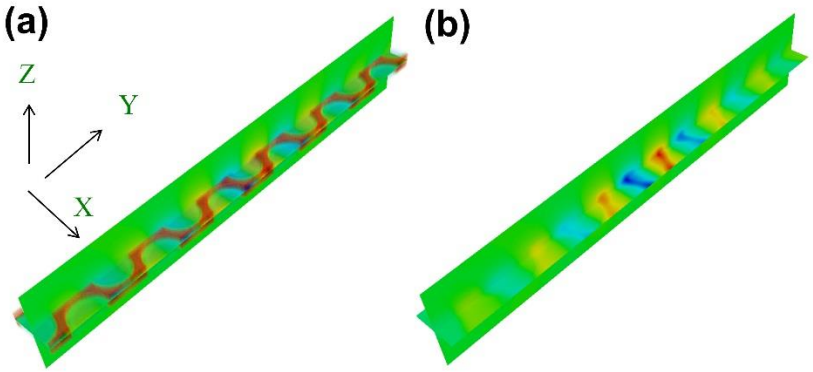

Figure 3.9 Mode profiles of line-defect waveguide mode at a frequency of 0.296 **a** / λ calculated by PWE method with (a) and without (b) dielectric constant distribution.

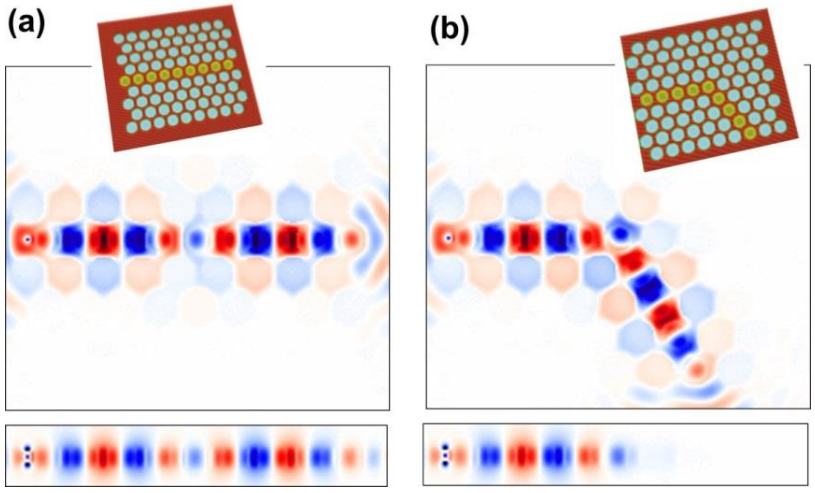

Figure 3.10 Mode profiles of a straight waveguide (a) and an L-shape waveguide bend (b) at a frequency of 0.296 ***a*** / λ calculated by FDTD method.

3.5 Device Fabrication and Characterization

As shown in Figure 3.11, the device is fabricated on an SOI wafer using e-beam lithography and reactive ion etching. Here, a microfluidic approach is employed to fill the air holes of the PC slab with the LC molecules, as described in Figs. 3.11c-d. We use plasma treatments to increase the surface energy and thus to improve the wettability of device [9]. SEM images of the whole devices after E-beam lithography and RIE are shown in Fig. 3.12.

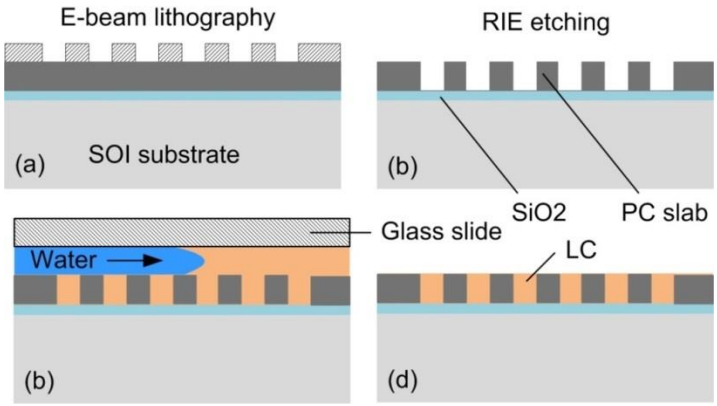

Figure 3.11 Device fabrication. (a-b) Fabrication of PC slab. (c-d) A glass slide is place on top of the fabrication PC slab with an air gap of 500 μm. Photoresponsive LC is then infiltrated into the holes of the slab. Water is flowed into the gap to remove the excess LC from the surface of the device.

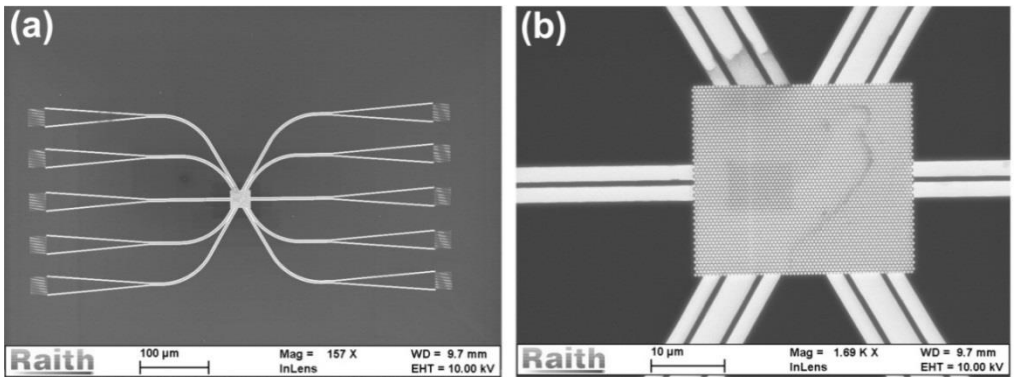

Figure 3.12 (a) Overview and (b) close-up SEM images of the device.

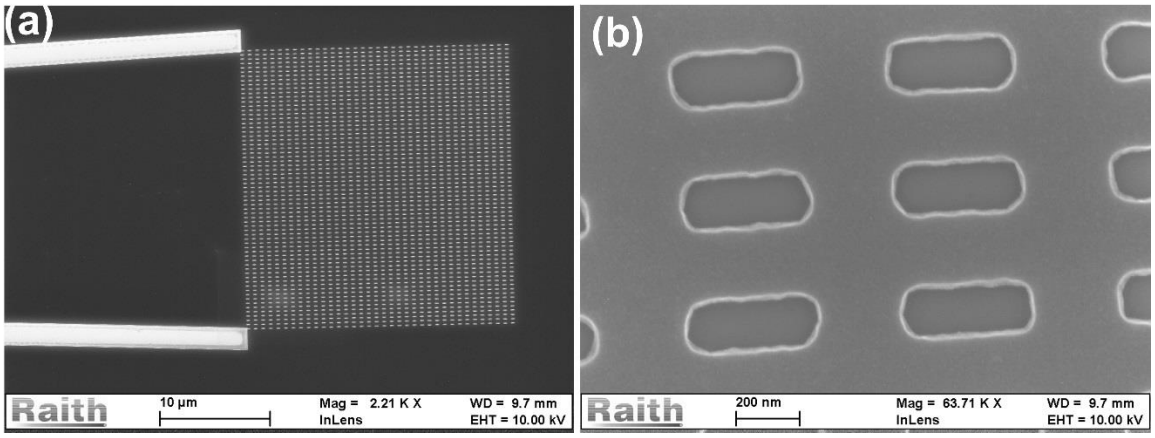

Figure 3.13 (a) Overview and (b) close-up SEM images of a 2D grating coupler.

To demonstrate the programmable PIC device concept, the LC-infiltrated PC region is located at the center of the device with five input and five output grating couplers. The probe light comes from a 1.55 µm tunable laser and is then incident onto the input coupler region. 2D grating couplers are fabricated and integrated in the thin silicon layer of the SOI wafer to couple the probe light into and out of the device through the on-chip tapered waveguides as shown in Fig. 3.13. The testing setup is shown in Fig. 3.14.

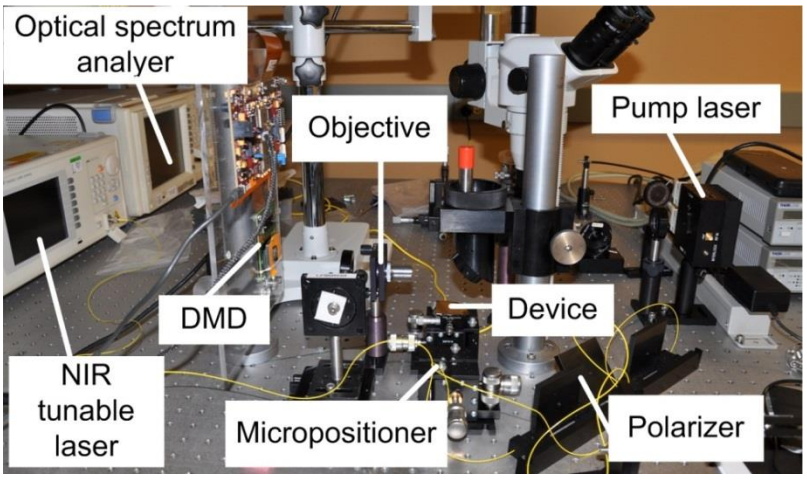

Figure 3.14 Testing setup for the optical programmable PIC.

Using the fabricated device, we demonstrate to generate three different optical components via digital programming: a straight waveguide and a point-defect acting as cavity filter. The feature size D of the pump light pattern is tuned from 1.0 μm to 4.0 μm, while the intensity I is varied from 3 to 9 W/cm^2.

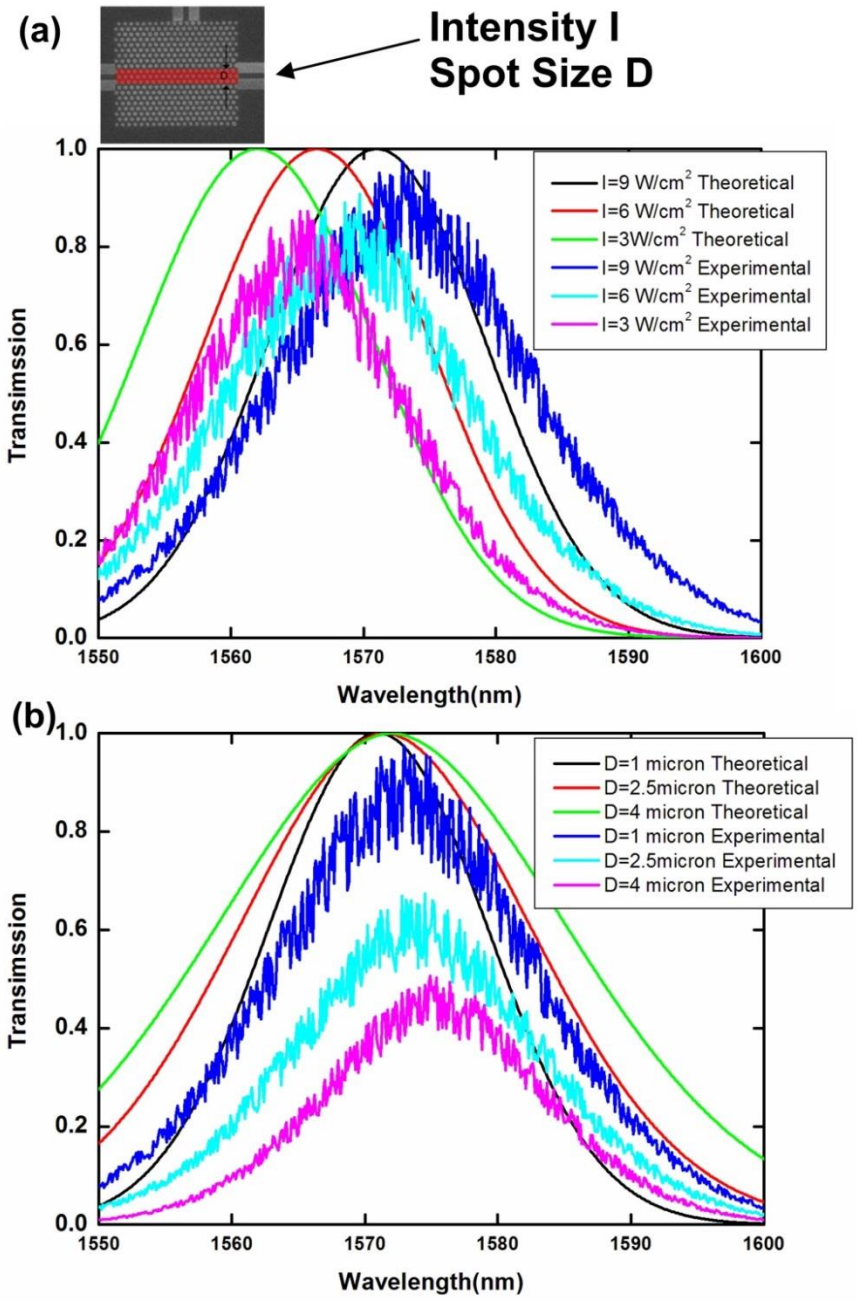

Figure 3.15 Transmission of a point-defect cavity generated by the pump light with respect to different light intensities I at the spot size D = 1 μm (a) and different spot sizes D at the intensity I = 9 W/cm^2 (b).

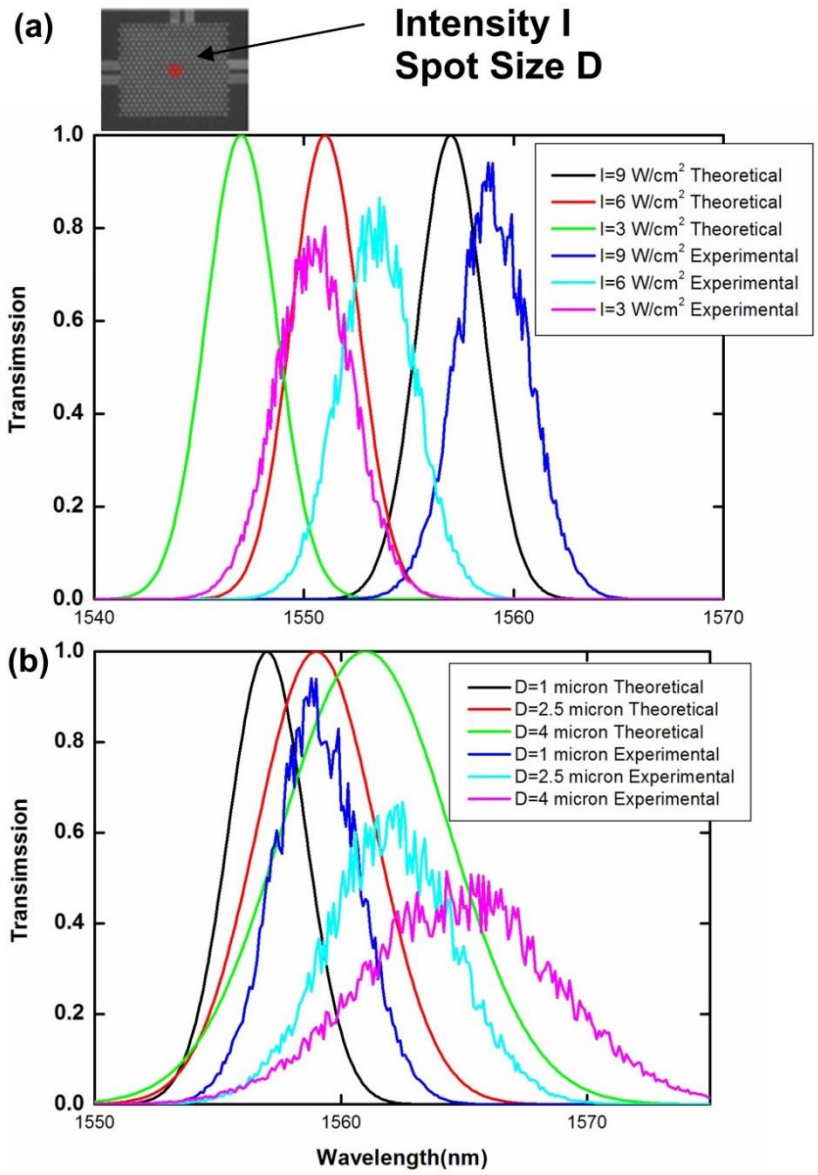

Figure 3.16 Transmission of a point-defect cavity generated by the pump light with respect to different light intensities I at the spot size D = 1 μm (a) and different spot sizes D at the light intensity I = 9 W/cm^2.

The line defect waveguide is formed between the input port and the output port by projecting a straight light pattern onto the device surface. By scanning the probe light wavelength from 1550 nm to 1600 nm, the maximum output signal power is found at 1565.4 nm at D = 1 μm and I = 3 W/cm^2. As shown in Fig. 3.15a, by increasing I from 3 to 9 W/cm^2, the transmission has a red shift of 10 nm. Both theoretical and experimental results have

similar trend. Increasing light intensity results in increasing refractive index in the line defect. Thus the defect mode red shifts. Figure 3.15b shows the normalized transmission when D increases from 1 μm to 4 μm. Both the theoretical and experimental results have a limited wavelength shift, but a significant change in transmittance. This is because the large spot size modulates more periods than what we expected and the light confinement in the perpendicular direction gets worse.

Finally, the pump light spot is incident onto the device surface to form a PC point-defect resonant cavity between the input port and the output port. At D = 1 μm and I = 3 W/cm^2, the experimental resonance peak is found at 1551.2 nm. As shown in Fig. 3.16, we increases the intensity I from 3 to 9 W/cm^2, and a similar red shift is obtained for the transmission peak, which is corresponding to wavelength of resonant mode in the cavity. This is an important characteristic since it can be used for filtering signal around communication wavelength by just changing the pump light power intensity. By setting I to be 9 W/cm^2, the spot size D significantly affects the performance of the cavity. As shown in Fig. 3.16b, the Q factor degrades when D increases from 1 μm to 4 μm. Also the transmittance gets lowered since the resonant cavity becomes more lossy due to the increasing size. The slight difference between the simulation and experiment results can be explained by inaccurate initial LC refractive index chosen for the simulation, and non-optimum contrast between dark and illuminated regions in the testing.

3.6 Conclusion

In this chapter, we develop an optical programmable PIC device by infiltrate 2D PC slab with and photo-responsive LC. The DMD is programmed to actuate LC by projecting a

pump light at a wavelength of 532 nm onto the device surface. We both theoretically and experimentally demonstrate a point-defect cavity, a straight waveguide and a waveguide bend on this programmable PIC device.

References

[1] Y. Akahane, T. Asanol, B. S. Song and S. Noda, "High-Q photonic nanocavity in a two-dimensional photonic crystal," *Nature*, Vol. 425, pp. 944−947, 2003.

[2] http://www.ti.com/lit/an/dlpa008a/dlpa008a.pdf

[3] N. Tabiryan, U. Hrozhyk, and S. Serak, "Nonlinear refraction in photoinduced isotropic state of liquid crystalline azobenzenes," *Phys. Rev. Lett.*, Vol. 93, pp. 113901−1−4, 2004.

[4] D. Kang, J. E. Maclennan, N. A. Clark, A. A. Zakhidov, and R. H. Baughman, "Electrooptic behaviour of liquid-crystal-filled silica opal photonic crystals: effect of liquidcrystal alignment," *Physical Review Letters*, Vol. 86, pp. 4052-4055, 2001.

[5] G. Alagappan, X. W. Sun, M. B. Yu, and P. Shum, "Controllable polarization splitting in liquid crystal infiltrated photonic crystals," *Proceedings of SPIE - Photonic Crystal Materials and Devices IV*, Vol. 6128, pp. 61280H-1, 2006.

[6] V. K. S. Hsiao, Y. B. Zheng, B. K. Juluri, T. J. Huang, "Light-driven plasmonic switches based on Au nanodisk arrays and photoresponsive liquid crystals," *Advanced Materials*, Vol. 20, pp. 3528-3522, 2008.

[7] A. F. Oskooi, D. Roundy, M. Ibanescu, P. Bermel, J. D. Joannopoulos, and S. G. Johnson, "MEEP: A flexible free-software package for electromagnetic simulations by the FDTD method," *Comput. Phys. Commun.*, Vol. 181, pp. 687−702, 2010.

[8] V. A. Mandelshtam and H. S. Taylor, "Harmonic inversion of time signals and its applications," *J. Chem. Phys.*, Vol. 107, pp. 6756−6769, 1997.

[9] D. Myers, *Surfaces, Interfaces and Colloids*, Wiley-VCH, Weinheim, 1991.

CHAPTER 4. NANO-ELECTRO-MECHANICAL SYSTEMS RECONFIGURABLE PHOTONIC CRYSTAL

4.1 Background

In the previous Chapter 3, photo-responsive LC is infiltrated into the air holes of a PC slab and modulated by a pump laser beam. The response time of photo-responsive LC is at the level of 100 ms and the lifetime is limited [1]. Unfortunately, it's not easy to find an alternative liquid or soft matter that may be able to alleviate the issues of the slow response time and limited lifetime, while possessing a high ability to modulate refractive as much as photo-responsive liquid crystal.

To overcome the problem, we proposed to electromechanically modulate local effective refractive index for each photonic unit in a PC, to maximize flexibility to tune optical properties of the PC. Electrostatic actuator is one of the simplest and effective MEMS actuation technologies to generate a precise displacement in a micro/nanometer range for a movable cantilever or membrane. We chose this type of actuator to perform a desired index modulation function for each unit of a PC, because of its ease to embed into a PC structure. Basically, each unit of a PC is constructed as part of an electrostatic actuator. A linear array of electrostatic actuators is formed to realize a tunable 1D PC. As controlled electrostatic forces are able to drive different units in the PC to move up and down, the local effective refractive indices of these units will be tuned, thus changing optical properties of the PC.

In this chapter we will first theoretically investigate electromechanical properties of a nanobeam electrostatic actuator and optical characteristics of a 1D PC formed by an array of nanobeam electrostatic actuators. Then, we will describe the design and fabrication of the nanobeam-based reconfigurable PC structure. Lastly, we will demonstrate the

reconfigurability of the device by a showcase of different photonic functionalities realized on a single device via reconfiguring the photonic bandgap of the device.

4.2 Inspiration of Distributed Bragg Reflector

A distributed Bragg reflector (DBR) is a reflector used in waveguides such as optical fibers [2]. It is a structure formed from multiple layers of alternating materials with different refractive indices, or by periodic variation of some characteristic, such as height, of a dielectric waveguide, resulting in periodic variation in the effective refractive index in the waveguide. Each layer boundary causes a partial reflection of an optical wave. For waves whose wavelength is close to four times the optical thickness of the layers, the many reflections combine with constructive interference, and the layers act as a high-quality reflector. It should be pointed out that essentially, a DBR stack is a simple example of a 1D PC and an excellent reflector for laser application, consisting of alternating layers of two different materials [3]. The range of wavelengths that are reflected is called the photonic bandgap.

Figure 4.1 shows transmittance of a typical DBR stack. In this DBR stack, the periodicity is 1 μm, the high index layer is silicon stack with a thickness of 0.75 μm while the low index layer is air with a thickness of 0.25 μm. The first (fundamental) photonic bandgap is located in the wavelength range from 2.74 μm to 3.50 μm. The DBR has an infinite number of high-order bandgaps in high-frequency or low-wavelength ranges. As shown in Fig. 4.1, width of high-order wavelength bandgap decreases as order number increases. Generally a low-order bandgap is preferred in most applications such as laser cavity, due to its width and high quality.

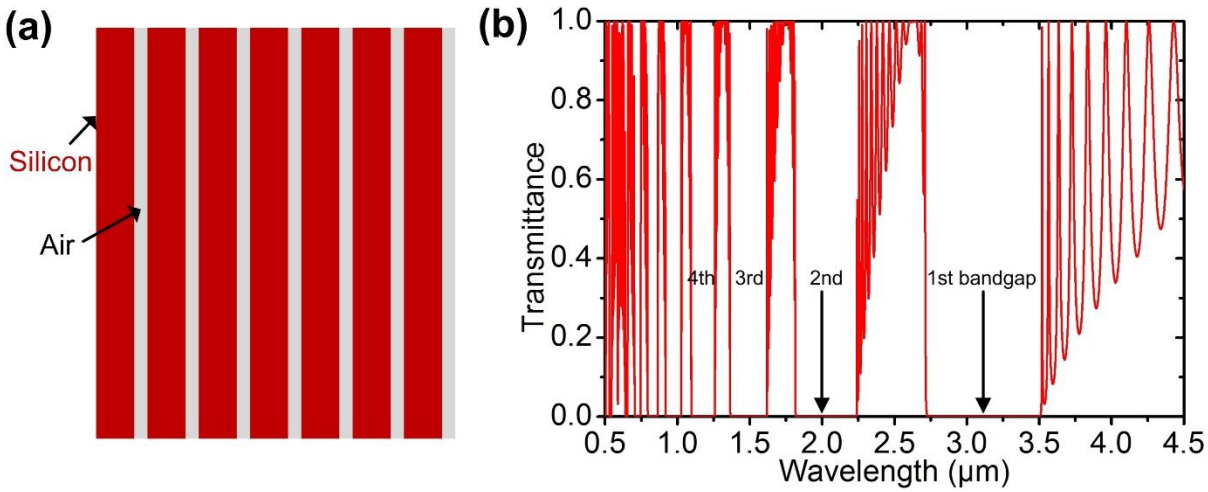

Figure 4.1 (a) Schematic and (b) transmittance of a typical DBR stack.

4.3 Structure of Reconfigurable 1D Photonic Crystal

Essentially, DBR is a special case of 1D PC. Now we introduce nanobeam [4] structure into DBR as one unit of PC. Since nanobeam is a cantilever structure which can be individually and electrostatically actuated in MEMS technology, the nanobeam-based DBR can be taken as a 1D reconfigurable PC structure.

Figures 4.2a shows the schematic for the proposed reconfigurable PC. In horizontal (X) direction the reconfigurable PC is sandwiched by a tapered feeding waveguide and a tapered output waveguide. In Y direction there are two symmetric and periodic array of 1 μm spaced silicon nanobeams. The gap distance between two adjacent nanobeams is 250 nm. The nanobeams are all suspended and only anchor at two ends. The central silicon space defect of each nanobeam forms a unit of the reconfigurable PC structure. The nanobeam is 20 μm long, and 750 nm wide. The periodicity and diameter of air holes in the nanobeam is 500 nm and 400 nm, respectively. The whole device is configure on top silicon layer of SOI wafer with thickness of 200 nm.

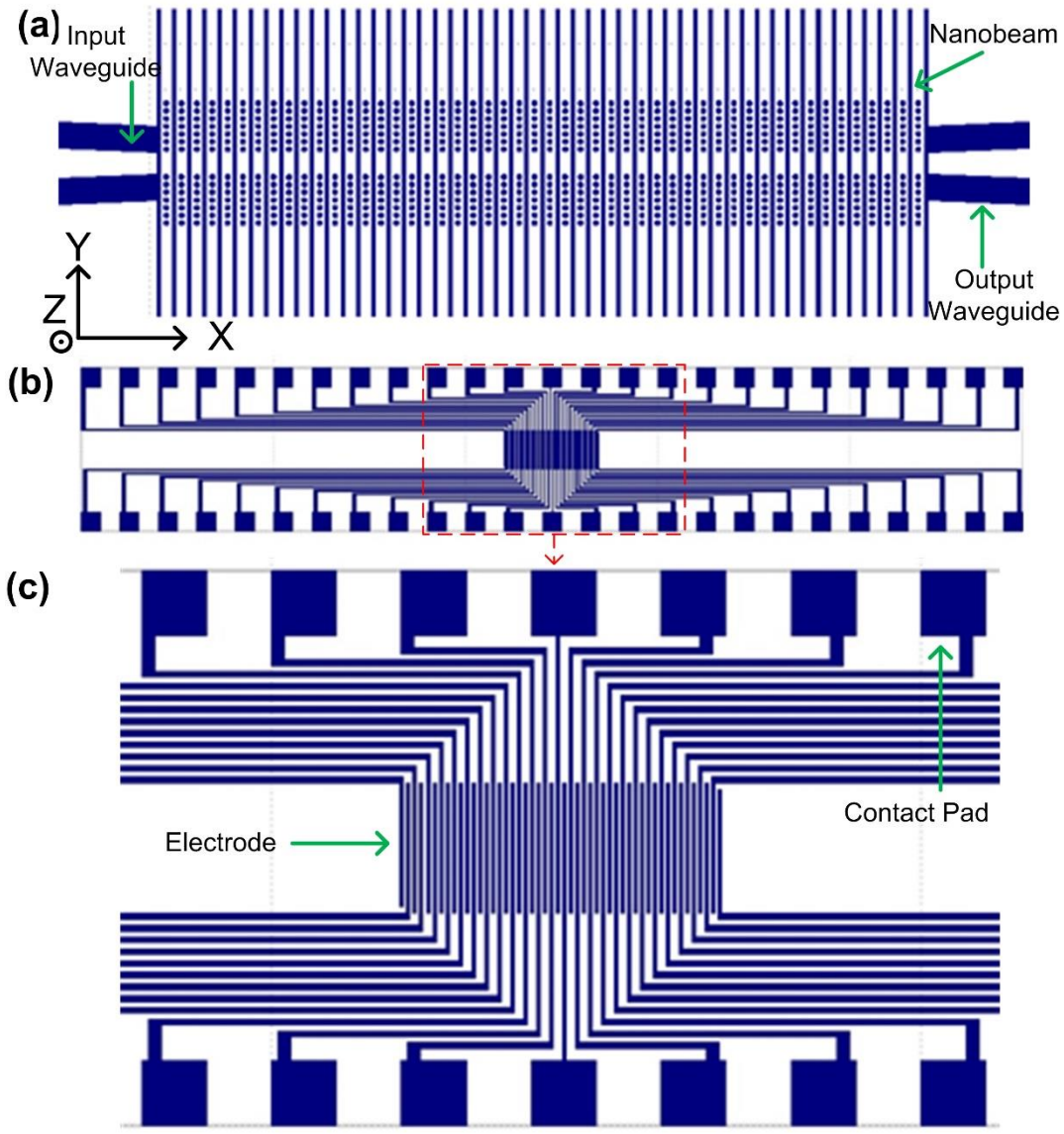

Figure 4.2. (a) Schematic of reconfigurable PC structure; (b) overview (c) close-up of pattern for electrodes.

Essentially, each silicon nanobeam in the proposed device could be considered as a 1D PC-based optical resonant cavity in Y direction [4]. The periodic air holes on the two sides of the nanobeam in Y direction (see Fig. 4.2a) enable creating a wide photonic bandgap to confine the light in Y direction. On the other hand, the light is confined vertically by index guiding in Z direction across the thickness of the nanobeam. It should be pointed out that the linear array of optical resonant cavities constructs a special PC waveguide in X direction. In other words,

light propagation along this special waveguide is determined by the periodically arranged optical cavities of the nanobeams. To individually control nanobeams, an array of nanoelectrodes is placed above and aligned with the nanobeams with a gap of one micrometer in Z direction (Fig. 4.2b and Fig. 4.2c). Because the nanobeams are all connected as an electrical ground, applying a voltage to an individual nanoelectrode though its contact pad will allow driving the corresponding nanobeam to move out of the plane, thus changing the local effective refractive index in X direction. With this unique reconfigurable PC design and flexible index manipulation method, we will be able to reconfigure different optical functionalities on the proposed device. The gold nanoelectrodes are fabricated by E-beam lithography, metal evaporation, and lift-off processes, as described in Section 2.2 and 2.5.

4.4 Theoretical Study

To theoretically investigate the influences of voltages applied to the nanoelectrodes though contact pad on optical characteristics of the reconfigurable PC, we first need to perform simulations to obtain the relation between mechanical deflections of the nanobeams and applied voltages. Then we study the relation between optical characteristics of the reconfigurable PC structure and deflections of the nanobeams.

The deflections of the silicon nanobeam under different applied voltages were simulated by using commercial FEM software COMSOL Multiphysics [5]. We set up the simulation model with exactly the same dimensions as the designed nanobeam (200 nm thick, 750 nm wide, and 20 μm long). Since nanoelectrodes is placed above and aligned with nanobeams with a gap of one micrometer in vertical direction, in the model we placed a plane in parallel to nanobeam with a gap of one micrometer. The top silicon is heavily doped with

boron (hole concentration: $10^{21}/cm^3$). Young's modulus of the silicon and is set to be 150 GPa, and the Poisson's ratio of silicon is fixed at 0.17. The model uses the electromechanics interface to solve the coupled equations for the structural deformation and the electric field. The electrostatic field in the air and in the beam is governed by Poisson's equation.

As a voltage is applied between the top surface of the cantilever and the other electrode, the cantilever bends from its initial bending. Figure 4.3a shows the simulated bending profiles of the beam under an applied voltage of 22 V. Figure 4.3b showed that the vertical deflection at the center of the beam is not linear with, but close to quadratic to an applied voltage. The deflection is 2.9, 25.8, 102.0, and 274.8 nm when the applied voltage is 5, 15, 30, and 50 V, respectively.

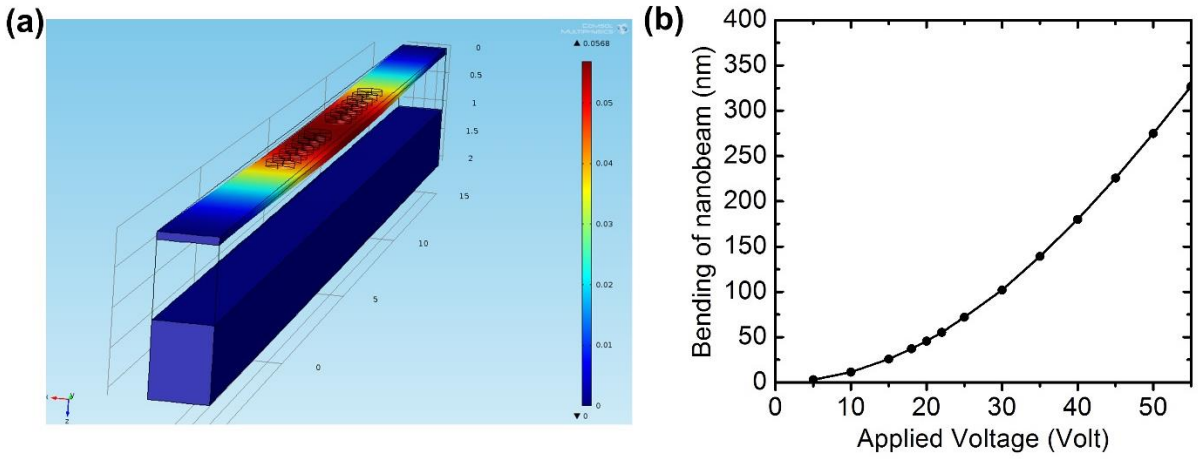

Figure 4.3 (a) Bending profile of the nanobeam with an applied voltage of 22 V (b) Deflections at the center of the cantilever as a function of applied voltages.

The nanobeam has periodically arranged air holes along in the longitudinal direction. The existence of the air holes creates a photonic bandgap. The high index of silicon allows for optical confinement in the normal (width) direction by total internal reflection (TIR). Therefore, by removing the central hole or increasing the distance between the central two holes, the nanobeam can provide a strong light confinement in the central defect. In our case,

the distance of the two central holes is increased from 0.5 μm to 1.75 μm to form a defect, and on each side of the defect, a 7-period photonic barrier is utilized to minimize the TE-like modes from leaking out of the center. The diameter of the holes in the nanobeam is chosen to be 400 nm and the periodicity of air holes is set to be 500 nm.

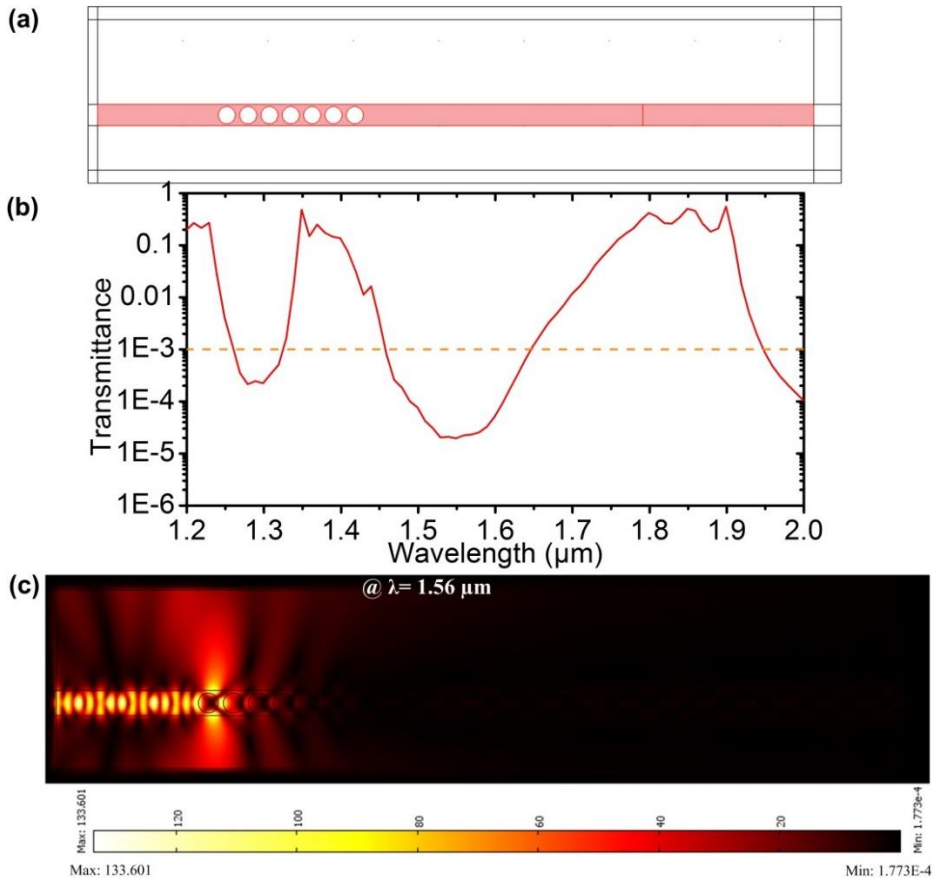

Figure 4.4 (a) Schematic of nanobeam for simulation using COMSOL (b) Transmittance of nanobeam with respect to wavelength (c) Mode profile of light propagating through the nanobeam with wavelength of 1.56 μm.

Commercial FEM software COMSOL Multiphysics was used to perform optical simulations (Fig. 4.4a). Here photonic bandgap is defined as a range of wavelength in which optical transmittance is below 0.001. The 7-period half nanobeam (each side of the cavity) has multiple photonic bandgaps centered at 1.29 μm, 1.54 μm, etc. The bandgap centered at 1.54 μm spans from 1.45 μm to 1.63 μm, which covers the communication wavelength range.

Therefore, light near 1.55 μm can be confined in the central part of the nanobeam without significant loss.

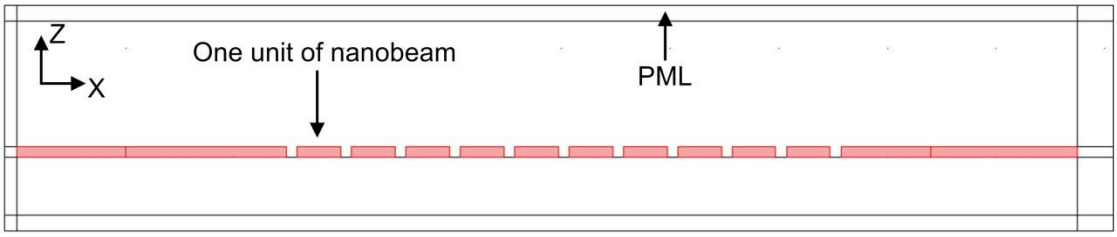

Figure 4.5 2D schematic of reconfigurable PC for simulation in COMSOL.

In the vertical plane (XOZ plane) we set up a 2D model for the reconfigurable PC structure, as shown in Fig. 4.5. Each nanobeam is modeled as a small unit with a thickness of 200 nm and a width of 750 nm. The reconfigurable PC structure has multiple photonic bandgap in X direction where the dielectric constant is periodic. Since we are able to modulate effective refractive index of each nanobeam unit in X direction by applying voltages, it is possible to reconfigure the photonic bandgap along X direction.

To theoretically demonstrate the reconfigurability of the device, we begin with a simple case where two adjacent units (nanobeam-based cavities) are grouped. The second unit in the group is vertically shifted by a distance of **s**, as show in Fig. 4.6a. The grouped two units along X direction form one period of the reconfigured new PC. By changing the relative position of the second unit to the other unit in one period, both the photonic lattice and photonic bandgap will be changed.

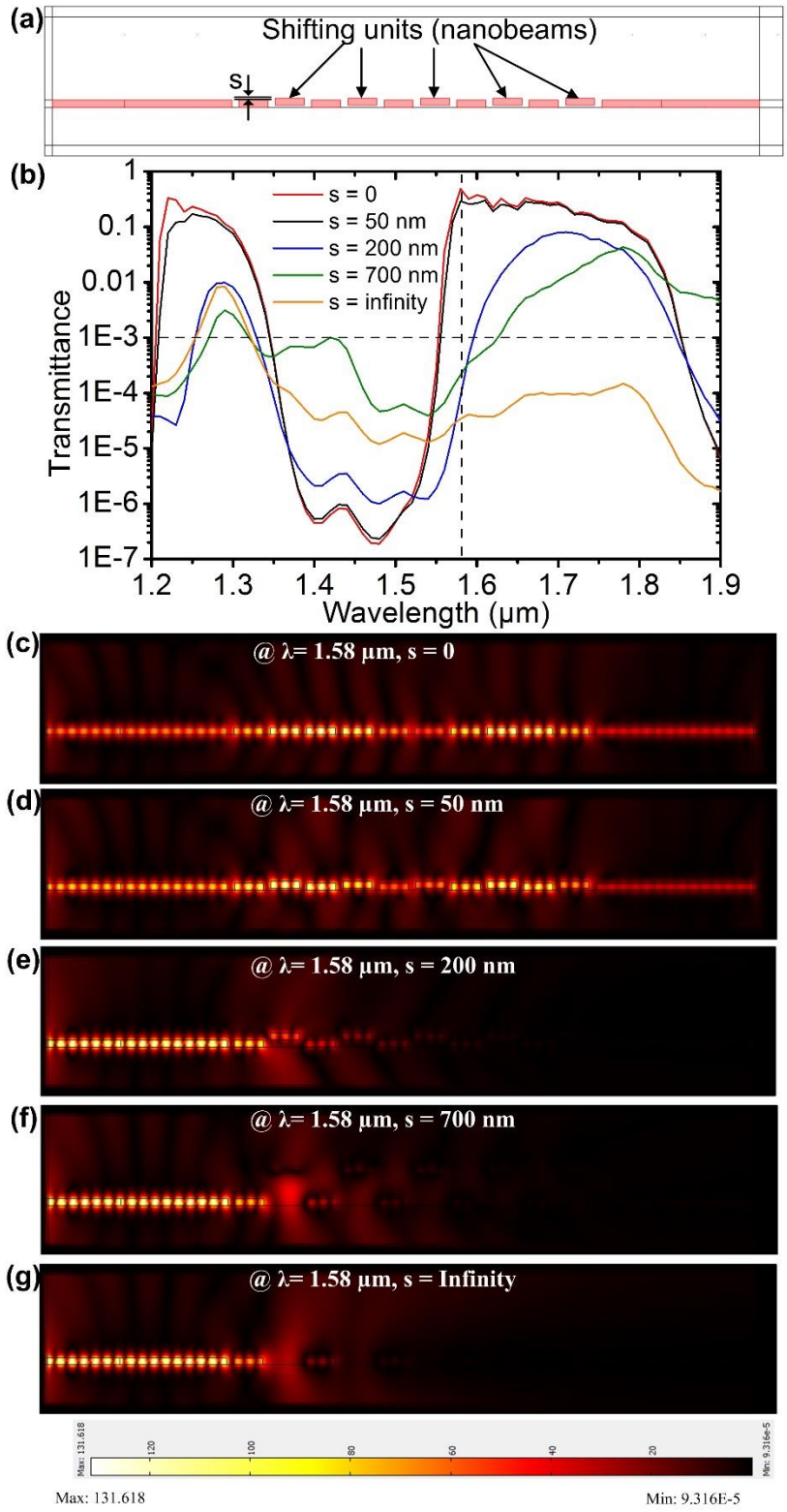

Figure 4.6 (a) Schematic of the reconfigurable PC in COMSOL. Two units are grouped to form a new photonic unit in the new PC. The second unit vertically shifts with a distance of **s**. (b) Transmittance of the reconfigured PC at **s** = 0, 50, 200, 700 nm, and infinity. (c)-(g) Mode profiles of the reconfigured PC at the wavelength of 1.58 μm, for different shifts from **s** = 0 to infinity.

Figure 4.6b shows the transmittance of the reconfigured PC with **s** varied from 0 to infinity. Similarly, the photonic bandgap is defined as a range of wavelength in which transmittance is below 0.001. The photonic bandgap at s = 0 is around the communication wavelength of 1.55 μm, spanning from 1.345 to 1.552 μm. When **s** increases to 50 nm, the bandgap becomes wider, spanning from 1.337 to 1.558 μm. With increasing **s**, the effective refractive index of the grouped photonic unit decreases, thus increasing the bandgap. When **s** = 200 and 700 m, the bandgap covers a wavelength range from 1.329 to 1.596 μm, and from1.319 to 1.626 μm, respectively. As **s** is set to be infinity, the bandgap starts from 1.32 μm to more than 1.9 μm with a low transmittance. The reason for this is that the absence of the second unit makes the actual lateral gap between two units to be 1.25 μm and this wide gap makes the new waveguide very lossy due to the significant scattering effect in the vertical direction.

To demonstrate how the tunable photonic bandgap influences light propagation through this PC structure, we simulated the TE-like mode profiles at the wavelength of 1.58 μm. Also, the photonic bandgap As shown in Figs. 4.6 c-g, at **s** = 0 the PC structure is able to guide the light at 1.58 μm with a transmittance of more than 0.3. But, when **s** reaches more than 200 nm above the original plane, the transmittance dramatically drops down to less than 0.0002. The result shows that by adjusting **s** to be larger than 200 nm, light at 1.58 μm can be blocked by the structure.

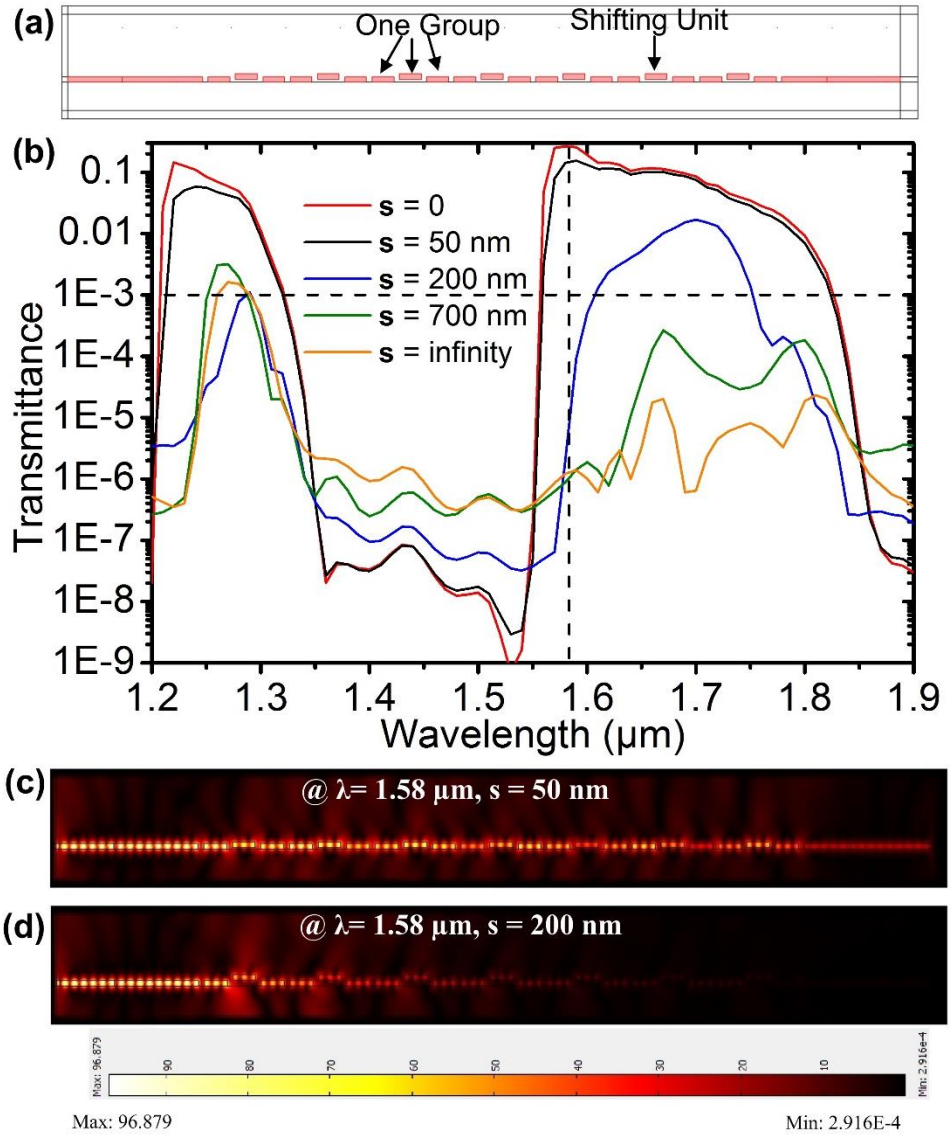

Figure 4.7 (a) Schematic of the reconfigurable PC in COMSOL. Three units are grouped to form a new photonic unit in the new PC. The second unit vertically shifts with a distance of **s**. (b) Transmittance of the structure at **s** = 0, 50, 200, 700 nm, and infinity. (c)-(d) Mode profiles of the structure with the wavelength of 1.58 μm at **s** = 50 nm (c) and 200 nm (d).

Next, we group three adjacent nanobeam units together as a new combined photonic unit. First, we investigate the effect of tuning one nanobeam unit in the combined group on photonic bandgap. Fig. 4.7a shows an example where the second unit moves upward. At **s** = 0 and 50 nm, the bandgaps are almost the same as those in the previous case of the two-unit group. When **s** increases to 200 nm, the bandgap spans from 1.281 μm to 1.607 μm, which is

about 22 % wider than that in the two-unit group case. But, the conduction band on the left side of the bandgap disappears (i.e., transmittance < 0.001), and thus the shorter wavelengths are blocked. Therefore, the result suggests that we could make necessary tradeoff among tuning range of photonic bandgap and location of conduction band to achieve desired optical properties of the reconfigured PC. As an example in Fig. 4.8a, two units in the three-unit group are tuned together by simultaneously applying the same voltage. Very similar to the case of tuning one unit in the three-unit group (Fig. 4.7), the bandgap at **s** = 0 and 50 nm are almost the same as those in the two-unit group case and they become wider at **s** ≥ 200 nm.

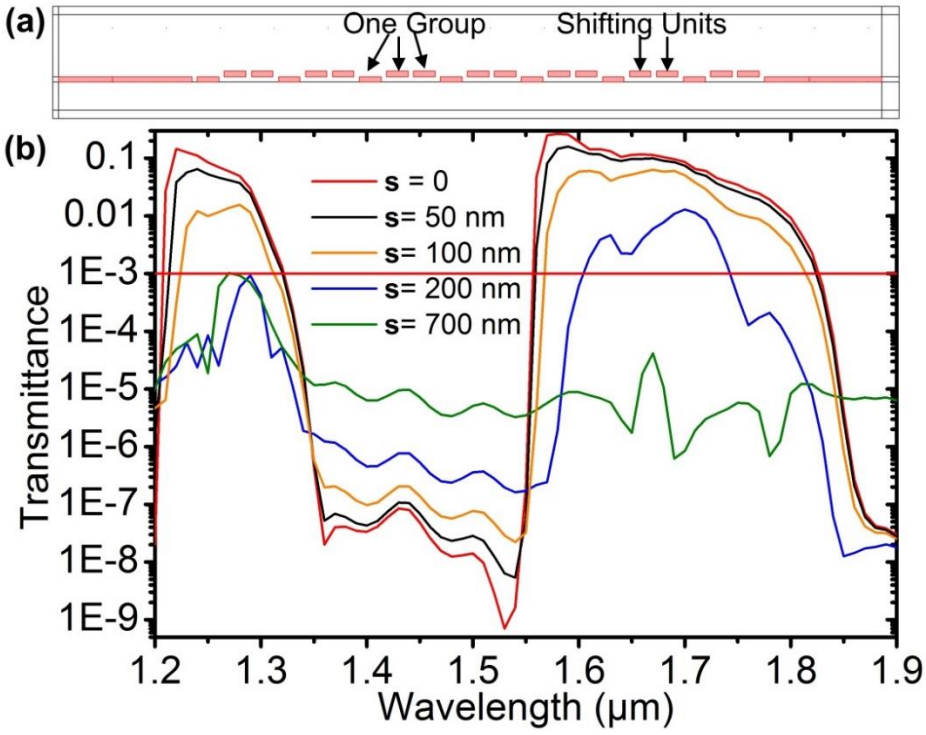

Figure 4.8 (a) Schematic of the reconfigurable PC in COMSOL. Three units are grouped to form a new photonic unit in the new PC. The second and third units shift with a distance of **s**. (b) Transmittance of the structure at **s** = 0, 50, 200, 700 nm, and infinity.

In the above simulations, we have demonstrated the capability of tuning the photonic bandgap of the device by actuating individual or subgroup of nanobeams inside a grouped or reconfigured lattice. To further demonstrate the flexibility in engineering photonic bandgap

of PC [6], we reconfigure on the original PC to form two new PC structures and combine them to obtain an even wider bandgap. A shown in Fig. 4.9a, two periodic PCs are formed, with a static PC on the left side and the other on the right side as a tunable PC. By connecting the two PCs in series, the new bandgap of the combined structure is able to block lights with wavelengths falling in the bandgaps of the two PC structures. As shown in Fig. 4.9b, the width of the combined photonic bandgap is significantly widened when s of the second PC increases to 200 nm.

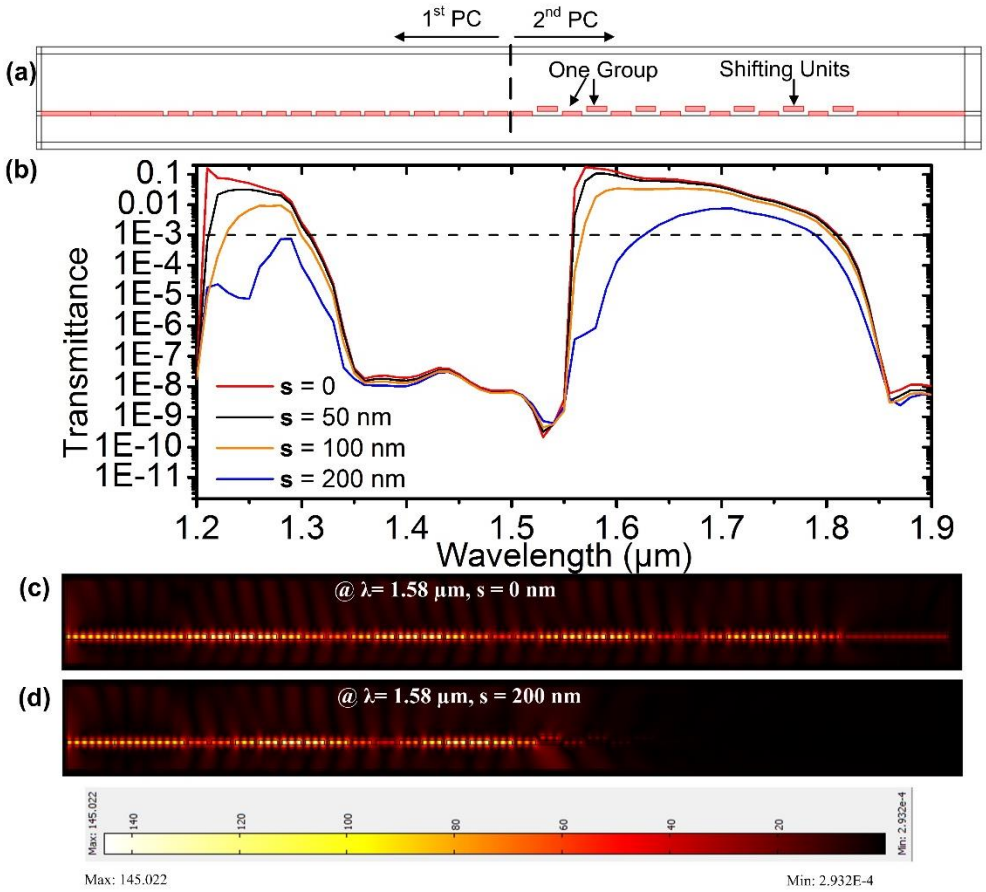

Figure 4.9 (a) Schematic of the reconfigurable PC in COMSOL. The structure consist of two PCs. The one on the left is static. The other on the right is a tunable PC where two nanobeam units form a periodic group with s being adjusted. (b) Transmittance of the structure at **s** = 0, 50, 100, and 200 nm. (c)-(g) Mode profilesx of the structure at the wavelength of 1.58 μm at **s** = 0 and 200 nm.

4.5 Device Fabrication

In the Chapter 2, we have discussed the fabrication techniques for manufacturing various types of suspended PC structures on SOI wafers. The developed processes allowed us to make the proposed reconfigurable nanobeam-based PC. Figures 4.10a-b show SEM images for the patterns of the reconfigurable PC in PMMA resist after e-beam lithography. We used RIE to etch unwanted silicon by using the patterned PMMA layer as an etching protection mask. The patterns were then transfer into the top silicon layer of the SOI wafer. After that, the PMMA layer was stripped off by PMMA remover. After removal of PMMA, wet etching is conducted to remove the buried oxide underneath the air hole areas of the nanobeams, making the nanobeams free-standing. Figures 4.10c-d show the reconfigurable PC device.

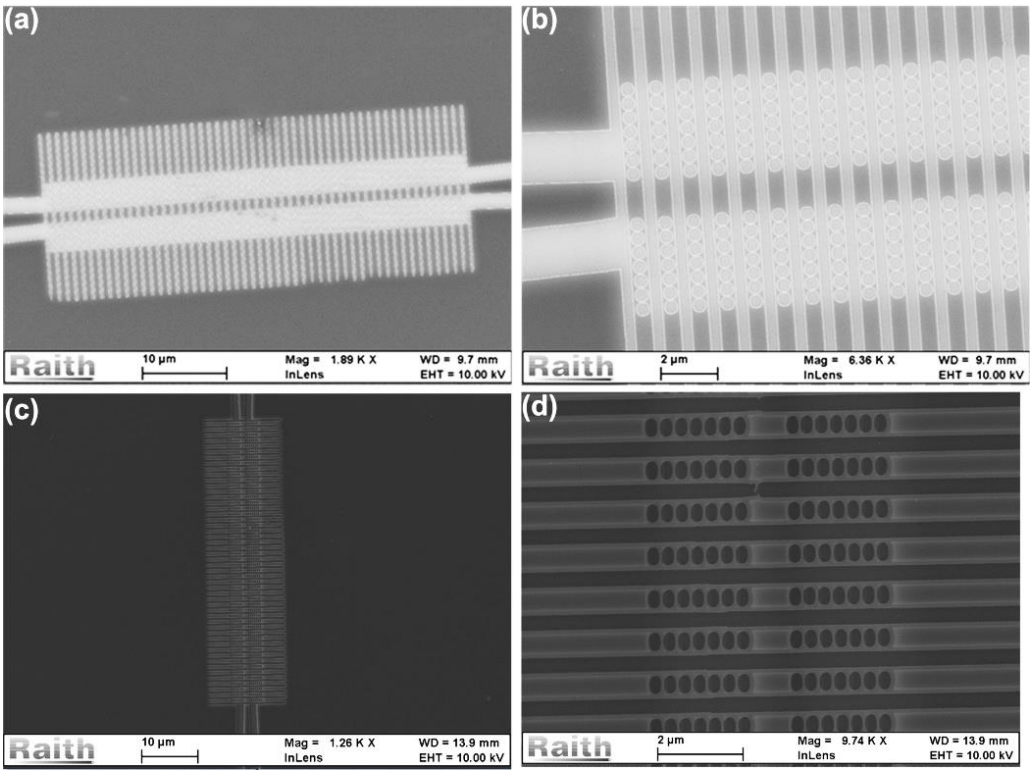

Figure 4.10 (a) Overview and (b) close-up of the reconfigurable PC structure after e-beam lithography; (c) overview and (d) close-up of the reconfigurable structure after etching on a 45-degree tilting stage.

The fabrication of gold nanoelectrodes on a glass slide is slightly different from that on a silicon wafer. As we mentioned in Chapter 2, we need to add a layer of conductive polymer (PEDOT:PSS) on the top surface of PMMA to make it more conducting for e-beam lithography. After the lithography, we deposited a gold layer with the thickness of 20 nm, followed by stripping off the unwanted gold via lift-off process. Figure 4.11 shows SEM images of glass slide with gold nanoelectrodes after the lift-off process.

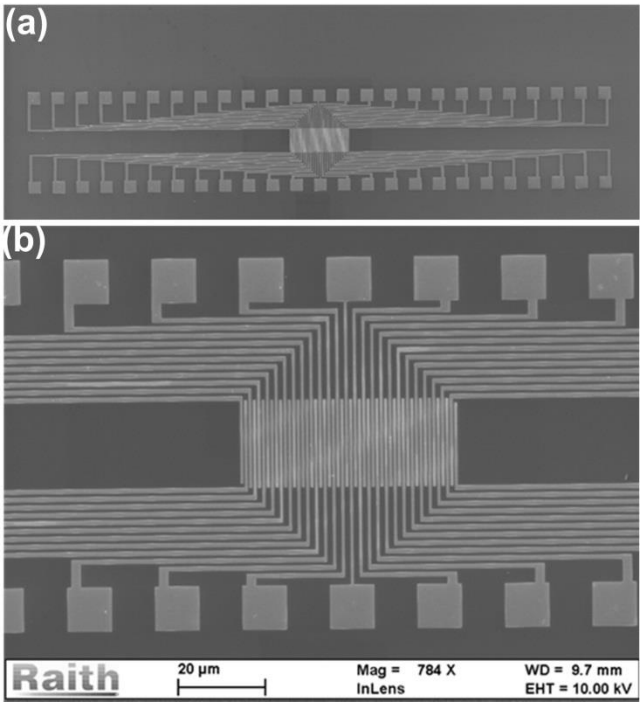

Figure 4.11 (a) Overview and (b) close-up of glass slide with gold electrodes.

4.6 Experimental Demonstration of Device Reconfigurability

In Section 4.4, we theoretically investigated the reconfigurablility of the proposed photonic structure to achieve different functionalities. To experimentally demonstrate the reconfigurablility, we designed a testing setup, as shown in Fig. 4.12. The gold nanoelectrodes were carefully aligned with the PC under a microscope. A 1 µm thick photoresist pattern was used to create an air gap between the gold nanoelectrodes and the PC.

The input and optical fibers were placed above and aligned with the corresponding grating couplers. The nanoelectordes were connected to a multichannel voltage controller.

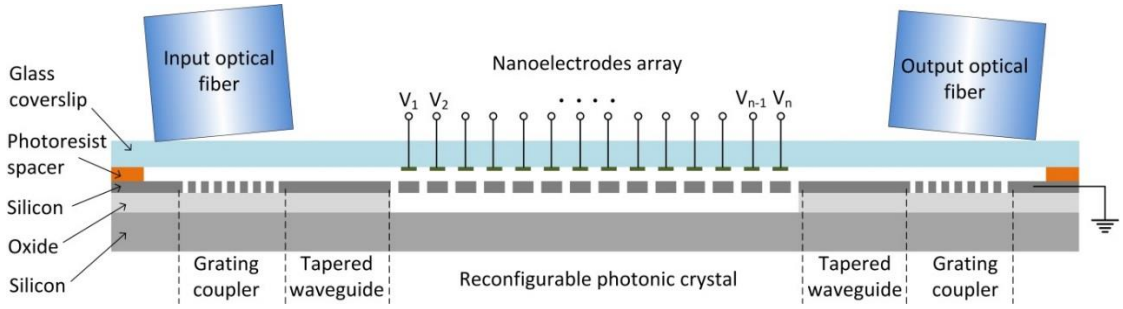

Figure 4.12 Schematic of a testing setup for reconfigurable PC device.

The first demonstration (theoretical demonstration given in Fig. 4.6a in Section 4) takes two neighboring nanobeam units as a group and tunes the vertical position of one nanobeam in the group. To implement it in the experiment, we connect all the corresponding nanoelectrodes together and record the spectra at different applied voltages. As the applied voltage V increases from 20 to 50 Volt, significant red shift in the right edge of the bandgap was observed, demonstrating the effectiveness of bandgap engineering (Fig. 4.13). However, the experimental spectra have obvious blue shift with respect to their theoretic transmittance. This is presumably due to possible fabrication errors and misalignment between the nanoelectrodes and the PC. For example, the obtained width of nanobeams is slightly narrower than the designed one, resulting in a blue shift in bandgap.

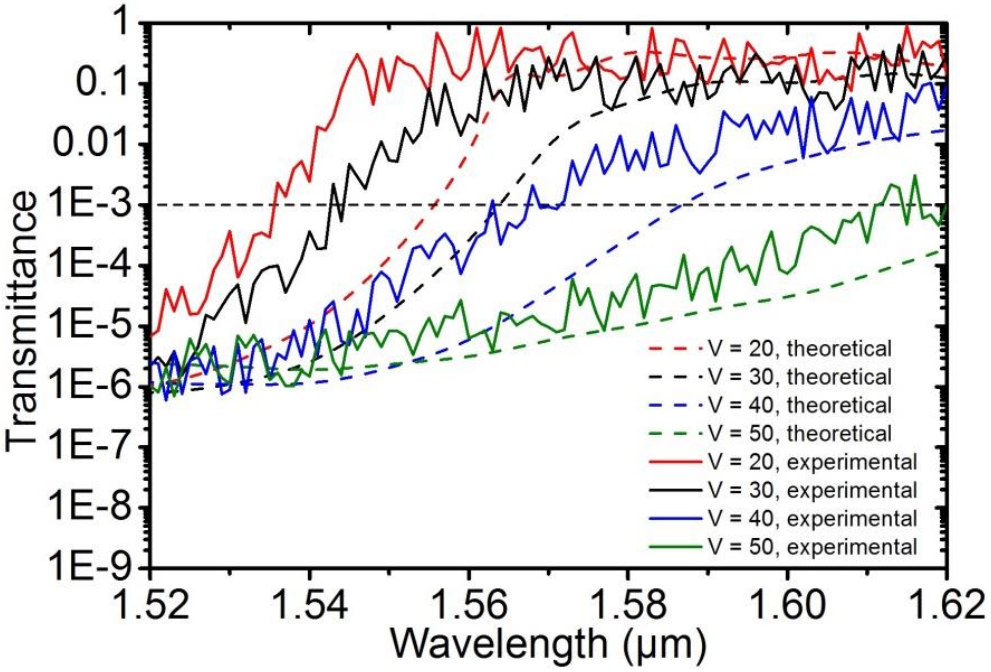

Figure 4.13 Theoretical and experimental transmittance as a function of wavelength. This result demonstrates the tuning example described in Fig. 4.6a at V = 20, 30, 40 and 50 Volt.

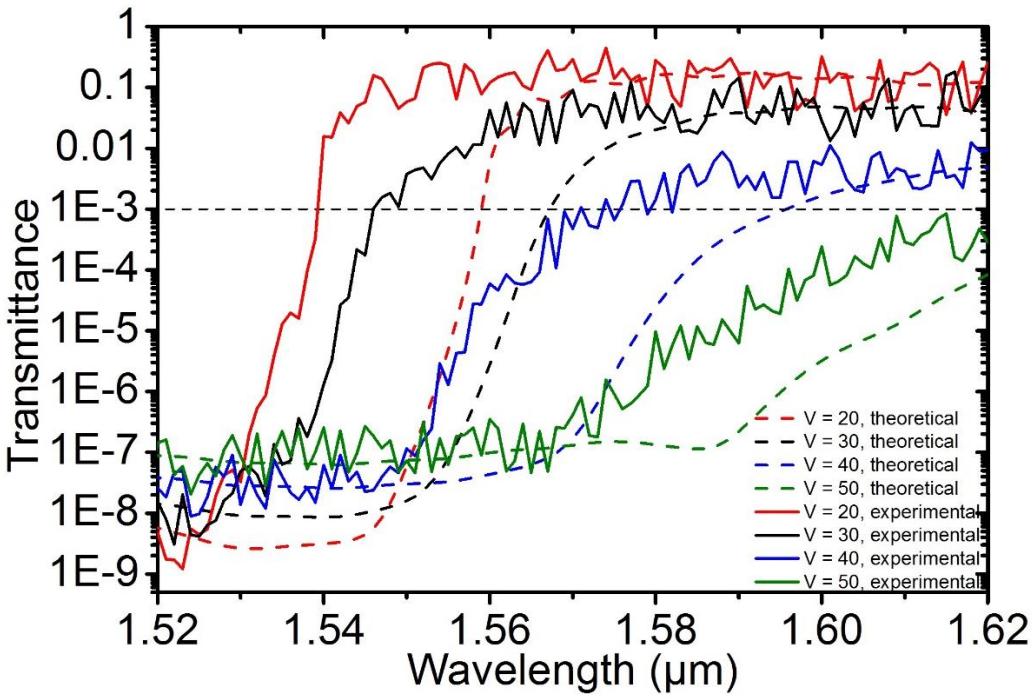

Figure 4.14 Theoretical and experimental transmittance as a function of wavelength. This result demonstrates the tuning example described in Fig. 4.7a at V = 20, 30, 40 and 50 Volt.

The second tuning example was theoretically described and demonstrated in Fig. 4.7a, where three neighboring unit nanobeams are grouped as a new combined unit and one nanobeam in the grouped unit changes its vertical position. Figure 4.14 shows the experimental results. Compared to the theoretical result, the right edge of the bandgap shifts to a longer wavelength. Similarly, this is maybe due to the fabrication and alignment errors. Nevertheless, as the voltage increases, the wavelength of conduction band redshifts and corresponding transmittance decreases.

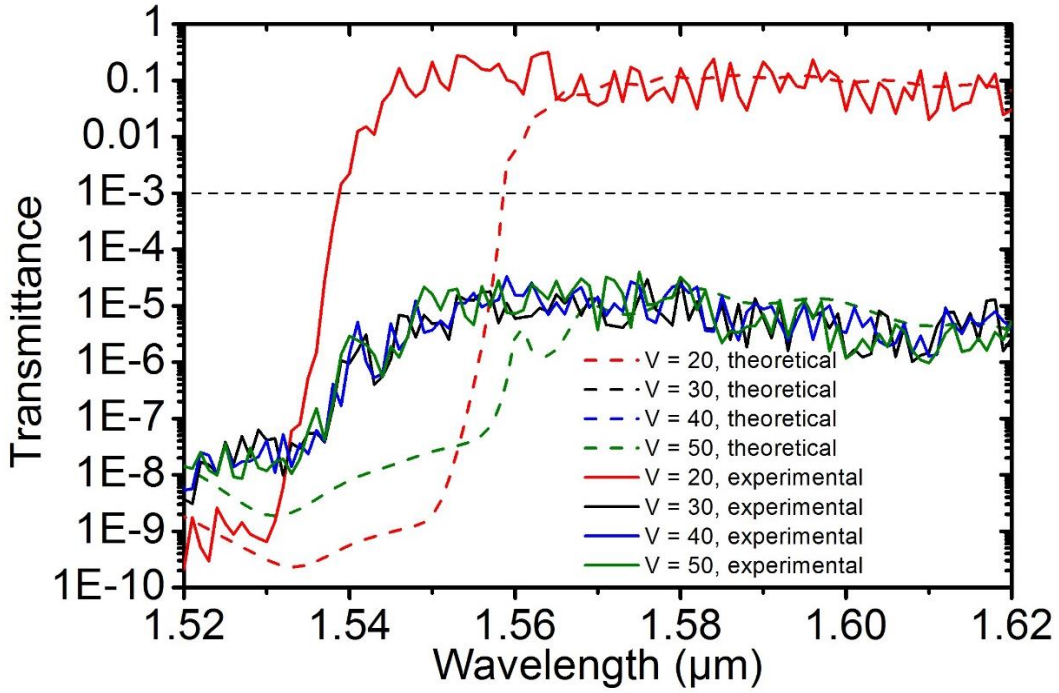

Fig. 4.15 Theoretical and experimental transmittance as a function of wavelength. This result demonstrates the tuning example described in Fig. 4.9a at V = 20, 30, 40 and 50 Volt.

The third tuning example is theoretically described in Fig. 4.9a, forming a static PC and a tunable PC structures on the original single PC. By tuning one nanobeam unit in a group of two neighboring units for the tunable PC structure, the bandgap becomes wider as expected, as shown in Fig. 4.15. However, after the applied voltage reaches 30 Volt, the

transmittance in a wide range of wavelength is shown very low, presumably due to the optical loss.

4.7 Theoretical Study of Cantilever-Pillar Reconfigurable Photonic Crystal

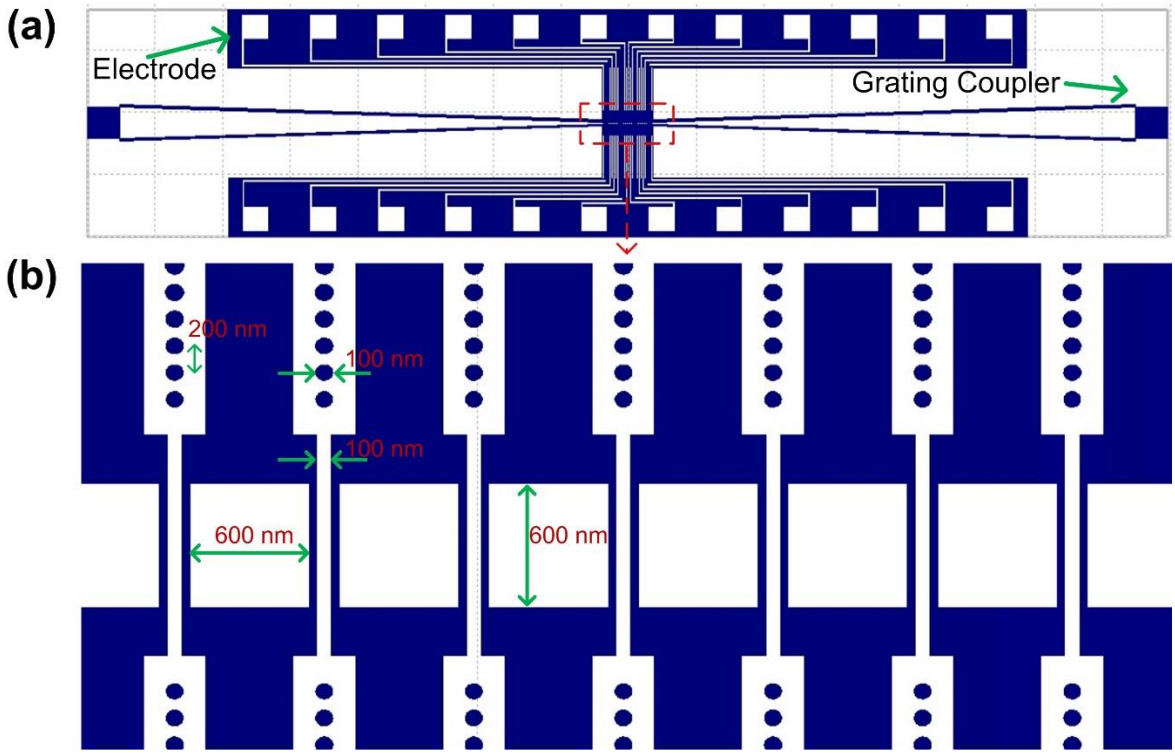

Figure 4.16. (a) Overview and (b) close-up of cantilever-pillar reconfigurable PC structure with anchored stack.

In this section, we propose another reconfigurable PC design integrating an array of mechanical tunable silicon nanobeams with an array of fixed silicon pillars (Fig. 4.16). The pillars are designed as a straight PC structure as a base waveguide. The air gaps between every two neighboring pillars are inserted by silicon cantilevers. These cantilevers are the narrow central parts of the nanobeams in the vertical direction. The cantilevers and the pillars are alternating in positions. The cantilever-pillar reconfigurable PC is connected with a tapered

feeding and an output waveguides in the horizontal direction. The width of the cantilever insertion is 100 nm. The side length of the pillar is 600 nm.

Different from the previous design in Fig. 4.2, this new reconfigurable PC is integrated at a higher level, where each silicon nanobeam serves as an individual nanoelectrode and the handling layer of the SOI wafer serves as a common electrical ground. As the top silicon layer is highly doped ($10^{21}/cm^3$) and each nanobeam has its own contact pad, these nanobeams can be applied with voltages for individual actuation and control of local effective index of each photonic unit. Due to limited time and scope of this research, only theoretical study has been conducted in this thesis.

We investigate bandgap characteristics of the proposed PC as the nanobeam units bend out of plane (bending inside is identical with bending inside). Here, the photonic bandgap of the PC is defined as a range of wavelength in which transmittance is below 0.001. Figure 4.17b shows the transmittance of the reconfigured PC with **s** is varied from 0 to 100 nm. At **s** = 0, there is one photonic bandgap spanning from 1.094 to 1.120 μm. When **s** increases to 50 nm, another bandgap occurs in a wavelength range from 1.007 to 1.041 μm. As **s** further increases to 100 nm, both the two bandgaps become wider with red shift, spanning from less than 1.000 to 1.064 μm, and from 1.186 to 1.268 μm. TE-like mode profiles at the wavelength of 1.10 μm with different **s** is shown in Fig. 4.17c-e. At **s** = 0 and 50 nm the PC structure is not able to guide the light at 1.10 μm with a transmittance of more than 0.001. But when **s** reaches 100 nm, the transmittance dramatically increase to 0.01 and light at 1.10 μm can propagate through the device due to the bandgap shift.

Notably, as we further increase **s** from 100 nm to 150, to 200 nm, up to infinity, the third photonic bandgap is generated, as shown in Fig. 4.18a. Also the width of bandgap gets

wider and the center of bandgap red shifts further. TE-like mode profiles at the wavelength of 1.30 μm with different **s** are shown in Figs. 4.17c-e. We can clearly see light at 1.30 μm can propagate through the device at **s** = 100 nm. When **s** increases more than 100 nm, the wavelength of 1.30 μm falls into the widen bandgap and thus the light is blocked by the structure.

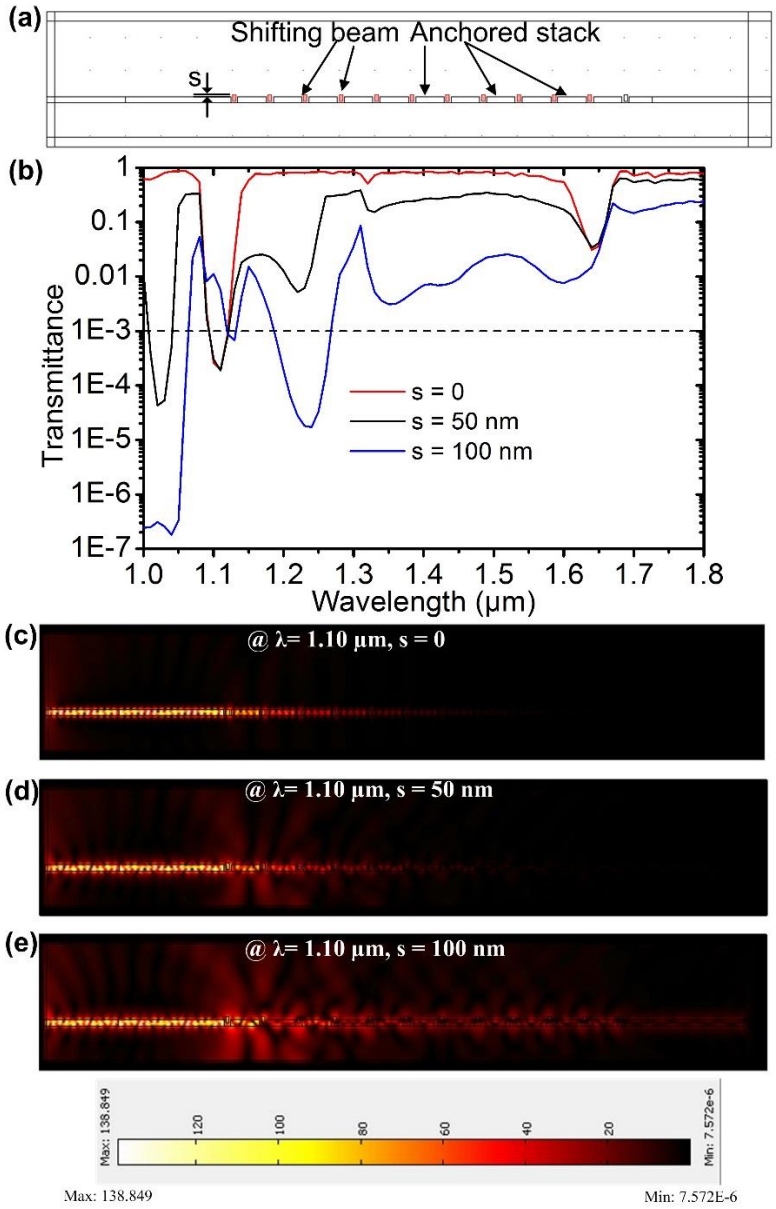

Figure 4.17 (a) Schematic of the cantilever-pillar reconfigurable PC in COMSOL. Nanobeam units vertically shifts with a distance of **s**. (b) Transmittance of the reconfigured PC at **s** = 0, 50, 100 nm. (c)-(e) Mode profiles of the reconfigured PC at the wavelength of 1.10 μm, for different shifts from **s** = 0 to 100 nm.

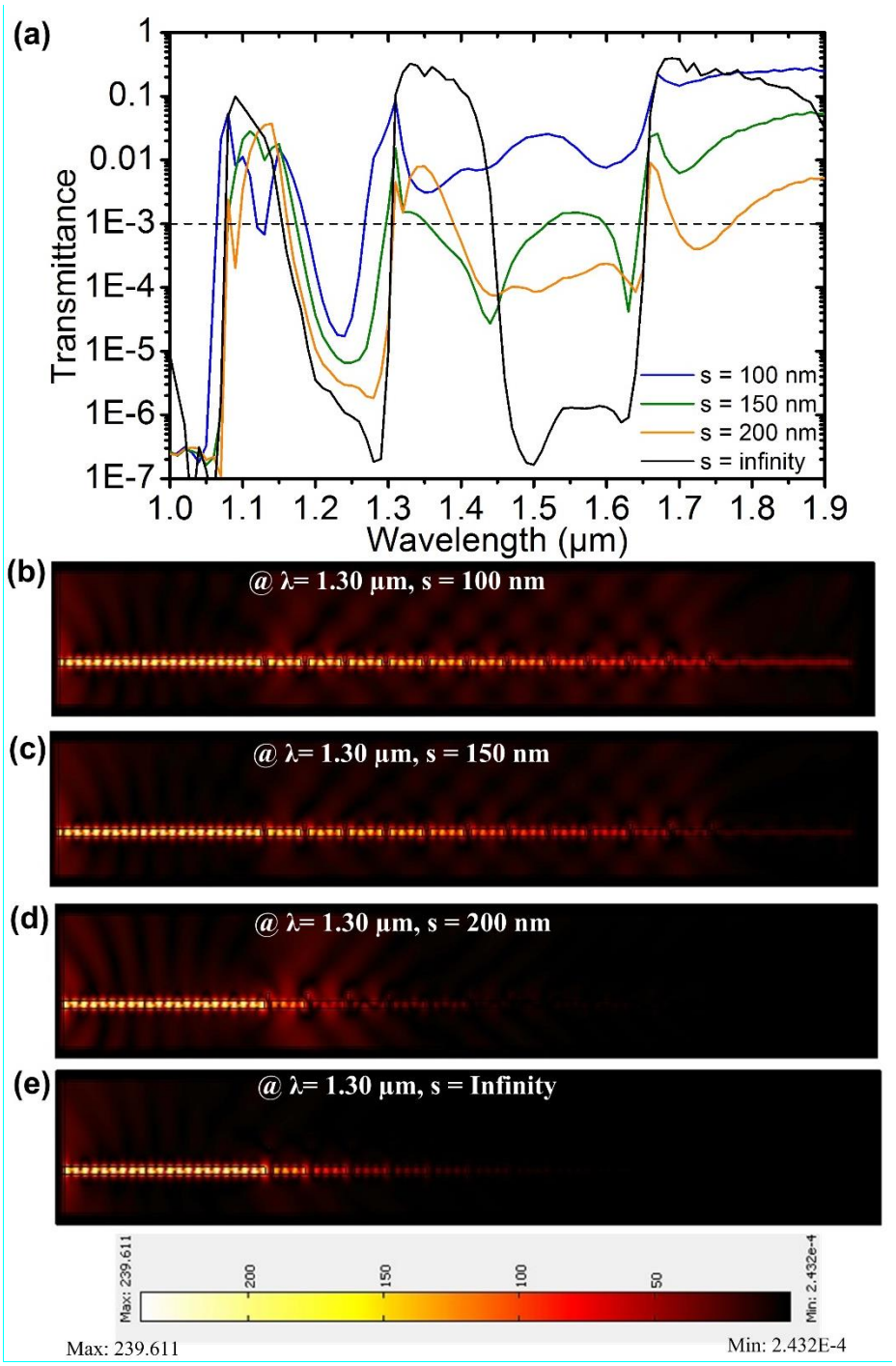

Figure 4.18 (a) Transmittance of the cantilever-pillar reconfigured PC at **s** = 100, 150, 200 nm, and infinity. (b)-(e) Mode profiles of the reconfigured PC at the wavelength of 1.30 μm, for different shifts from **s** = 100 nm to infinity.

4.8 Conclusion

In this chapter, we developed a novel reconfigurable PC consisting of an array of nanobeams. Both theoretical and experimental studies were conducted. The device is unique in that each nanobeam serves be an electrostatically tunable photonic element in the PC. We demonstrated the capability of the device to tune its photonic bandgap by presenting three different configurations, including tuning one unit in group of two nanobeams, tuning one or two unit in group of three, and forming two reconfigurable PCs together. Besides, we also theoretically studied another reconfigurable PC integrating an array of mechanical tunable nanobeams with an array of fixed pillars into the top silicon layer of a SOI wafer. This allows for a higher-level integration. Theoretical analysis for bandgap engineering was conducted.

References

[1] N. Tabiryan, U. Hrozhyk, and S. Serak, "Nonlinear refraction in photoinduced isotropic state of liquid crystalline azobenzenes," *Phys. Rev. Lett.*, Vol. 93, pp. 113901, 2004.

[2] R. Chen, A. Yan, M. Li, T. Chen, Q. Wang, J. Canning, K. Cook, and K. P. Chen, "Regenerated distributed Bragg reflector fiber lasers for high-temperature operation," *Opt. Lett.*, Vol. 38, pp. 2490−2492, 2013.

[3] J. A. Lott, R. P. Schneider, Jr., K. J. Malloy, S. P. Kilcoyne, and K. D. Choquette, "Partial top dielectric stack distributed Bragg reflectors for red vertical cavity surface emitting laser arrays," *IEEE Photonics Technology Letters.*, Vol. 6, pp. 1397−1399, 1994.

[4] Q. Quan, P. B. Deotare, and M. Loncar, "Photonic crystal nanobeam cavity strongly coupled to the feeding waveguide," *Appl. Phys. Lett.*, Vol. 96, pp. 203102-1-3 (2010).

[5] http://www.comsol.com.

[6] A. Cusano, A. Iadicicco, D. Paladino, S. Campopiano and A. Cutolo, "Photonic band-gap engineering in UV fiber gratings by the arc discharge technique," *Opt. Express*, Vol. 16, pp. 15332−15342, 2008.

CHAPTER 5. TUNABLE PHOTONIC CRYSTAL-CANTILEVER CAVITY

5.1 Background

Optical resonant cavities [1] with high quality factor and small mode volume provide a powerful means of modifying interactions between light and matter, and have many exciting applications, including quantum information processing [2], nonlinear optics [3], optomechanics [4, 5], optical trapping [6], optofluidics [7], integrated photonic circuits [8], and sensor applications [9]. Different light confinement methods have been developed to realize resonant cavities with a high Q factor, such as Fabry-Perot cavity, whispering gallery resonator, microring resonator, and photonic crystal (PC). From a manufacturing and integration point of view, two dimensional (2D) PC has been considered as one of the most popular schemes because its fabrication process is compatible with the conventional standard silicon integrated circuit process.

However, the resonant frequency of an optical cavity is often difficult to exactly match the need of a given application because small fabrication induced variations and irregularities are inevitable. Tuning optical properties of an optical cavity is thus needed to increase their functionality and open up new possibilities for a variety of applications for integrated photonic circuits. Electro-optic tuning has been studied using lithium niobate [10-11]. But, only sub-nm tuning was achieved; Thermo-optic tuning has been demonstrated to tune resonant wavelength of a PC cavity up to tens of nm [12-13]. This method, however, is limited to materials with high thermo-optic coefficient and requires high temperatures (> 400 K). Phonon-assisted scheme can modulate full-width at half-maximum (FWHM) of a spectrum of the cavity by manipulating surface acoustic waves, but the central wavelength cannot be tuned [14]. Carrier injection method is commonly used in optical modulation in

silicon [15-16]. But, the voltage and power consumption of these silicon modulators are too high for on-chip applications. For the most widely employed p-i-n diode configuration, these issues for gigahertz modulation stem from a lower limit of ac current density (~104 A/cm^2) intrinsic to silicon.

Another way to modulate optical cavities is to utilize optomechanical force provided by photons circulating inside optical cavities [17-19]. This method needs a complex dual structure with a non-trivial gap distance design, to support even and odd modes required for obtaining optical force. Infiltration of liquid crystal into PC structure is a good scheme for electrical or thermal modulation for refractive index of material [20-21]. However, integration of fluids into solid-state devices may bring additional issues. Mechanical tuning has been demonstrated to tune optical characteristics of an optical cavity. By moving a dielectric plate towards a PC line-defect waveguide [22] or changing a height difference between a PC waveguide and silicon rods [23], optical transmittance of PC waveguides can be tuned. In another example, physical perturbation of an AFM tip or a small plug into the periodic holes of a PC has allowed modulating transmission of light through the PC [24-25]. Overall, the mechanically tunable optical devices often require sophisticated fabrication processes, multi-layer structures, and relatively complex actuation methods.

In this chapter, we present a novel tunable PC resonant cavity. A mechanical cantilever serves as a tunable defect in a 2D PC slab. We call it PC-Cantilever Cavity or PC^3. Our previous theoretical study has shown that nano-photo-mechanical interactions between a gold/silicon nitride (Au/Si_3N_4) nanocantilever and the defect-mode field inside the PC^3 are strong and highly sensitive to a surface stress-induced mechanical deflection of the cantilever [26]. However, a silicon PC with an embedded Au/Si_3N_4 cantilever is not easy to fabricate.

To experimentally demonstrate the PC^3 concept, we designed a simple device structure, in conjunction with an electrostatic actuation method, to realize a MEMS tunable PC^3 device. A PC and a cantilever are integrated in the same top silicon layer of an SOI wafer. The whole top silicon layer serves as an electrode while the handling layer of the SOI wafer acts as an electrical ground of the device. This allows forming the PC3 in a single planar layer using single-step e-beam lithography, reactive ion etching, and wet etching-based release for the cantilever.

In the following sections, we propose two schemes of SOI-based PC^3 designs and investigate their optical and electromechanical characteristics. Then, we present our results on fabrication and characterization of the PC^3 devices. Our discussion will be based on the result of electromechanical tuning of transmittance spectra of the devices.

5.2 Photonic Crystal-Cantilever Device Structures

Figure 5.1 shows the top-view schematics of the proposed two PC^3 structures. To allow for an easy comparison of optical characteristics between the two structures, we utilize the same size cantilevers. The length and width of the cantilever are set to be l = 2.7 μm and w = 150 nm, respectively. The two schemes are implemented on the same type of SOI wafer, in which the top silicon device layer is 200 nm thick serving as a device layer and the buried oxide is 1 μm thick serving as an insulation layer. Also, the 2D PC lattice provides a 2D photonic barrier in plane directions and has a conventional triangular lattice structure with a periodicity of P = 500 nm and a hole size of D = 400 nm.

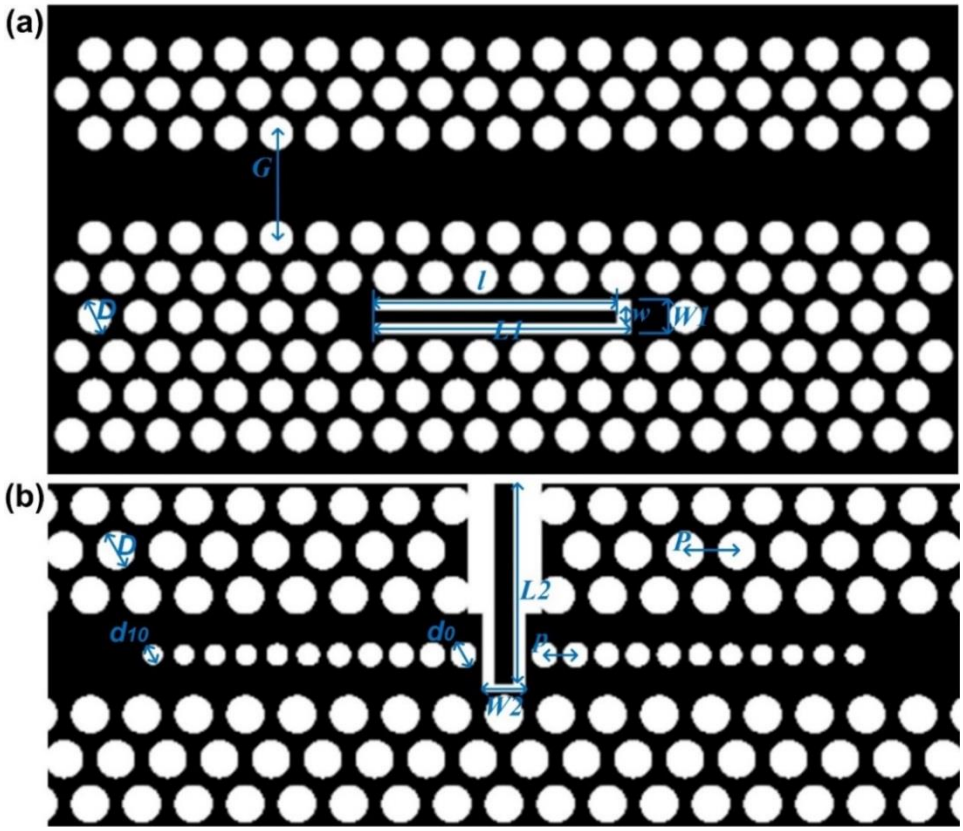

Figure 5.1 (a) Schematic of a PC^3 with a cantilever parallel to a PC waveguide; (b) Schematic of a PC^3 with the tip of a cantilever inserted into a nanobeam-based PC structure.

The first PC^3 device (Fig. 5.1a) is a modified version of a conventional 2D L6 PC cavity beside a feeding waveguide [27-29]. The feeding waveguide is formed by removing a line of air holes from the triangle-lattice PC and increasing the distance between two adjacent lines of holes to a gap G = 780 nm. The L6 PC cavity is formed 3 lattices away from the feeding waveguide by removing a line of six holes from the PC slab. The width and length of the cavity are set to be W_1 = 400 nm and L_1 = 2.9 μm, respectively. A cantilever is located in the cavity and anchored at one end. By removing the buried oxide from underneath the PC layer, the cantilever will be able to bend up and down under an electrostatic field created between the PC and the handling layer of the SOI wafer.

The second PC^3 design is a modified version of a conventional nanobeam cavity design [30-34], as shown in Fig. 5.1b. A linear array of air holes is designed on each side of the central defect. The periodicity of the linear air holes is fixed at p = 300 nm, while the radii of the air holes gradually decrease from the center outwards along the horizontal direction. The air hole nearest to the center has a maximum radius d_0 = 125 nm, while the air hole connecting to the feeding waveguide has a minimum radius d_{10} = 88 nm. The width of the nanobeam is adjusted to make the two adjacent lines of the PC holes in the center has the same gap G = 780 nm as that in the first scheme. To form a tunable cavity on the optical passage of the nanobeam, we removed 4 air holes from the PC lattice and inserted a tip of a sword-like cantilever into the space at the center of the broken nanobeam. The other end of the cantilever is anchored to the PC. The cantilever used here has the same size as that used in the first scheme. The width and length of the cavity are W_2 = 420 nm and L_2 = 2.8 μm, respectively.

5.3 Simulation for Electrostatic Actuation of Cantilever

Mechanical deflections of the embedded cantilever in the PC^3 under different applied voltages were simulated by using commercial finite element method (FEM) software COMSOL. For both the devices, the cantilevers are 200 nm thick, 200 nm wide, and 2.7 μm long (Figs. 5.1a and 5.1b). Since the buried oxide layer is removed, there is a 1 μm thick air layer between the cantilever and the handling Si layer. Thus, in the simulation, an electrical ground is placed 1 μm underneath the cantilever. The Si cantilever is heavily doped with boron ($10^{21}cm^{-3}$), the top surface of the cantilever serves as the other electrode of an electrostatic actuator. The Young’s modulus of silicon is 150 GPa and the Poisson's is 0.17.

The model uses the electro-mechanics interface to solve the coupled equations for the structural deformation and the electric field. The electrostatic fields in the air and in the cantilever are governed by the Poisson's equation.

As a voltage is applied to the top surface of the cantilever, the cantilever bends downward due to electrostatic attraction. Figures 5.2 a-c show the simulated bending profiles of the cantilever under three different applied voltages. As we will see later, the bending of the cantilever will cause to shift the resonance wavelength of the PC[3]. Figure 5.2d shows that the vertical deflection at the tip of the cantilever is not linear with, but approximately quadratic to applied voltage. At the applied voltage of 5, 15, and 50 volts, the corresponding deflection is about 0.4, 4.3 and 64.5 nm, respectively. When applied voltage reaches 97 volts, the deflection increases to 200 nm, making cantilever out of slab.

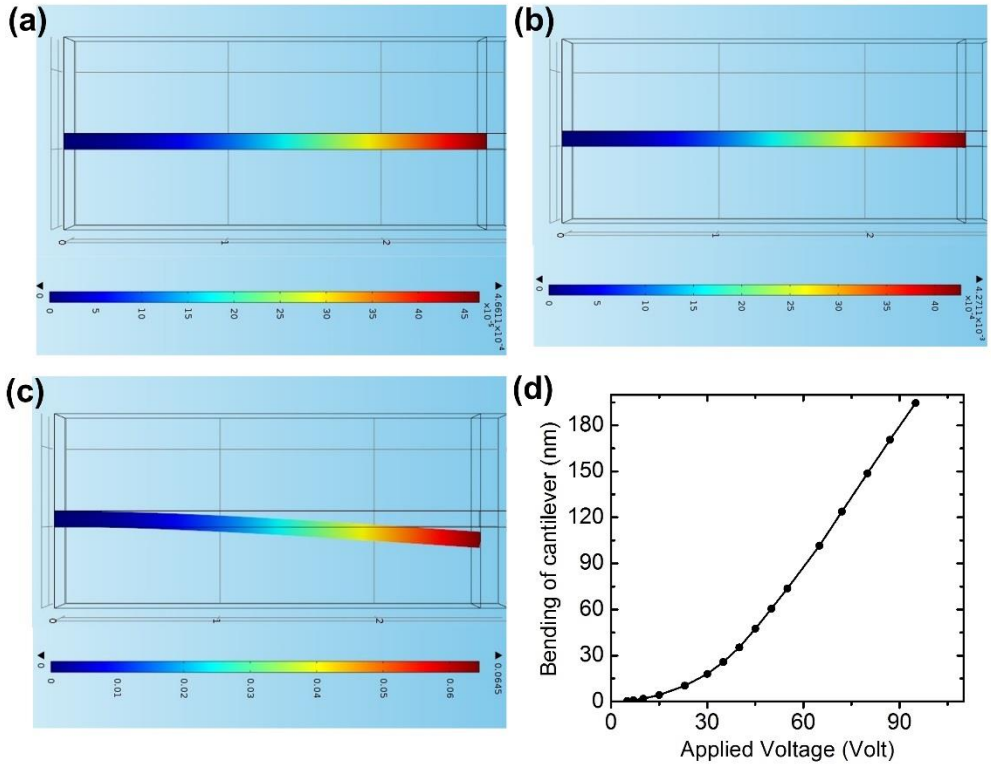

Figure 5.2 Simulated bending profiles of the cantilever under three different applied voltages: (a) 5 Volts (b) 15 Volts, and (c) 50 Volts. (d) Vertical displacement at the tip of the cantilever as a function of an applied voltage.

5.4 Theoretical Study on Photonic Crystal-Cantilever

To investigate the resonance characteristics of the two PC^3 structures, we use the plane-wave expansion method to conduct optical simulations. A TE-polarized pulse line source with a Gaussian frequency distribution is put along the vertical direction at center of the cantilever. This line source had the same height as the top Si layer. Resonance wavelength and Q factor of the PC^3 were computed by the Harminv [35] based on steady-state field profiles in time domain. To record the mode profiles, a continuous-wave line source at resonance was used.

Figure 5.3 shows the resonance mode profiles of the L6 PC^3 under different bending conditions of 0 nm (Fig. 5.3b), 100 nm (Fig. 5.3c), and 200 nm (Fig. 5.3d). Mode profiles in three planes cutting through center of the PC^3 are presented. Here, the mode profiles were taken after the propagation of 1000 wavelengths distance. The defect-mode field distributions demonstrated the capability of the PC^3 to confine the mode fields in all three dimensions. When the vertical displacement at the tip of the cantilever was $\Delta z = 0$ nm, 100 nm and 200 nm from the top surface of the slab, the resonance wavelength was 1557.5, 1551.4, and 1538.3 nm, respectively. The Q factor of the cavity was 1532.7, 1123.6 and 845.2, at $\Delta z = 0$ nm, 100 nm and 200 nm, respectively. The Q factor was relatively low and slightly degraded as the cantilever bent downward inside the hosting hole. The reason for the slight Q degradation is that the Q factor in the planar direction (X-Y plane) was determined mainly by the L6 geometry, while only slightly by the bending location of the cantilever inside the L6 cavity. Leakage of defect-mode field into removed SiO_2 layer was very limited. This allowed us to neglect the Si handling substrate in these simulations. When cantilever is bending

outside off the rectangular cavity, resonance wavelength blue shifts, due to the decreasing of effective index of the cavity.

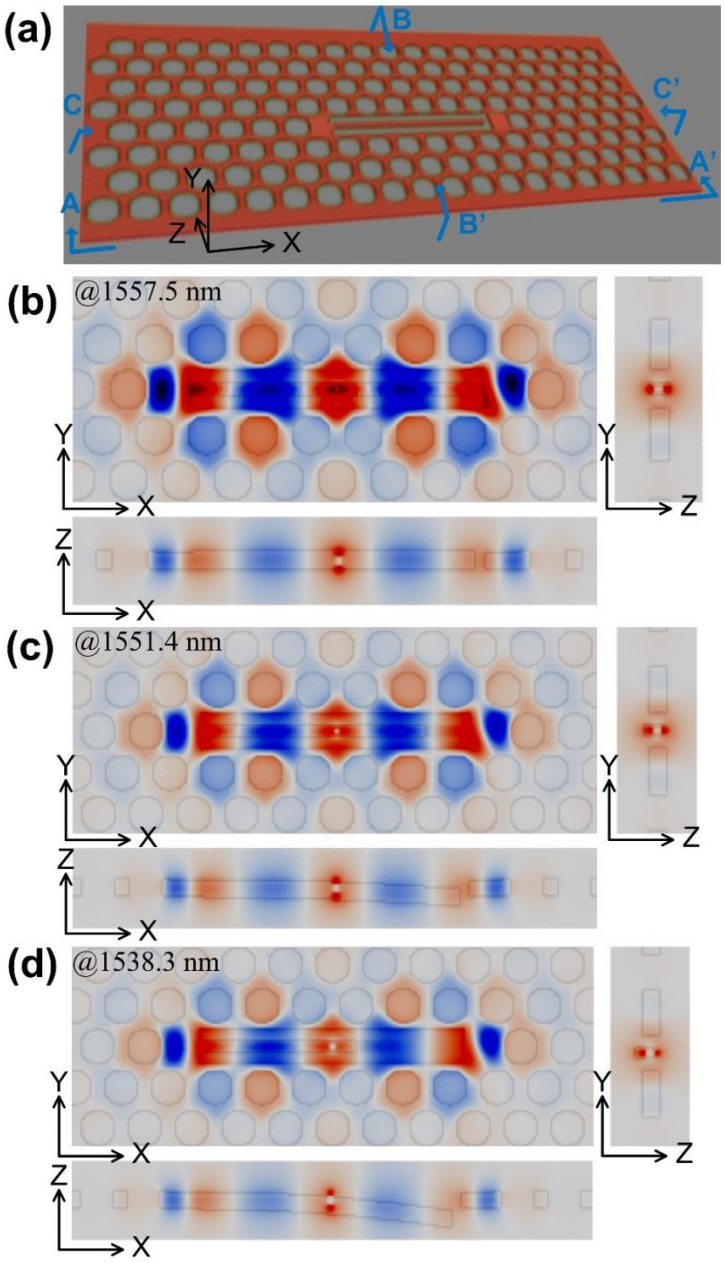

Figure 5.3 (a) 3D schematic of L6 PC^3; Electric field (amplitude) distributions at the resonance mode of L6 PC^3 with a deflection of 0 nm (b), 100 nm (c), and 200 nm (d). Each image contains three smaller images showing the field distributions in the plane of X-Y, Y-Z, and X-Z, at the cross section of A-A', B-B', and C-C', respectively (see (a)).

To understand how mechanical bending of the embedded cantilever influences transmission spectrum of the PC^3, we also performed 3D electromagnetic simulations using the finite-difference time-domain (FDTD) method with the freeware package MEEP [36]. The computing region covered a 200 nm thick Silicon layer sandwiched with two 300 nm thick air layers. 150 nm thick perfectly matched layers (PMLs) were applied at the boundaries of the entire computing region. 20 periods of the photonic lattice in the Γ-M direction were covered. The handling substrate of the SOI wafer was excluded because as we will see later, the mode profiles hardly reached the substrate through the removed oxide layer.

Figure 5.4 shows transmittance characteristics of the first scheme. Normalized transmittance is calculated as the ratio of the output optical powers with and without the L6 cavity. As shown in Fig. 5.4a, the normalized transmittance has a significant dip, which corresponds to the resonance mode coupling into the L6 cavity. Wavelength of transmittance dip is 1557.6, 1551.6 and 1538.4 nm when vertical displacement at tip of the cantilever is Δz = 0 nm, 100 nm and 200 nm. They are very close to resonance wavelengths of L6 PC^3 cavity at same displacements (1557.5, 1551.4, 1538.3 nm at Δz = 0, 100, 200 nm). Figure 5.4b shows the relation between shift of the transmittance dip wavelengths and bending of cantilever. The more the cantilever bends, the more the shift occurs. The transmittance dip wavelength shifts faster when cantilever bends outward since the change of effective refractive index gets larger. For the L6 PC^3 scheme, a theoretical maximum shift of 19.2 nm is obtained when the cantilever completely bends out of the slab (with a tip bending of 200 nm).

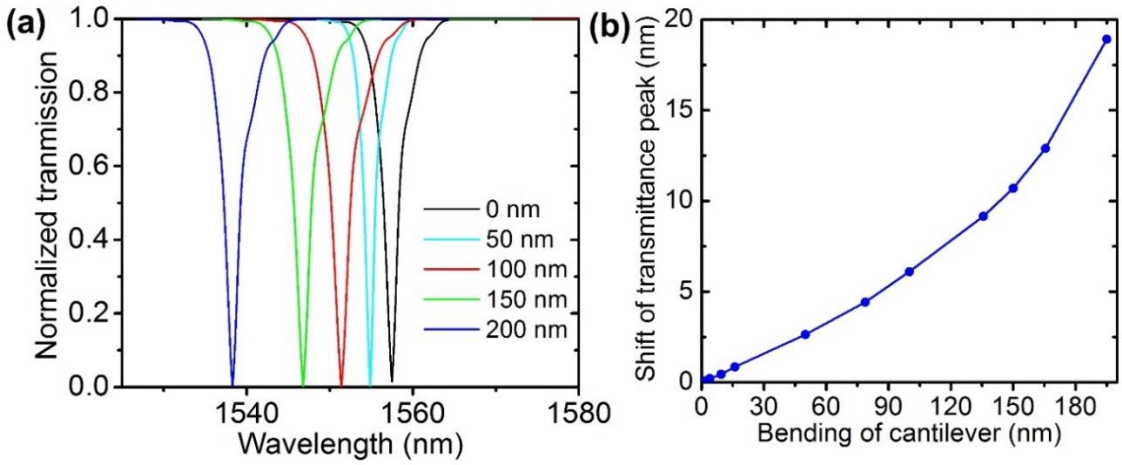

Figure 5.4. For L6 PC^3 device (a) Simulated normalized transmittance for different deflections at the tip of the cantilever: 0, 50, 100, 150, and 200 nm. (b) Resonance wavelength shift as a function of deflection at the tip of the cantilever.

Figure 5.5 shows the resonance mode profiles of the nanobeam-based PC^3 under different bending conditions: 0 nm (Fig. 5b), 100 nm (Fig. 5c), and 200 nm (Fig. 5d). The defect-mode field the PC^3 is mostly confined in the center of the nanobeam. The highest field strength occurs at the two sides of the tip of the vertical cantilever. The field profile indicates that the proposed nanobeam-based PC^3 has a similar field distribution to a conventional nanobeam cavity. The surrounding PC structure helps to confine the resonance mode in the planar direction. In the vertical direction, the energy loss at the resonance mode due to the presence of the cantilever is not found significant because the cantilever is designed so thin to support the transmission of light at the resonance mode along the cantilever. Therefore, as shown in Figure 5.5, the electric fields at the resonance mode are well confined in the cavity region in all three dimensions.

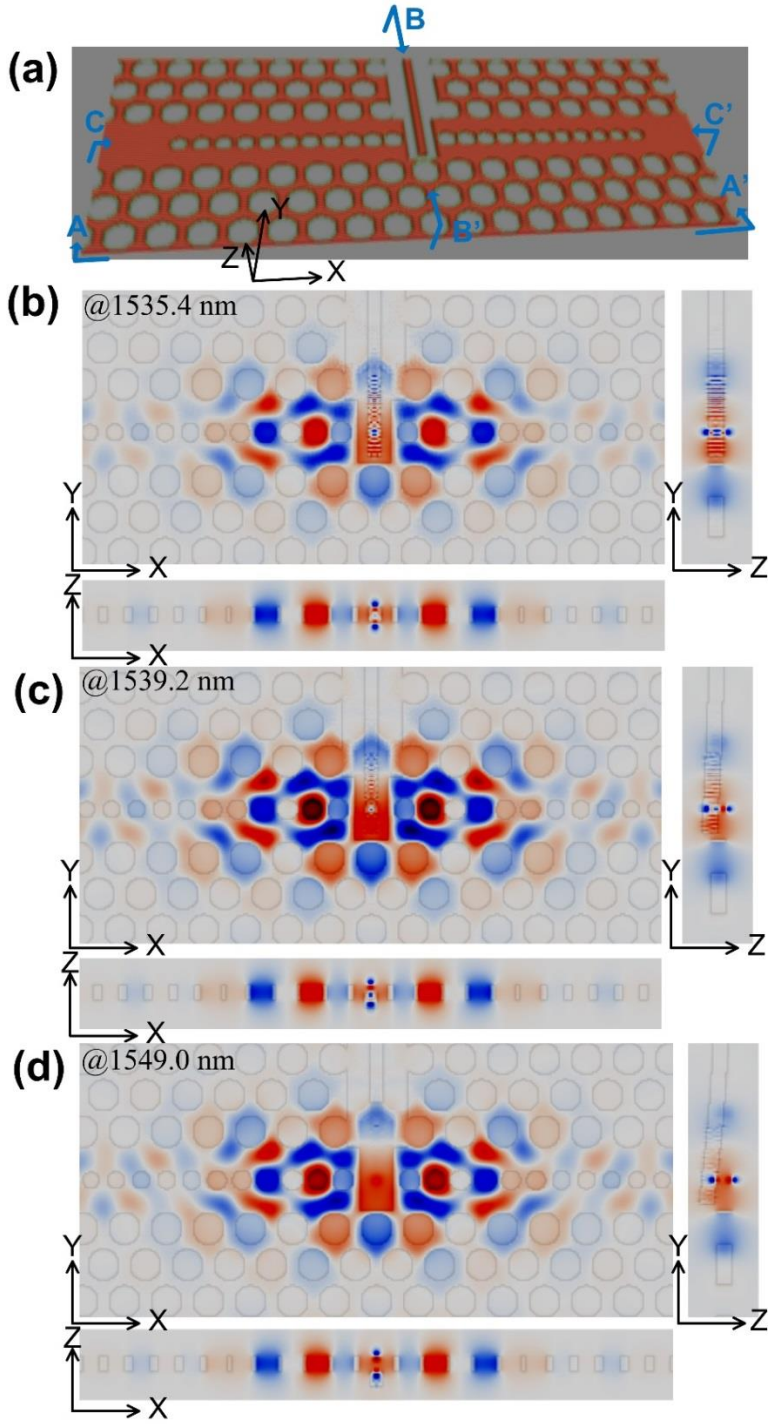

Figure 5.5 (a) 3D schematic of nanobeam-based PC^3; Electric field (amplitude) distributions at the resonance mode of nanobeam-based PC^3 with deflection of 0 nm (b), 100 nm (c), and 200 nm (d). Each image contains three smaller images showing the field distributions in the plane of X-Y, Y-Z, and X-Z, at the cross section of A-A', B-B', and C-C', respectively (see (a)).

Furthermore, when the vertical displacement at the tip of the cantilever was $\Delta z = 0$ nm, 100 nm and 200 nm from the top surface of the slab, the resonance wavelength was 1535.4, 1539.2, and 1549.0, respectively. The Q factor of the cavity was 175.3, 145.5 and 120.1, at $\Delta z = 0$ nm, 100 nm and 200 nm, respectively. The Q factor of nanobeam-based PC^3 is lower than that of L6 PC^3 since the cantilever breaks 2D photonic barrier on the upper side as shown in Figure 5.1b and introduces more leakage for resonance mode in nanobeam-based PC^3.

Figure 5.6a shows the normalized transmittance at the three different values of displacement Δz. The normalized transmittances have a wide valley between 1350 nm and 1520 nm, which correspond to the photonic bandgap of the nanobeam. It's also seen that there are a few peaks in the transmittance beyond 1520 nm, which are induced by the existence of the tip of the cantilever in the center of the nanobeam. At $\Delta z = 0$, a peak occurs at 1535.3 nm, which is close to the simulated resonant wavelength 1535.4 nm. This peak indicates that lights at resonant wavelengths activate the resonant mode of the complex cavity to tunnel through the waveguide device. Similarly, at $\Delta z = 100$ and 200 nm, we have also seen the corresponding peaks in their normalized transmittances, which correspond to the respective resonant modes. Figure 5.6b shows the relation between shift of the transmittance peak wavelengths and bending of cantilever. For the nanobeam-based PC^3 device, a theoretical maximum shift of 13.5 nm is obtained when the cantilever completely bends out of the slab.

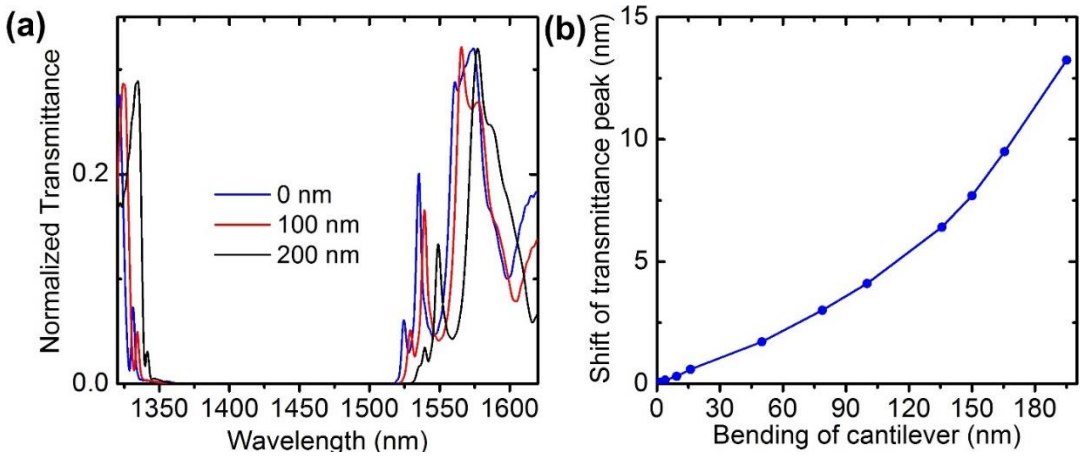

Figure 5.6 For nanobeam-based scheme (a) normalized transmittance at different bindings: 0, 100 and 200 nm; (b) wavelength shift versus bending of cantilever.

5.5 Fabrication and Characterization

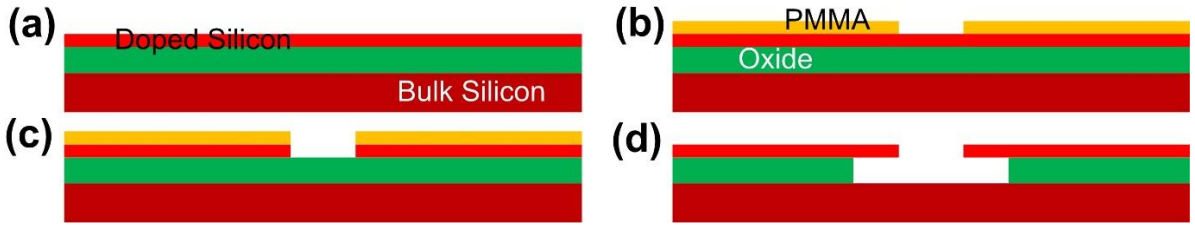

Figure 5.7 Fabrication processes for PC^3. (a) Thinning down and boron doping for better conductivity; (c) transferring pattern into PMMA by E-beam lithography; (d) Reactive ion etching; (e) Releasing cantilever by wet etching and stripping PMMA off.

As shown in Fig. 5.7, the fabrication processes for the two tunable PC^3 devices are similar with what we previously described in Chapter 2. Briefly, the two devices were fabricated on a SOI wafer, where the top silicon layer servers as a device layer and the buried oxide layer servers as a sacrificial layer. First, the top silicon layer was highly doped, partially oxidized, and then thinned down to 200 nm. The patterns of the whole integrated circuit were formed in PMMA resist using e-beam lithography and then transferred to the silicon layer by deep reactive ion etching. After that, wet etching was conducted to release

the cantilever by partially removing the buried oxide, while maintaining the feeding waveguides and nanobeam structures anchored to the handling layer of the SOI wafer.

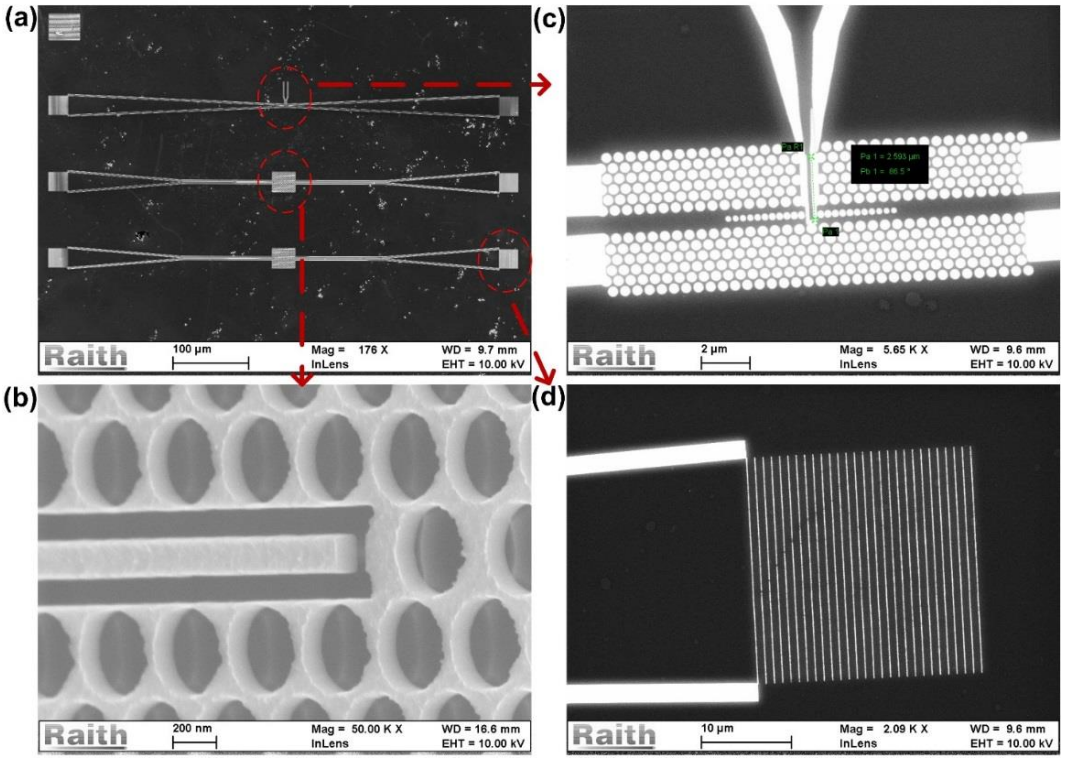

Figure 5.8 (a) Top view of the two PC^3 devices. (b) A cantilever embedded in the L6 PC^3. (c) A nanobeam-based PC^3. (d) Fabricated grating coupler.

Figure 5.8 shows SEM images of the two fabricated PC^3 devices. To facilitate coupling light into and out of the PC^3, two grating couplers with fully etched slots were designed and fabricated [37]. The tapered waveguides were used to connect the grating couplers with the feeding waveguide. Similarly to what we previously discussed in Chapter 3, an incident beam from a 1.55 µm tunable laser was coupled into the device through an input grating coupler and an output light was collected by a multimode fiber aligned to an output grating coupler on the other side. An optical spectrum analyzer (OSA) was used to detect and record the transmission spectrum of the output light. The detection range of the OSA is from 1520 nm to 1620 nm. A D.C. voltage was applied between the surface of the

chip and the back of the SOI wafer. All alignments were achieved under a microscope with the help of a motorized stage.

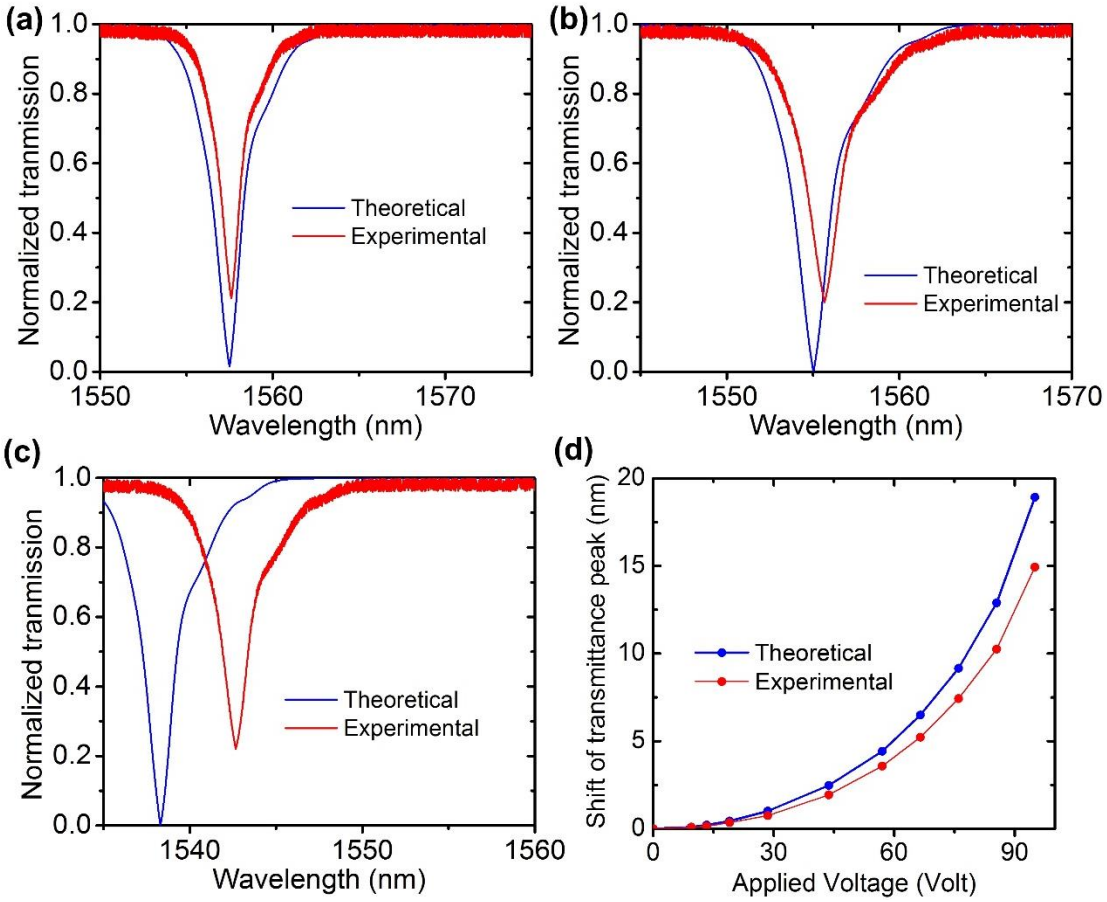

Figure 5.9 Normalized transmittance of the tunable L6 PC^3 at different applied voltages for L6 PC^3: 0 V (a), 45 V (b), and 97 V (c). (d) Resonant wavelength shift versus an applied voltage.

Figures 5.9a-c show normalized transmittance of the L6 PC^3 under different voltage applications: V = 0, 45 V, and 97 V. The normalization is performed based on the reference transmittance of light through the waveguide and two grating couplers, without a PC^3 structure in the center of the waveguide. Without an applied voltage, the experimental transmittance has a dip located at 1557.6 nm, which corresponds to the resonance mode with wavelength of 1557.5 nm and without displacement of cantilever in the L6 PC^3, shown in Figure 5.3b. The experimental transmittance result agrees relatively well with the simulated

one. The slight discrepancy between the experimental and simulated resonance frequencies indicates that the 3D model used in the optical simulations is acceptable. Also, both the experimental and simulated Q factors of this mode (estimated by FWHM of the peak) are near 1500, which is a relatively high value.

We also measured transmittance with different applied voltages and tracked shift of this mode. As shown in Fig. 5.9b, at 45 V, this mode wavelength blue shifts to 1555.7 nm with Q factor of 1102. As the voltage increases to 97 V, the peak wavelength further blue shifts to 1542.7 nm with Q factor of 837. As the voltage increases, the mismatch between the experimental and simulated resonance wavelengths increases to 4.4 nm. Presumably, this is because as the cantilever deflects more, the model used in the FEM and FDTD simulations becomes less accurate than the real one. The Q factor slightly degrades as the cantilever bends down with an increasing applied voltage. This phenomenon has been mentioned in the previous theoretical study of L6 PC^3 (Section 5.4). The root cause is that whole Q factor is mainly determined by Q factor in the planar direction (X-Y plane) and slightly affected by cantilever bending. Figure 5.9d describes the overall tuning capability of the L6 PC^3 device. The maximum wavelength shift is about 15 nm at an applied voltage of 97 V.

For the tunable L6 PC^3 device, it is worthy to note that while the whole device surface experiences a voltage application, the embedded cantilever bends much more significantly than other surrounding parts of the device. Therefore, the negligibly small bending of the other parts of the device surface has almost no influence on the capability of the device to tune its optical properties.

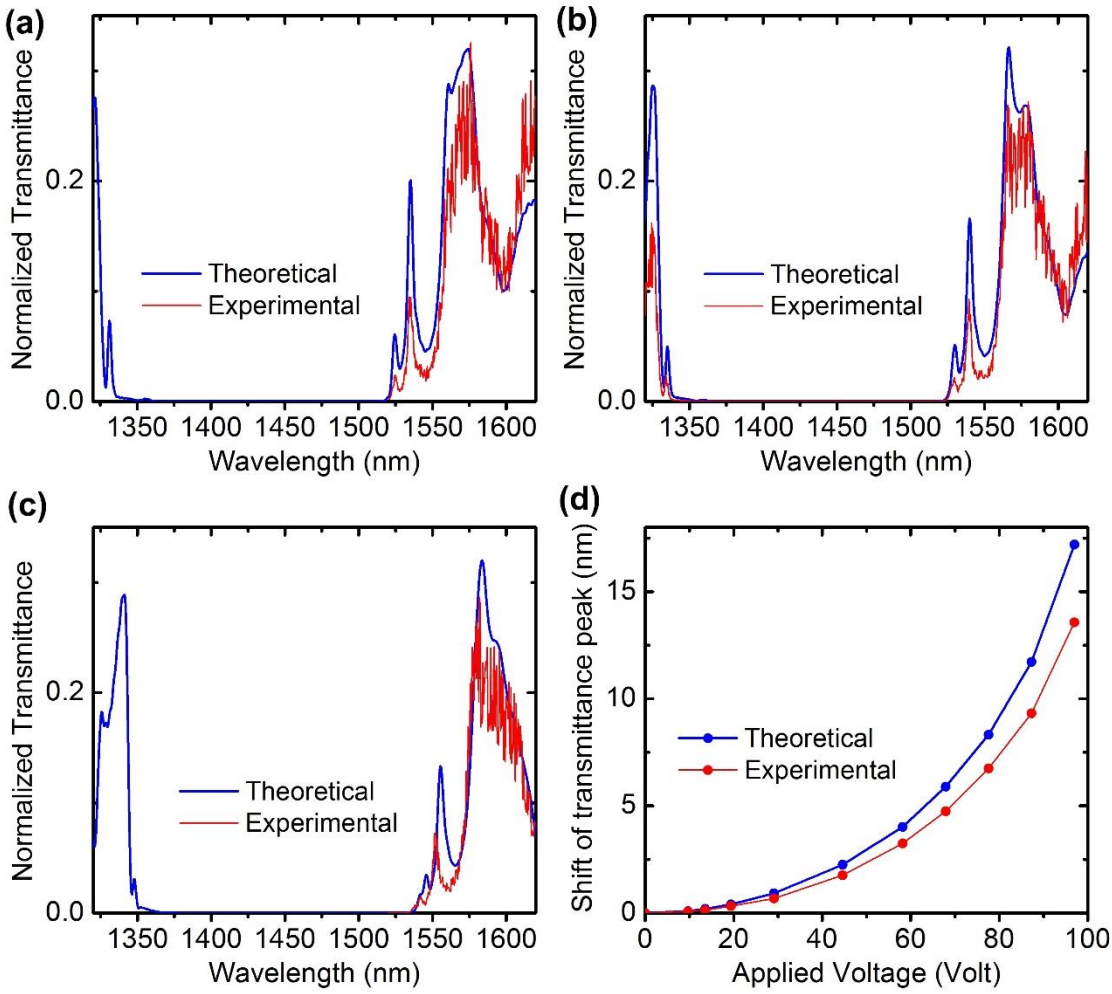

Figure 5.10 Normalized transmittance (theoretical result in blue, measurement result in red) at different applied voltages for nanobeam-based PC^3. (a) V=0 Volt (b) V=45 Volt (c) V = 97 Volt device (d) Wavelength shift versus applied voltage.

Here, we present the experimental results for the tunable nanobeam-based PC^3 device. Figures 5.10a-c show the normalized transmittance of this PC^3 under different applied voltages. Similarly, the normalization is performed based on the reference transmittance of light through the waveguide and two grating couplers, without a PC^3 structure in the center of the waveguide. Without an applied voltage, the normalized transmittance has a wide valley between 1350 nm and 1520 nm, which is due to the photonic bandgap of the 1D PC waveguide of the device. Several peaks are observed in the spectrum

due to the insertion of the tip of the cantilever into the central broken region of the PC waveguide, which correspond to the band-edge modes beyond 1520 nm. The experimental transmittance values match well with the theoretical ones at the peak wavelengths of these band-edge modes. The sharpest peak is located at 1534 nm in the measured spectrum, which is close to the theoretical peak wavelength at 1535 nm. Also, both the experimental and theoretical Q factors of this mode (estimated by FWHM of this peak) are around 371.

Knowing that this mechanical defect introduces a resonance cavity with a good Q factor, we further measured transmittance of the PC^3 at different applied voltages and tracked wavelength shift of this mode. As shown in Fig. 5.10b, at 45 V, the peak wavelength of this mode red shifts to 1540 nm with Q factor decreasing to 305. As the voltage increases to 97 V, the resonance wavelength further shifts to a longer wavelength at 1552 nm with Q factor of 218. The experimental resonance wavelength at 97 V has a 3 nm difference from the theoretical wavelength, which may be due to inaccuracy of the model used in the FDTD simulation. Similarly, the Q factor degrades with increasing deflection of the cantilever under a higher voltage. The reason is as following: the Q factor in the planar direction (X-Y plane in Fig. 5a) was determined mainly by the geometry of the air holes in the broken 1D PC waveguide, while the Q factor in the vertical direction decreases with downward bending of the cantilever that results in a weaker field confinement in this direction. Figure 5.10d shows the overall performance of the PC^3 device on tuning its resonance wavelength. The maximum wavelength shift is 13.5 nm under the voltage of 97 V.

5.6 Conclusion

In this chapter, we developed two tunable PC^3 devices based on a conventional 2D PC platform. The first design involves embedding a nanoelectromechanical cantilever into a L6 cavity in the PC, while the second design involves inserting a similar cantilever into a nanobeam-base waveguide structure. The planar integration of the cantilever into the PC allows not only simplifying the device design and fabrication processes, but also increasing the tunability of the device. We both theoretically and experimentally investigated the optical characteristics of these two devices at different voltage applications. The results show that at 97 V, the maximum resonance wavelength shifts of 15 nm and 13.5 nm are obtained for the L6 PC^3 and the nanobeam-based device, respectively.

References

[1] K. J. Vahala, "Optical microcavities," *Nature*, Vol. 424, pp. 839–846, 2003.

[2] J. L. O'Brien, A. Furusawa, and J. Vuckovic, "Photonic quantum technologies," *Nat. Photonics*, Vol. 3, pp. 687–695, 2009.

[3] J. Leuthold, C. Koos, and W. Freude, "Nonlinear silicon photonics," *Nat. Photonics*, Vol. 4, pp. 535–544, 2010.

[4] M. Eichenfield, J. Chan, R. Camacho, K. J. Vahala, and O. Painter, "Optomechanical crystals," *Nature*, Vol. 462, 78–82, 2009.

[5] D. Van Thourhout and J. Roels, "Optomechanical device actuation through the optical gradient force," *Nat.Photonics*, Vol. 4, 211–217, 2010.

[6] D. G. Grier, "A revolution in optical manipulation," *Nature*, Vol. 424, 810–816, 2003.

[7] D. Psaltis, S. R. Quake, and C. Yang, "Developing optofluidic technology through the fusion of microfluidics and optics," *Nature*, Vol. 442, 381–386, 2006.

[8] M. Notomi, A. Shinya, S. Mitsugi, E. Kuarmochi, H-Y. Ryu, "Waveguides, resonators and their coupled elements in photonic crystal slabs," *Opt. Express*, Vol. 12, 1554–1561, 2004.

[9] C. Kang and S. M. Weiss, "Photonic crystal with multiple-hole defect for sensor applications," *Opt. Express*, Vol. 16, 18188–18193, 2008.

[10] T. J. Wang, C. H. Chu, and C. Y. Lin, "Electro-optically tunable microring resonators on lithium niobate," *Opt. Lett.*, Vol. 32, 2777–2779, 2007.

[11] A. Guarino, G. Poberaj, D. Rezzonico, R. Degl'Innocenti, and P. Gunter, "Electro-optically tunable microring resonators in lithium niobate," *Nat. Photonics*, Vol. 1, 407–410, 2007.

[12] A. Biberman, N. Sherwood-Droz, B. G. Lee, M. Lipson, and K. Bergman, "Thermally active 4x4 non-blocking switch for networks-on-chip," *21st Annual Meeting of the IEEE Lasers and Electro-Optics Society*, pp. 370–371, 2008.

[13] A. Reja,W. H. Charles, G. Fuwan, I. S. Henry, K. Franz, J. R. Rajeev, and A. P. Milos, "Low power thermal tuning of second-order microring resonators," *CLEO/QELS, OSA Technical Digest Series*, pp. CFQ5, 2007.

[14] D. A. Fuhrmann, S. M. Thon, H. Kim, D. Bouwmeester, P. M. Petroff, A. Wixforth and H. J. Krenner, "Dynamic modulation of photonic crystal nanocavities using gigahertz acoustic phonons," *Nat. Photonics*, Vol. 5, 605–609, 2011.

[15] B. G. Lee, A. Biberman, N. Sherwood-Droz, C. B. Poitras, M. Lipson, and K. Bergman, "High-speed 2x2 switch for multiwavelength silicon-photonic networks-on-chip," *J. Lightwave Technol.*, Vol. 27, 2900–2907, 2009.

[16] H. L. R. Lira, S. Manipatruni, and M. Lipson, "Broadband hitless silicon electro-optic switch for on-chip optical networks," *Opt. Express*, Vol. 17, 22271–22280, 2009.

[17] J. Rosenberg, Q. Lin, and O. Painter, "Static and dynamic wavelength routing via the gradient optical force," *Nat. Photonics*, Vol. 3, 478–483, 2009.

[18] G. S. Wiederhecker, L. Chen, A. Gondarenko, and M. Lipson, "Controlling photonic structures using optical forces," *Nature*, Vol. 462, 633–636, 2009.

[19] I. W. Frank, P. B. Deotare, M. W. McCutcheon, and M. Loncar, "Programmable photonic crystal nanobeam cavities," *Opt. Express*, Vol. 18, 8705–8712, 2010.

[20] S. Weiss, H. Ouyang, J. Zhang, and P. Fauchet, "Electrical and thermal modulation of silicon photonic bandgap microcavities containing liquid crystals," *Opt. Express*, Vol. 13, 1090–1097, 2005.

[21] C. L. Smith, U. Bog, S. Tomljenovic-Hanic, M. W. Lee, D. K. Wu, L. O'Faolain, C. Monat, C. Grillet, T. F. Krauss, C. Karnutsch, R. C. McPhedran, and B. J. Eggleton, "Reconfigurable microfluidic photonic crystal slab cavities," *Opt. Express*, Vol. 16, 15887–15896, 2008.

[22] S. Iwamoto, S. Ishida, Y. Arakawa, M. Tokushima, A. Gomyo, H. Yamada, A. Higo, H. Toshiyoshi, and H. Fujita, "Observation of micromechanically controlled tuning of photonic crystal line-defect waveguide," *Appl. Phys. Lett.*, Vol. 88, 011104–1–3, 2006.

[23] T. Takahata, K. Matsumoto and I. Shimoyama, "A wide wavelength range optical switch using a flexible photonic crystal waveguide and silicon rods," *J. Micromech. Microeng.*, Vol. 20, 075009–1–6, 2010.

[24] S. M. C. Abdulla, L. J. Kauppinen, M. Dijkstra, E. Berenschot, M. J. de Boer, R. M. de Ridder and G. J. M. Krijnen, "Mechano-optical switching in a MEMS integrated photonic

crystal slab waveguide," *IEEE 24th Int. Conf. on Micro Electro Mechanical Systems*, pp. 9–12, 2011.

[25] I. Marki, M. Salt, and H. P. Herzig, "Tuning the resonance of a photonic crystal microcavity with an AFM probe," *Opt. Express*, Vol. 14, 2969–2978, 2006.

[26] D. Mao, P. Liu, K. M. Ho, L. Dong, "A theoretical study of a nano-opto-mechanical sensor using a photonic crystal-cantilever cavity", *J. Opt.*, Vol. 14, pp. 075002–1–8, 2012.

[27] J. S. Foresi, P. R. Villeneuve, J. Ferrera, E. R Thoen, G. Steinmeyer, S. Fan, J. D. Joannopoulos, L. C. Kimerling, H. I. Smith and E. P. Ippen, "Photonic-bandgap microcavities in optical waveguides," *Nature*, Vol. 390, 143–145, 1997.

[28] O. Painter, R. K. Lee, A. Scherer, A. Yariv, J. D. O'Brien, P. D. Dapkus, and I. Kim, "Two-dimensional photonic band-gap defect mode laser," *Science*, Vol. 284, 1819–1821, 1999.

[29] J. Ctyroky, "Photonic bandgap structures in planar waveguides," *J. Opt. Soc. Am. A*, Vol. 18, 435–441, 2001.

[30] M. Notomi, E. Kuramochi, and H. Taniyama, "Ultrahigh-Q nanocavity with 1D photonic gap," *Opt. Express*, Vol. 16, 11095–11102, 2008.

[31] P. Velha, E. Picard, T. Charvolin, E. Hadji, J. C. Rodier, P. Lalanne and E. Peyrage, "Ultra-high Q/V Fabry-Perot microcavity on SOI substrate," *Opt. Express*, Vol. 15, 16090–16096, 2007.

[32] Y. Zhang and M. Loncar, "Ultra-high quality factor optical resonators based on semiconductor nanowires," *Opt. Express*, Vol. 16, 17400–17409, 2008.

[33] Q. Quan, P. B. Deotare, and M. Loncar, "Photonic crystal nanobeam cavity strongly coupled to the feeding waveguide," *Appl. Phys. Lett.*, Vol. 96, 203102–1–3, 2010.

[34] Q. Quan and M. Loncar, "Deterministic design of wavelength scale, ultra-high Q photonic crystal nanobeam cavities," *Opt. Express*, Vol. 19, 18529–18542, 2011.

[35] V. A. Mandelshtam and H. S. Taylor, "Harmonic inversion of time signals and its applications," *J. Chem. Phys.*, Vol. 107, pp. 6756−6769, 1997.

[36] A. F. Oskooi, D. Roundy, M. Ibanescu, P. Bermel, J. D. Joannopoulos, and S. G. Johnson, "MEEP: A flexible free-software package for electromagnetic simulations by the FDTD method," *Comput. Phys. Commun.*, Vol. 181, pp. 687−702, 2010.

[37] Bernd Schmid, Alexander Petrov and Manfred Eich, "Optimized grating coupler with fully etched slots," *Opt. Express*, Vol. 17, pp. 11066−11076, 2009.

CHAPTER 6. THEORETICAL STUDY OF TWO-DIMENSIONAL RECONFIGURABLE PHOTONIC CRYSTAL

6.1 Background

PIC technology is a technical trend and revolutionary breakthrough in such diverse applications as optical communication, bio/chemical sensing, and photonic computing [1, 2]. Considerable efforts have been made to develop a large number of PICs (e.g., optical waveguides [3], resonators [4], multiplexers [4], attenuators [5], and detectors [6]), with high level of integration, low power consumption, and fast response. However, many of the existing PICs are application specific and each device often relies on a specified design and manufacturing protocol. To minimize the complexity and potential cost of developing a large number of application-specific PICs, it is highly desirable to develop reconfigurable PICs capable of configuring and reconfiguring various photonic functionalities on a single chip to accommodate different application needs [7, 8].

2D PCs result from drilling periodic air hole lattices in a high index membrane [9]. A wide range of PC-based PICs have been developed, including waveguide bends [10], resonators [11], spectral filters [12], add-drop multiplexers [4], and super prisms [13]. But, they are often static since their functionalities are fixed by fabrication. It is well known that PC resonant cavities are a basic element of building many of these PC-based devices and can be formed, simply by introducing a defect to a periodic PC [9]. Interestingly, the optical properties of a PC cavity can be tuned, by changing its effective refractive index via different mechanisms such as free-carriers injection [14], optical Kerr effect [15], optothermal tuning [16], liquid crystal infiltration [17], and micro/nanofluidic tuning [18]. Recently, micro/nano-electro-mechanical systems (MEMS/NEMS) technology has been exploited in tunable and

reconfigurable optical devices [19-21]. Several mechanically tunable PC-based devices have been realized or proposed by utilizing controlled disturbance of a mechanical component at the micro/nanometer scale to the evanescent or resonant part of the optical field of a PC device [22-32]. For example, the optical transmittance of a PC waveguide can be modulated by bringing a microplate close to the waveguide [22], and by changing the height difference between a PC slab and silicon rods [23]. Also, the resonance wavelength of a PC cavity can be tuned by moving a scanning probe microscope and an atomic force microscope probe close to the cavity [30, 31]. More remarkably, in Ref. [28] Zhou et al. proposed a novel device concept for a reconfigurable optoelectronic integrated circuit by designing, modeling, and fabricating of a photonic crystal membrane (slab) device with MEMS activated waveguide. Cantilever layer was designed to insert a line of posts into holes in photonic crystal membrane to create a defect line that forms or alters an optical waveguide.

In this chapter, we take the next step from work that has previously demonstrated the effective interaction between a mechanical component and the optical field of a PC cavity. To exploit even higher flexibility and functionality to make sophisticated integrated circuit such as L-shaped waveguide, we theoretically demonstrated the possibility of forming a highly reconfigurable PIC device by individually introducing a different number of plugs into corresponding air holes of a PC. As shown in Figure 6.1a, an array of micro/nanoscale plugs was initially placed above the PC, with each plug aligned with each air hole of the PC. The possible fabrication method to make this device is to combine addressable integrated electronic circuit which could be embedded in a layer underneath the PC slab layer with movable MEMS-based plugs layer above slab. Electrostatic force could be induced by electronic circuit and used to actuate the each plug individually.

We assumed that each plug could be individually controlled to insert into and lift up from an air hole via MEMS/NEMS technology, serving as a local refractive index modulator for each photonic unit of the PC. Although a lot of photonic functionalities potentially can be pursed in the PC slab by inserting different plugs into their corresponding air holes, this chapter demonstrated configuring three typical photonic building blocks, including a point-defect resonant cavity, a line-defect straight waveguide, and a 60o waveguide bend. It should be noted that the focus of this work was on (i) designing the plugs and PC slab for the proposed reconfigurable PIC device, (ii) examining the optical properties of the three building blocks configured on the PC, and (iii) investigating the influence of possible fabrication, alignment, and mechanical actuation errors on the optical properties of the configured building blocks, while the design of a MEMS/NEMS actuator for controlling the vertical position of these plugs was out of scope of this chapter.

6.2 Model Structure

Figure 6.1b shows a cross-sectional schematic view of the present reconfigurable PIC device. A 2D PC with a triangular lattice was designed in the top silicon (Si) layer of a Si-on-insulator (SOI) wafer. The top Si layer and the oxide (SiO_2) layer of the SOI wafer was 0.75 *a* and 3 *a* in thickness, respectively, where *a* was the lattice constant of the PC. The Si handling substrate of the wafer was 750 μm thick. The diameter of the air holes of the Si PC was set to be $d = 0.8\ a$, allowing us to obtain photonic band gap (PBG) for transverse-electric (TE)-like modes. To minimize the field leakage into the handling substrate, the oxide layer underneath of the PC was removed. An array of identical cylindrical Si plugs was placed above the PC. The diameter of the plugs was set to be $D = 0.6\ a$. The minimum height of the

plugs was found to be H_{min} = 4.25 *a*. The reason that we chose these two structural parameters will be discussed later. The distance or gap between the bottom surface of the Si plugs and the top surface of the PC was denoted by G. These mechanical plugs protruded downward from a MEMS/NEMS actuator. As mentioned earlier, the actuator was assumed to be able to control the vertical position of the individual plugs.

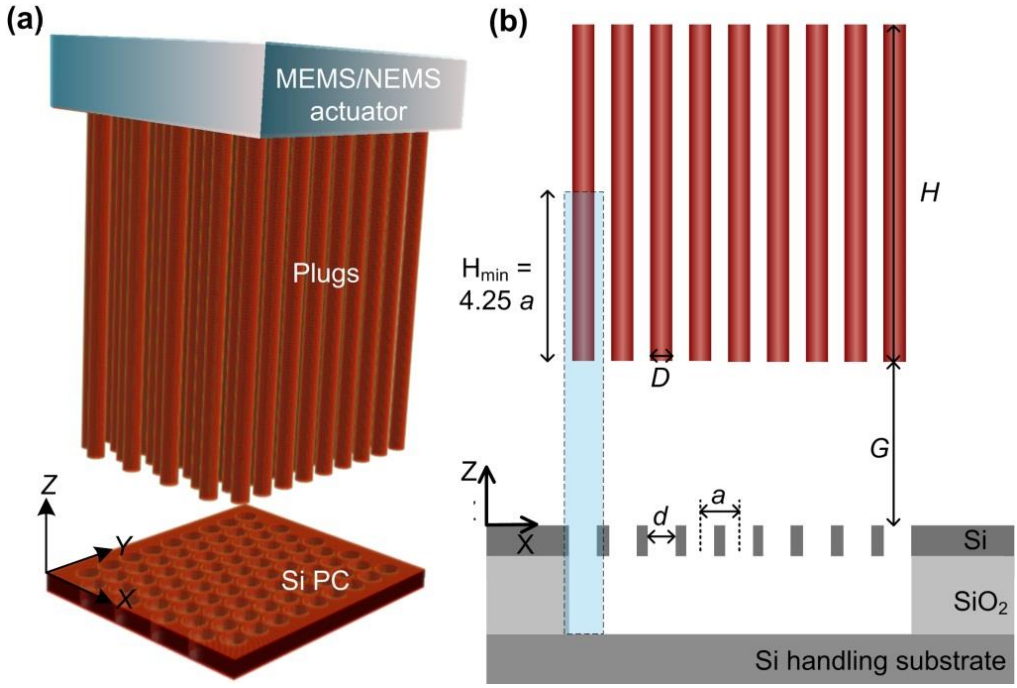

Figure 6.1 Schematic structure of the reconfigured PIC device consisting of a 2D Si PC, an array of Si plugs, and an MEMS/NEMS actuator. (a) 3D view. (b) Cross-sectional view. Each plug was designed to align with each air hole of the PC. The actuator was assumed to be able to control the vertical position of individual plug. Drawings are not to scale.

6.3 Photonic Band Diagram

The band structure of the PC depended on how close the plugs were to the PC. We defined the minimum distance between the bottom surface of the plugs and the top surface of the PC (or G_{min}) as the critical distance beyond which the TE-like band gap of the PC with plugs was similar to that without plugs. To compute the band diagram of the PC with a

different G, the 3D PWM method with periodic boundary conditions was used during simulations. All plugs could simultaneously move up and down relative to the PC. The computing region covered a unit cell of the PC, the lower part of a plug, and the gap between the unit cell and the plug (see the dashed-line frame in Figure 6.1b and the insets in Figures 6.2a-c). We note that the whole length of the plug could be $H \geq H_{min} = 4.25\ a$, but, to simplify the simulation, the upper part of the plug (beyond 4.25 *a* from the bottom surface of the plug) was excluded from the computing region (Figure 6.1b). This simplification was reasonable since the upper part of the plug actually would not affect the band gap of the PC (discussed later). We truncated the simulation space by using a 9 *a* thick air layer to enclose the solution volume. The handling substrate was also excluded from the computing region since little field was found to reach this layer through the 3 *a* thick air layer (also discussed later). Rectangular coordinates were used to simplify computation since the Γ-X direction in rectangular coordinates was equivalent to the Γ-M direction in triangular coordinates for wave-vector space.

Figure 6.2a shows the band structure of the PC when no any plug was used (or G = infinity). The result demonstrates that the TE-like band gap ranged from 0.2591 a / λ to 0.2705 a / λ, but no TM-like band gap occurred beneath the light cone of the band diagram. After the plugs were introduced to the PC with $0 \leq G \leq 0.75\ a$, no TE-like band gap was found (Figure 6.2b). As G increased further, the TE-like band gap emerged and increased. When $G = 4.5\ a$, the band gap spanned from 0.26041 a / λ to 0.2708 a / λ (Figure 6.2c), which was almost similar to that found with no plug. As shown in Figure 6.3a, when $G \geq 4.5\ a$, the band gap remained unchanged. Therefore, the plugs must initially be located at least 4.5 *a* away from the top surface of the PC (or $G \geq G_{min} = 4.5\ a$). Furthermore, by choosing *a*

= 410 nm, the central wavelength of the band gap was set to be around the telecommunication wavelength of 1550 nm.

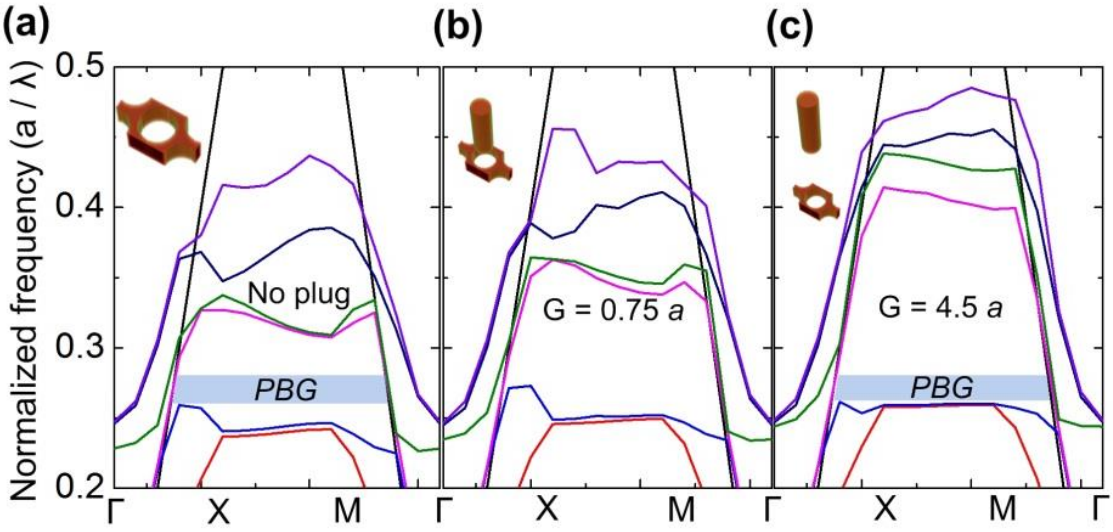

Figure 6.2 Band structures for the TE-like modes of the PC with a different initial distance G between the bottom surface of the plugs and the top surface of the PC: G = infinity (a), 0.75 a (b), and 4.5 a (c). The computing structure used for the PWM simulation is shown in the insets of this figure and the dashed-line frame in Figure 1b.

We examined the influence of possible fabrication errors on the band gap of the PC. Considering that the plugs needed to be placed at least 4.5 *a* above the top surface of the PC at the initial state of the device, here we studied the case of G = 4.5 *a* for illustrating the fabrication error versus photonic band structures as shown in Figure 6.3b. Also, as mentioned earlier, when G = 4.5 *a*, the plugs had little influence on the band gap. This allowed us to only take into account the fabrication error in the air hole diameter of the PC. As a result, we applied random errors with a certain maximum magnitude (in the form of a percentage of the ideal air hole diameter) to the ideal air hole diameter (d = 0.8 a). Specifically, for a given magnitude of randomness introduced, the Pseudo-Random function of the C++ Library was used to generate ten different sets of random errors, and then, each set was applied to the ideal air hole diameter for simulation. Thus, the upper and lower bounds of each band gap in

Figure 6.3b were obtained by averaging the results of the ten simulations. It is shown that the band gap of the PC reduced as the error in the air hole diameter increased. When the magnitude of error was 6 %, the TE-like band gap of the PC decreased to be from 0.2617 a / λ to 0.2675 a / λ, which was about the half of the band gap of the ideal PC (with no fabrication error).

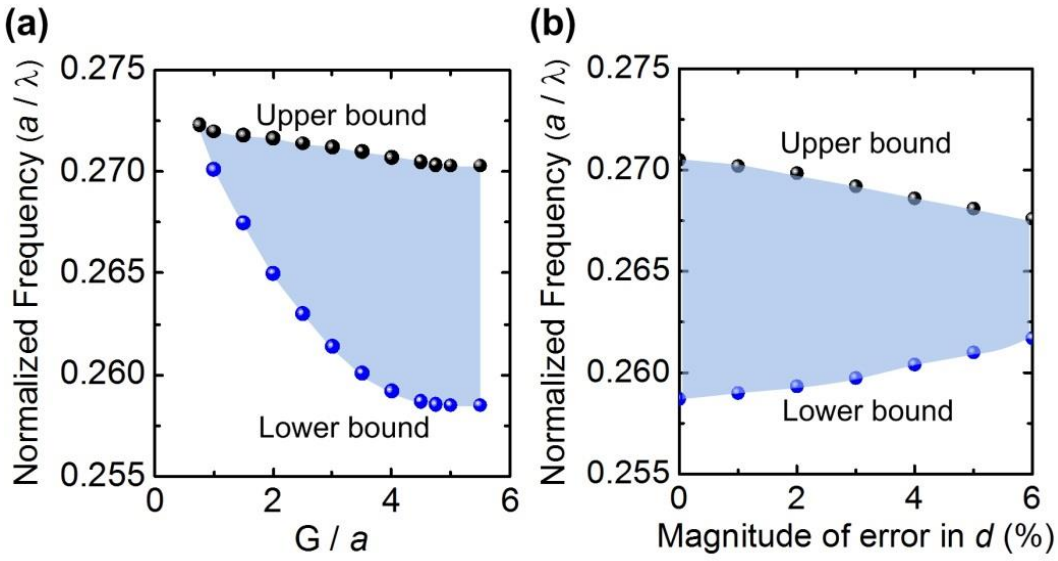

Figure 6.3 (a) TE-like band gap of the PC as a function of an initial distance G between the bottom surface of the plugs and the top surface of the PC. (b) TE-like band gap of the PC as a function of magnitude of error in the air hole diameter (in the form of a percentage of the ideal air hole diameter d = 0.8 a).

6.4 Point-defect Photonic Crystal Resonant Cavity

To demonstrate the formation of a simple point-defect resonant cavity in the PC, a plug was positioned in an air hole in the PC, as shown in Figure 6.4a. The lower level of the plug was positioned at the bottom surface of the PC. Electromagnetic simulation was performed by using the 3D FDTD method with the freeware package MEEP [33]. The computing region covered the lower part of the plugs (4.25 a thick), an air gap (4.5 a thick), a PC, and an air layer (3 a thick) underneath the PC, from top to bottom of the device (Figure 6.4a). A 200 nm thick perfectly matched layer (PML) was applied at the boundaries of the

entire computing region. The grid resolution was 10 nm. A TE-polarized pulse line source with a Gaussian frequency distribution was placed vertically along the Z direction and offset by 20 nm from the spatial center of the air hole of interest. The line source was set at the same height as the PC. The resonance wavelength and Q factor of the resonant cavity were computed by the Harminv [34]. To record mode profiles, a continuous-wave line source at resonance was used.

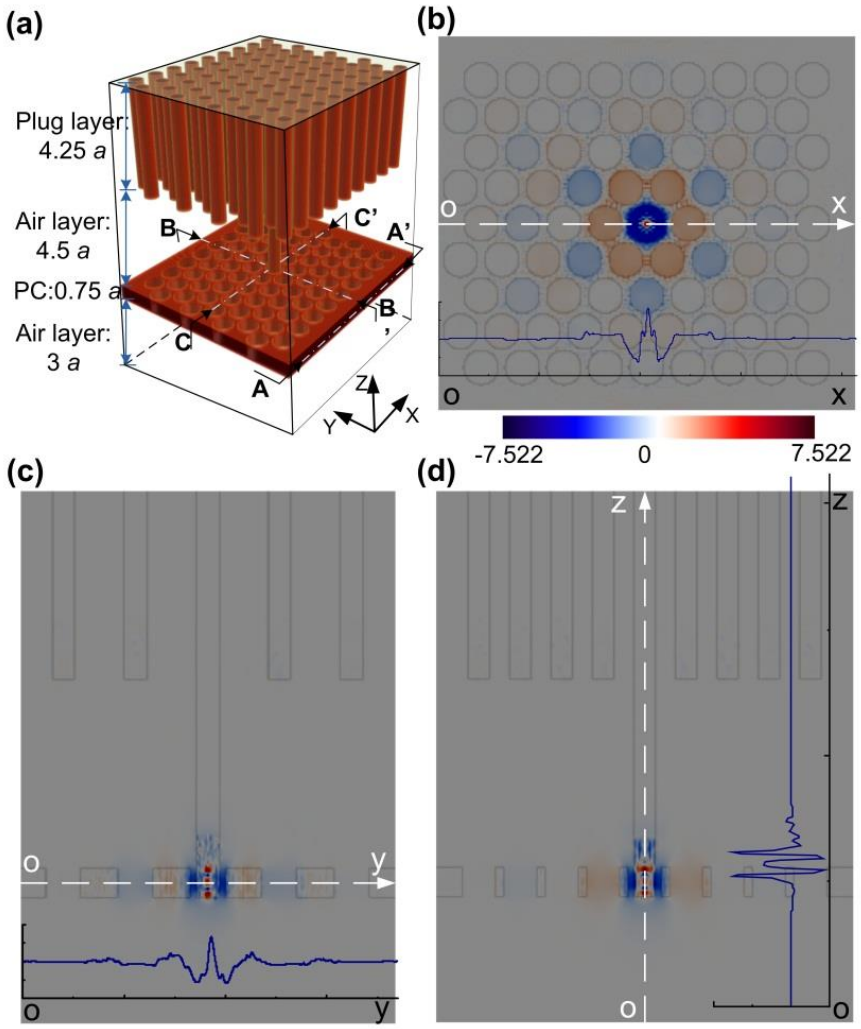

Figure 6.4 (a) Schematic representation for the computing region used in the FDTD simulation for a point-defect resonant cavity configured in the PC. A 200 nm thick PML (not shown here) was used to enclose the entire computing volume. (b)-(d) E-field (amplitude) distributions of the TE-like mode (λ = 1552.8 nm) in the plane of X-Y (b), Y-Z (c), and X-Z (d), at the cross section of A-A', B-B', and C-C', respectively, shown in (a). The insets in (c) and (d) show the field profiles along the dashed lines. The intensity scale is an arbitrary unit (not shown in the insets).

Figures 6.4b-d show the electric field distributions for the plug-induced defect mode (λ = 1552.8 nm) of the PC cavity. A stable mode profiles were recorded after propagation of 1000 wavelengths distance. The result shows that the defect mode of the configured cavity had a dipole mode profile. The cavity was able to localize the mode field in all three dimensions. By extracting the field profiles along the X and Y directions at the spatial center of the cavity, the decay rate of the field intensity with distance from the spatial center of the cavity was found to be 42.4 and 44.3 dB μm^{-1} in the X and Y directions, respectively (see the insets of Figures 6.4b-c). Also, in the vertical downward direction, there was little field leakage into the air layer beneath the PC (Figure 6.4d). This allowed us to exclude the Si handling substrate in the simulation structure (Figure 6.4a). Interestingly, the field leakage upward into the inserted plug was also limited (Figure 6.4d). The field decayed rapidly into the plug away from the top surface of the PC, with the decay rate of 114.8 dB μm^{-1}. The result provided us with an important guideline to define the minimum length of the plug or H_{min} that was needed to eliminate any possible influence of the actuator on the optical properties of any photonic circuit configured in the PC. Specifically, we defined H_{min} as the critical length of the plug at which the mode field intensity reduced by 200 dB. Thus, H_{min} was calculated to be 4.25 *a* (or 1.74 μm). As a result, it was reasonable to exclude the upper part (beyond 4.25 *a* from the bottom surface) of the plugs from the computing region in Figure 6.1b.

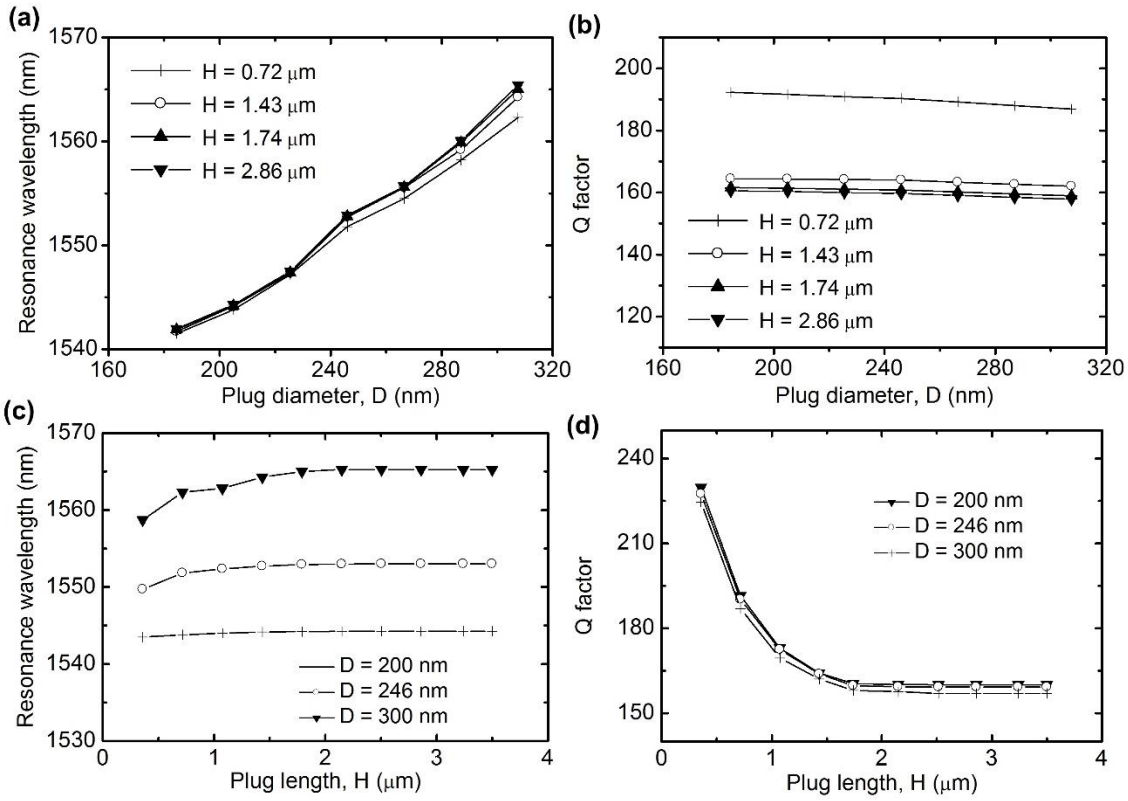

Figure 6.5 (a) Resonance wavelength of the plug-induced PC resonant cavity as a function of D for a different H. (b) Q factor of the cavity as a function of D for a different H. (c) Resonance wavelength of the cavity as a function of H for a different D. (d) Q factor of the cavity as a function of H for a different D.

We investigated the influences of D and H on the resonance wavelength and Q factor of the plug-induced PC cavity. As shown in Figure 6.5a, the resonance wavelength red-shifted as D increased. This is attributed to an increase in the effective refractive index of the cavity. To obtain the resonance wavelength of the cavity near 1550 nm, we chose D = 0.6 *a* (or 246 nm). It is shown in Figure 6.5b that the Q factor of the cavity was little influenced by D. We know that generally, the Q factor of a defect mode is composed of an in-plane (Q_{plane}) and an out-of-plane component ($Q_{vertical}$) and is determined by $1/Q = 1/Q_{plane}+1/Q_{vertical}$ [9]. The PBG effect of a PC allows for light confinement in the planar direction, and thus, Q_{plane} is mainly determined by the periodicity and lattice constant of the PC. Therefore, changing the plug diameter would pose limited influence on the Q_{plane} component, and thus, the total Q factor of the cavity. On the other hand, with increasing H, the resonance wavelength of the

cavity red-shifted at low H values and remained almost unchanged at high H values (Figure 6.5c). This is because when the plug was short, the whole plug was regarded as part of the cavity and increasing its length led to an increase in effective index of the cavity. However, when a long plug was used, increasing the upper part of the plug had little influence on changing the effective index of the cavity. As a result, no change in resonance wavelength occurred with increasing H further. Also, since the plug provided a pathway for the mode field to leak upward, the $Q_{vertical}$ component, and thus, the total Q factor, of the cavity dropped as H increased (Figure 6.5d). Similarly, the Q factor became little influenced by the presence of a large H. Although any H, as long as $H \geq H_{min} = 4.25\ a$, was acceptable in principle, we continued to use $H = H_{min} = 4.25\ a$ in the 3D computing region in all following simulations to reduce the simulation load. Specifically, with $D = 0.6\ a$ (or 246 nm), $H = H_{min} = 4.25\ a$ (or 1.74 μm), and $G = G_{min} = 4.5\ a$ (or 1.85 μm), the resonance wavelength and Q factor of the cavity was computed to be 1552.8 nm and 160.8, respectively. The -20 dB mode volume of the cavity was as small as 0.155 μm^3.

Next, we investigated the influences of possible errors in fabrication, alignment, and mechanical actuation on the optical resonance wavelength and Q factor of the configured PC cavity with $D = 0.6\ a$ and $H = 4.25\ a$. Figure 6.6a shows that as the magnitude of fabrication error in the air hole diameter increased to 6 % (a percentage of the ideal air hole diameter), the resonance of the cavity changed randomly by less than 5 nm, while its Q factor deceased dramatically from 160 to 91. Actually, the size error may occur in both the PC and plugs. Here we focused on the error of the air hole diameter of the PC because the changing tendencies of the optical properties with D and H of the plugs were already revealed in Figure 6.5. The lateral alignment error was defined by the misalignment of the plug's axis

with the vertical axis of the air hole in the planar directions. Figure 6.6b demonstrates that the lateral random shift of the activated plug had a quite limited effect on both the resonance wavelength and Q factor. This is attributed to the unchanged effective index of the cavity and the fixed lattice periodicity of the PC used. Furthermore, the mechanical actuation error or the vertical position error of the plug referred to the vertical shift of the plug off the bottom surface of the PC. As shown in Figure 6.6c, because the vertical position error of the plug resulted in a significant change in the effective refractive index of the cavity, the upward unwanted deviation of the plug from the bottom surface of the PC caused a blue shift of the resonance wavelength and a degradation of the Q factor. Figure 6.7 displays the electric field distributions in the cavity with the air hole diameter error of 6 %, the plug lateral position error of 41 nm, and the plug vertical position error of 154 nm (half of the PC slab thickness). The result indicates that with these structural errors, it was still possible to build a cavity to operate in a resonant mode near the communication wavelength.

We note that the Q factor of the configured cavity was relatively low. But, many excellent methods are available to realize a high Q factor for a PC cavity [35-39]. It is believed that there would be an improvement of the Q factor through optimization of the device structure. This discussion, however, is out of the scope of this chapter.

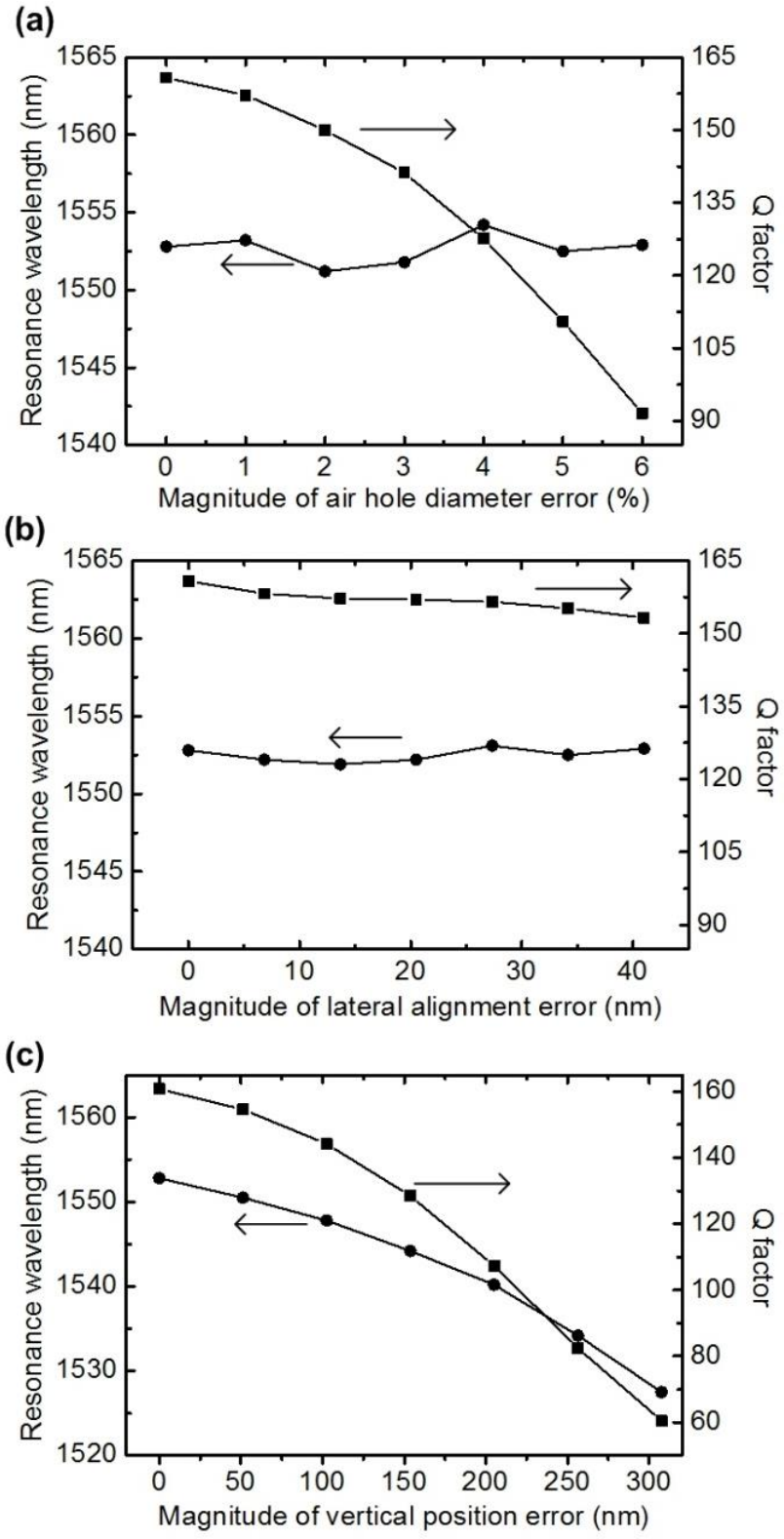

Figure 6.6 Resonance wavelength of the plug-induced PC resonant cavity as a function of air hole diameter randomness (a), lateral alignment error of the axes between the actuated plug and the air hole (b), and vertical position error of the plug or an unexpected distance from the bottom surface of the air hole (c).

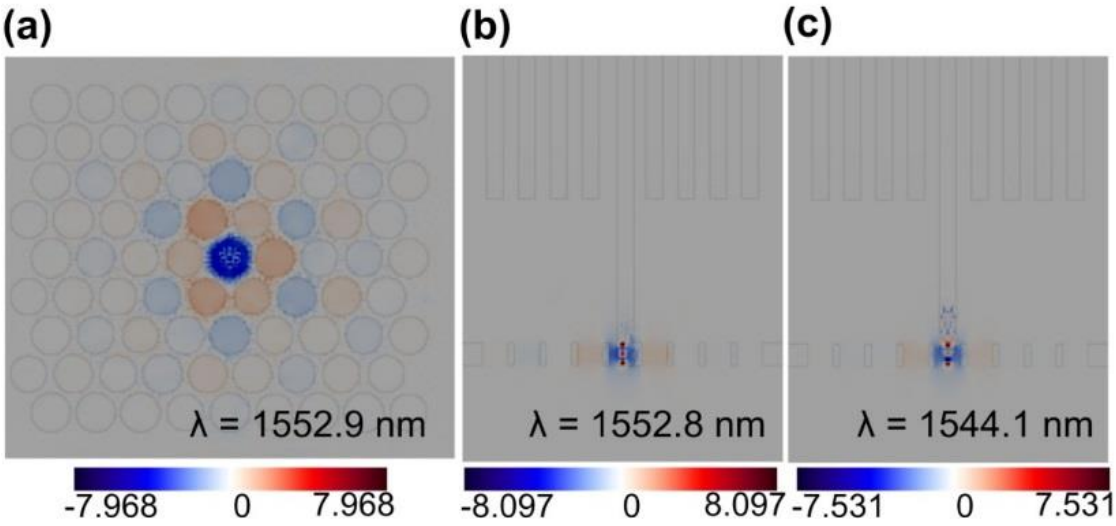

Figure 6.7 Electric field (amplitude) distributions of the TE-like mode at the A-A' cross section with the air hole randomness of 6 % (a), at the B-B' cross section with the plug lateral alignment error of 41 nm (b), at the C-C' cross section with the plug vertical position error of 154 nm (above the bottom surface of the air hole). The locations of A-A', B-B', and C-C' sections are the same as those shown in Figure 6.4. The defect mode wavelength for each case is shown in each panel.

6.5 Line-Defect Photonic Crystal Straight Waveguide

To configure a straight waveguide in the PC, a line of plugs was inserted into corresponding air holes in the PC (Figure 6.8a). D = 0.6 *a* (or 246 nm), H = H_{min} = 4.25 *a* (or 1.74 μm), and G = G_{min} = 4.5 *a* (or 1.85 μm) were used for forming the line-defect PC straight waveguide. We first computed the band diagram (dispersion curves) for the waveguide along the Γ-X direction of the triangular lattice in wave-vector space, using the 3D PWM method. As shown in the inset of Figure 6.8b, the supercell used in this simulation contained one period in the Γ-X direction, four periods in the X-M direction (normal to the Γ-X direction), and five plugs with the central one inserted in the corresponding air hole. Among the lower fourteen bands of the line-defect modes found in Figure 6.8b, there were two bands (see the red and blue dash-dot lines) occurring in the TE-like band gap of the perfect PC. The light blue region in Figure 6.8b was obtained from Figure 6.2c. The upper

band (the red dash-dot line) covered the normalized frequency from 0.2635 *a* / λ to 0.2705 *a* / λ, while the lower one (the blue dash-dot line) from 0.2591 *a* / λ to 0.2705 *a* / λ that actually covered the whole band gap region. The results demonstrate that the guided TE-like defect modes in this configured straight waveguide existed and could be guided horizontally by the band gap and vertically by index guiding.

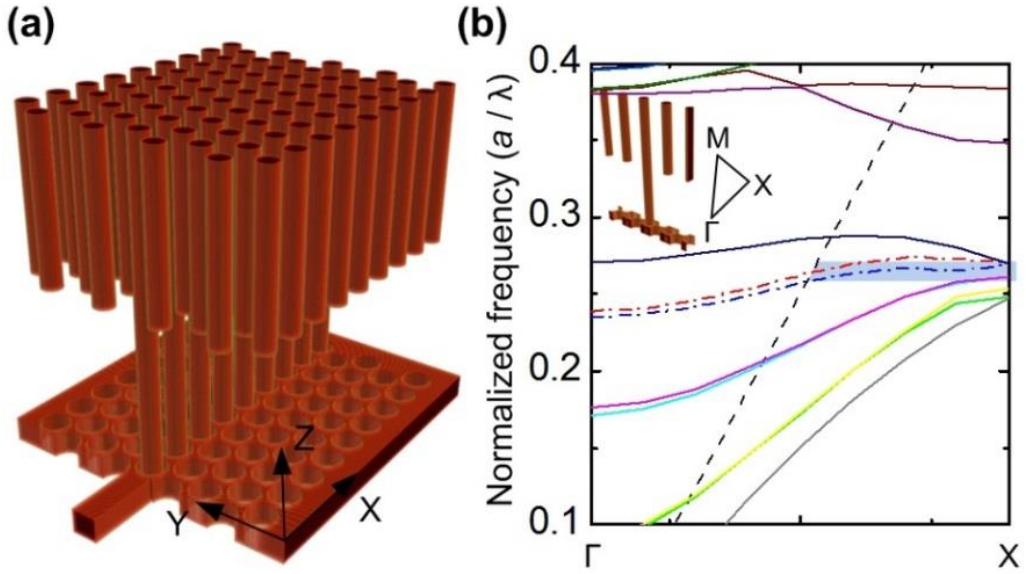

Figure 6.8 (a) Schematic representation for a straight waveguide configured in the PC. The waveguide was formed by introducing a line of plugs into corresponding air holes of the PC. X, Y, and Z represent real space. (b) Band diagram for the straight waveguide along the Γ-X direction (or the propagation direction of the waveguide). Γ, X, and M represent the corresponding plane in wave-vector space for X-Y plane in real space. PBG region is shaded by blue color. Fourteen lines represent band of modes, and among them two specific dash-dot lines go across with PBG region, representing line-defect modes.

It is known that in a conventional line-defect PC waveguide, part of the guided mode (lying above the light line of the air-claddings) energy may leak off the waveguide in the plane due to an insufficient number of lattice periods. Also, the guided mode couples with the radiation mode, radiating wave energy out of the plane. In the configured PC straight waveguide studied here, the upper part of the plugs protruded from the top surface of the PC and inevitably influenced the coupling between the guided mode and radiation mode in the vertical or Z direction of the PC. Thus, we computed the transmittance, loss, and reflectance

spectra of the waveguide using the FDTD method. The computing region is shown in Figure 6.9a, where a TE-polarized light was coupled into the PC laterally through a short input waveguide. The transmitted power through this configured waveguide was monitored by an output detector at the exit of the waveguide. The in-plane and out-of-plane loss of power from the waveguide was monitored by four detectors at the upper, lower, back and front planes of the computing region shown in Figure 6.9a.

Figures 6.9b-d display the electric field distributions of the line-defect guided mode at the wavelength of 1553.5 nm after propagation of 1000 wavelengths. The guided mode was well confined within the configured waveguide (Figure 6.9b). The protruding part of the inserted plugs (from the top surface of the PC) provided multiple optical pathways for the guided mode to vertically leak out of the PC (Figures 6.9c and d). The mode field decayed rapidly upward into the plugs and the average decay rate over the nine inserted plugs was computed to be 49.5 dB μm^{-1}. On the other hand, the field that went down into the air layer (underneath the PC) decayed at a rate of 148.1 dB μm^{-1}, which was much faster than that went upward into the plugs. This observation may be attributed to the removal of the oxide from underneath the Si PC as shown in Figure 6.1b.

Figure 6.10 shows the power flow along the propagation direction of the guided mode. The power flow was monitored at the exit of the configured waveguide (in the Y-Z plane at the spatial center of the last air hole from the left; see the inset of Figure 6.10) and normalized to the power measured at the inlet of the configured waveguide (in the Y-Z plane at the spatial center of the first air hole from the left). It was found that the decay rate of the optical power through this configured waveguide was as low as 0.30 dB μm^{-1}.

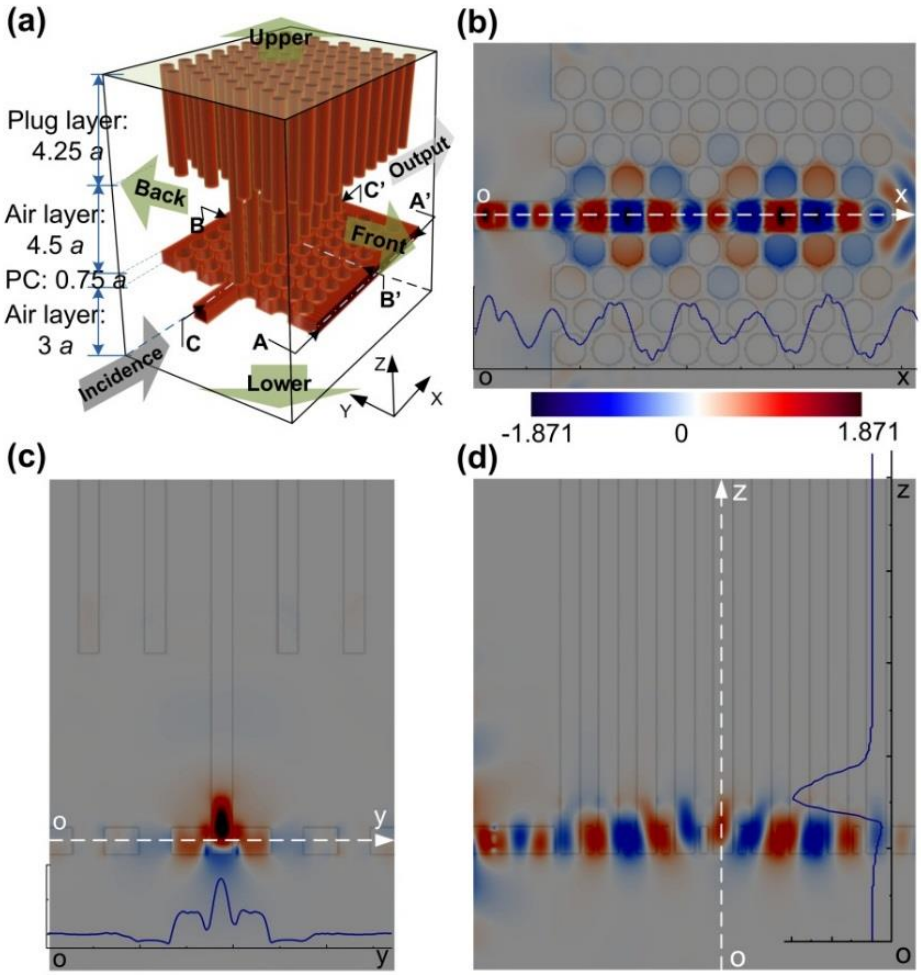

Figure 6.9 (a) Schematic representation for the computing region and detection planes used in the FDTD simulation for a configured line-defect PC straight waveguide. (b)-(d) E-field (amplitude) distributions of the TE-like mode (λ = 1553.5 nm) in the plane of X-Y (b), Y-Z (c), and X-Z (d), at the cross section of A-A', B-B', and C-C', respectively. The insets in (b)-(d) show the field profiles along the dashed white lines shown in the corresponding panels. The intensity scale is an arbitrary unit (not shown in the insets).

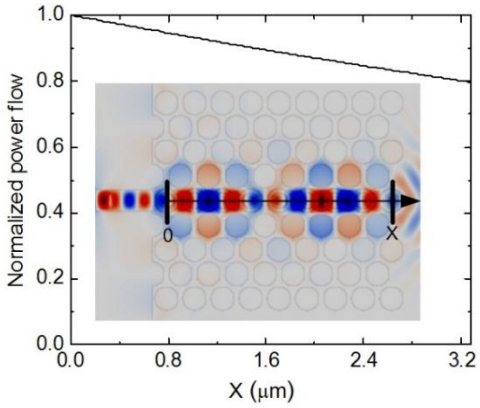

Figure 6.10 Normalized power flow of the guided mode at λ = 1553.5 nm through the configured line-defect PC straight waveguide. The power detection plane was defined to be a square area with 2 a long on each side in the Y-Z plane.

Figure 6.11 depicts the transmittance, loss, and reflectance spectra of the configured straight PC waveguide. The transmittance peak of 78 % was located at 1553.5 nm with a full width at half maximum (FWHM) of ~18 nm. The optical loss detected at the upper plane (see the detection plane in Figure 6.9a) was 7.0 % at the peak transmission wavelength and a maximum of 11.4 % at 1545.4 nm, which sits about the center of bandgap mentioned in section III. In contrast, the optical loss detected at the lower plane was 3.0 % at the peak transmission wavelength and a maximum of 3.2 % at 1551.3 nm. Due to the symmetrical device structure in the Y direction, the loss power detected at the front and back sides of the computing region (see the two detection planes in Figure 6.9a) were the same (6.4 %).

Figure 6.12a shows the influence of possible air hole diameter error on the peak transmittance and corresponding wavelength of the configured straight PC waveguide. As the magnitude of the error increased by 6 % of the ideal air hole diameter (d = 328 nm or 0.8 a), the peak transmittance dramatically decreased by ~38 % and the peak wavelength increased by ~11 nm. On the contrary, the lateral misalignment of the axes between an actuated plug and corresponding air hole had little influence on the resulting transmission peak wavelength. As shown in Figure 6.12b, as the axis of a plug was laterally shifted off the axis of an air hole by 41 nm, no conclusive pattern of the tendency of plot was observed. We believe that this is because the lattice periodicity of the PC remained unchanged. There was a distinct decrease, however, in the peak transmittance of the waveguide.

The mechanical actuation of the plugs may be in error of their stop position and two types of error may occur: A) the actuated plugs stopped at the same but wrong vertical position, and B) each of the actuated plugs had a random error in their vertical position. In the former case A (Figure 6.12c), the deviation of the plugs from the bottom surface of the

air holes caused a decrease in the peak transmittance and a blue shift in the transmittance peak wavelength. When the bottom surface of the actuated plugs was located at the same level with the top surface of the PC (deviating from the bottom of the air holes by 308 nm or the whole slab thickness), the peak transmittance of the configured waveguide deceased to ~9 % due to the field leakage in the vertical direction. This result, more importantly, indicates that the deeper the plugs were inserted into the air holes, the higher the peak transmission could be obtained, although we believe, to some extent, that keeping the movement of the actuated plugs outside of the PC would alleviate the challenge of the geometric alignment between the plugs and PC. In the latter case B, where the plugs may be stopped at different vertical positions inside the air holes, the peak transmittance of the waveguide dropped more significant than that in the case A. As seen in Figure 6.12d, the peak transmittance deceased to ~18 % as the magnitude of the vertical random position error increased to 100 nm.

Figures 6.13a-d display the TE-like mode profiles of the configured straight waveguide with the maximum structural errors respectively studied in the aforementioned four cases (Figures 6.12a-d). The results here further demonstrate that the mechanical actuation-induced errors of the plug position in the vertical direction caused more field energy leakage than the size and alignment errors in the lateral direction.

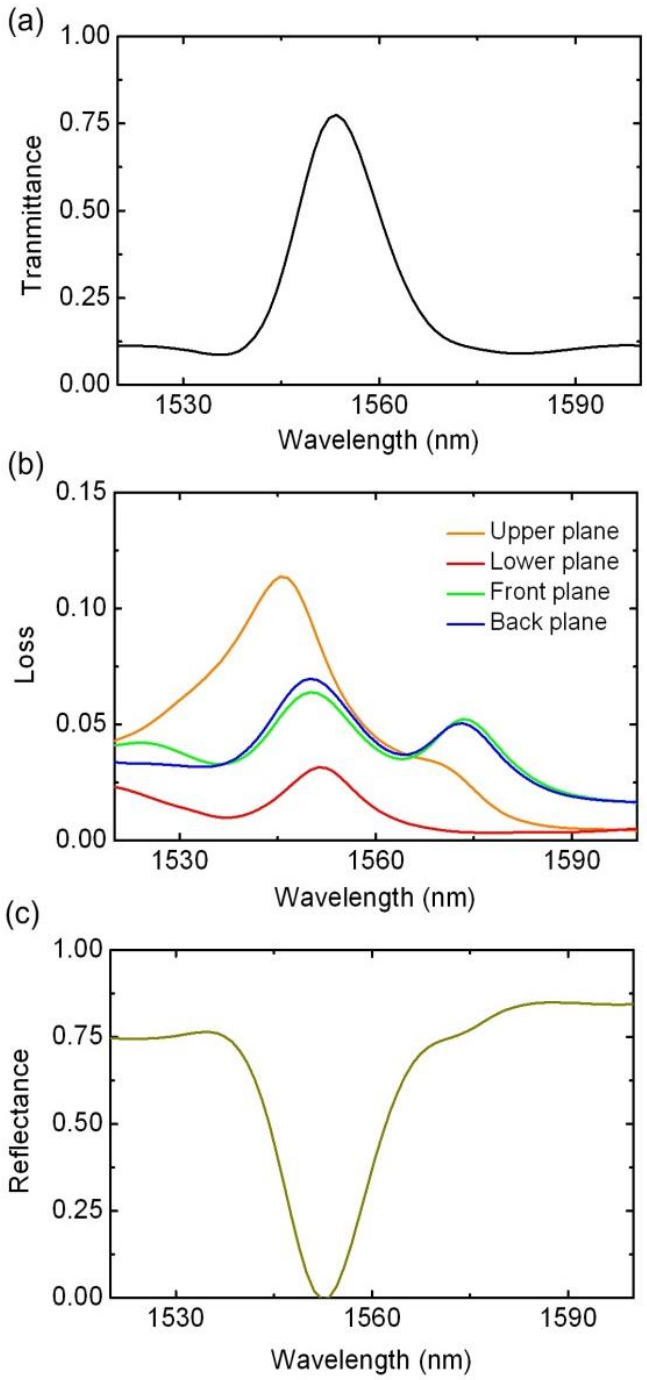

Figure 6.11 Transmittance (a), loss (b) and reflectance (c) spectra of the configured PC straight waveguide with a TE wave incidence.

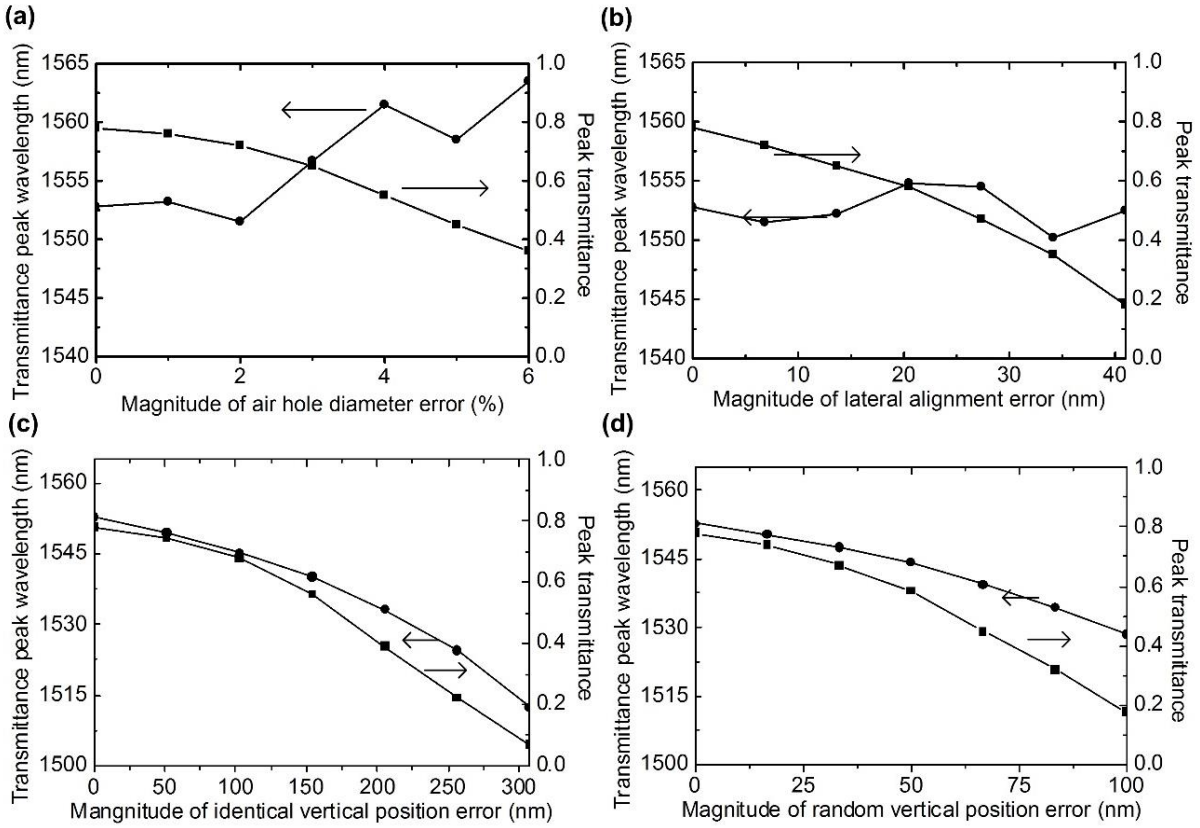

Figure 6.12 Transmittance peak wavelength (left) and peak transmittance (right) of the configured PC straight waveguide as function of an air hole diameter randomness in the form of a percentage of the ideal air hole diameter (a), lateral alignment error or lateral offset of the actuated plugs with the center of corresponding air holes (b), identical vertical position error of the actuated plugs or the unexpected distance between the plugs and the bottom surface of corresponding air holes (c), and random vertical position error of the actuated plugs (d).

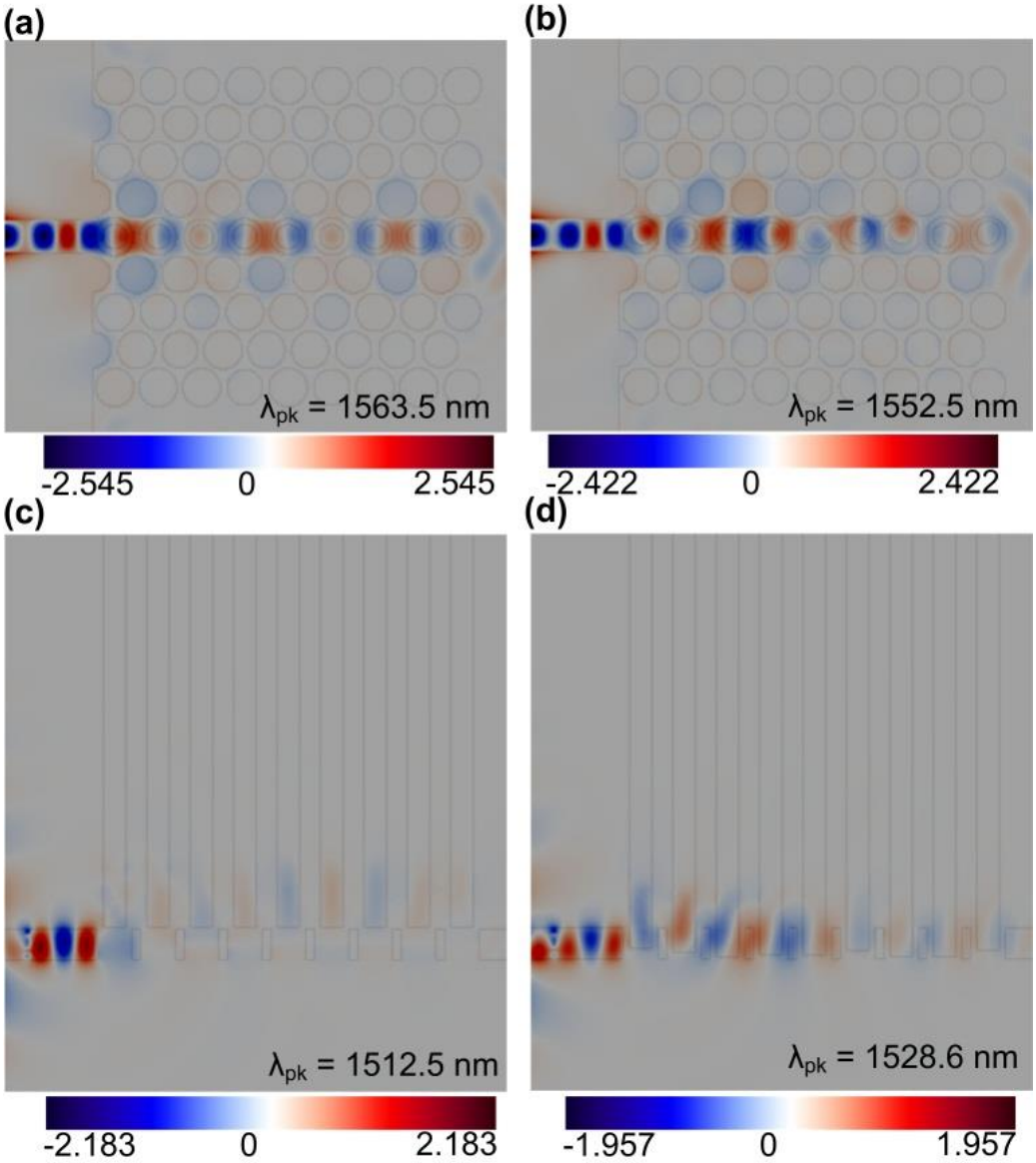

Figure 6.13 Electric field distributions of the TE-like mode in the configured PC straight waveguide at the A-A' cross section with the magnitude of random air hole diameter error at 6 % (a), at the A-A' cross section with the lateral misalignment of the actuated plugs with the center of the air holes at 41 nm (b), at the B-B' cross section with the identical vertical position error of the plugs at 308 nm (c), and at the B-B' cross section with the random vertical position of the plugs at 100 nm. The locations of A-A' and B-B' sections are the same as those labeled in Figure 6.9. The peak transmission wavelength λpk in each case is shown in each panel.

6.6 Line-defect Photonic Crystal Waveguide Bend

The ability to guide light waves in sharp bends of PICs is one of the most important properties of PC waveguides. To configure a waveguide bend in the PC, two lines of plugs with an intersection angle of 60° were inserted into their corresponding air holes of the PC, to

form two waveguide segments for the waveguide bend, as shown in Figure 6.14a. The intersection angle was determined by the triangular lattice used in the PC. We considered the waveguide bend formed by two straight waveguides and a bend corner. To examine the defect modes of the configured waveguide bend, we computed the band diagram (dispersion curves) of the bend corner. As shown in the inset of Figure 6.14b, the supercell lattice contained three units with the inserted plugs and seven lattice periods in the X-M direction in the triangular coordinates. In the resultant band diagram shown in Figure 6.14b, there were three defect modes (see the red, blue, and green dash-dot lines) crossing the whole TE-like band gap of the perfect PC (the light blue region in Figure 6.14b was obtained from Figure 6.2c). Therefore, it was possible for the three line-defect guided modes in the band gap to be coupled from one straight waveguide segment to the other through the bend corner.

Similar to the previously configured PC straight waveguide, the transmittance of this configured 60^{o} waveguide bend was largely determined by the in-plane and out-of-plane loss of power. The in-plane loss was mainly affected by the coupling efficiency between the guided propagation modes of the two straight waveguide segments. The field energy leakage upward into the plugs led to the out-of-plane loss. Thus, we conducted the FDTD simulation for the configured waveguide bend. In this simulation, the same structural parameters were used: D = 0.6 a (or 246 nm), H = H_{min} = 4.25 a (or 1.74 μm), and G = G_{min} = 4.5 a (or 1.85 μm). The computing region and detection planes are shown in Figure 6.15a, where a TE-polarized source (the same source as the one used in the simulation for the configured straight waveguide) was placed vertically at the termination side of the short input waveguide.

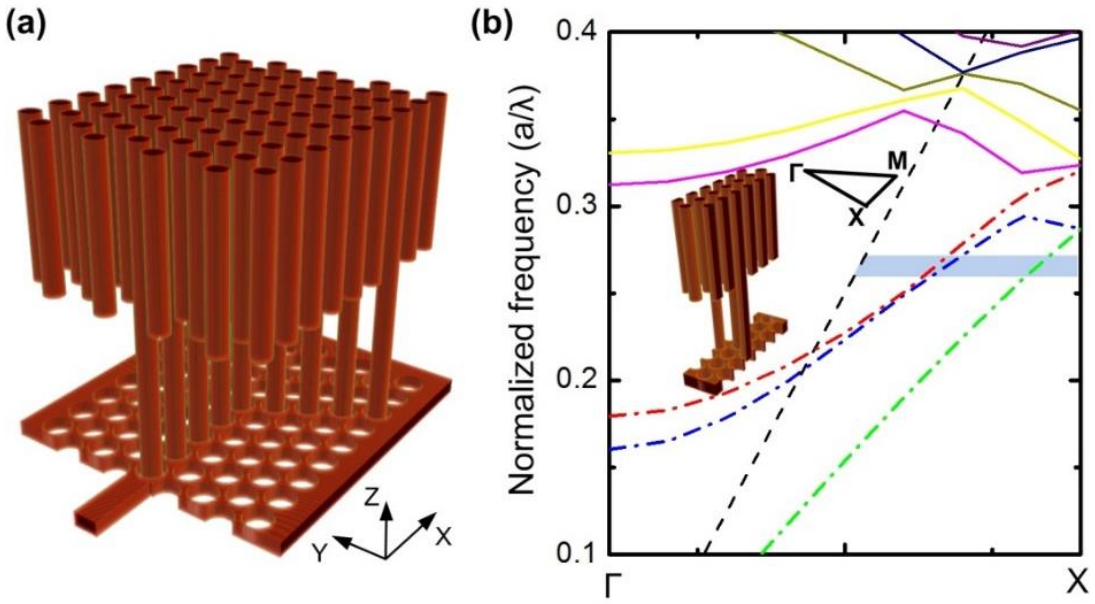

Figure 6.14 (a) Schematic view for a PC waveguide bend configured in the PC by introducing two lines of plugs into their corresponding air holes with an intersection angle of 60o. X, Y, and Z represent real space. (b) Band diagram for the configured waveguide bend. Γ, X, and M represent the corresponding plane in wave-vector space for X-Y plane in real space.

Figures 6.15b-d show that the guided mode at the wavelength of 1553.5 nm (after propagation of 1000 wavelengths) was well confined in both of the planar and vertical directions. The guided mode wave propagated from the first straight waveguide segment (see the segment X1 in Figure 6.15b) to the second one (see the segment X2 in Figure 6.15b) along the Γ-X direction through the bend corner. In the vertical direction, the field intensity decayed rapidly upward into the plug and downward into the air layer, with the decay rate of 47.5 and 73.7 dB μm^{-1}, respectively. Figures 6.16a and b show the normalized power flow of the guided mode through the two respective segments X1 and X2 along the Γ-X direction. The average decay rate of power for X1 and X2 was 0.31 and 0.32 dB μm^{-1}, respectively. Note that the detection plane at the exit of X1 was set in the Y-Z plane, while the detection plane at the entrance of X2 was set in the plane 60^o off the Y-Z plane (see the insets in Figure 6.16). Due to the non-unity light coupling efficiency from X1 to X2, the power detected at the exit of the X1 segment (P1) was higher than that detected at the entrance to the X2

segment (P2). Thus, the coupling efficiency of the bend corner was calculated to be P2 / P1 = 0.91.

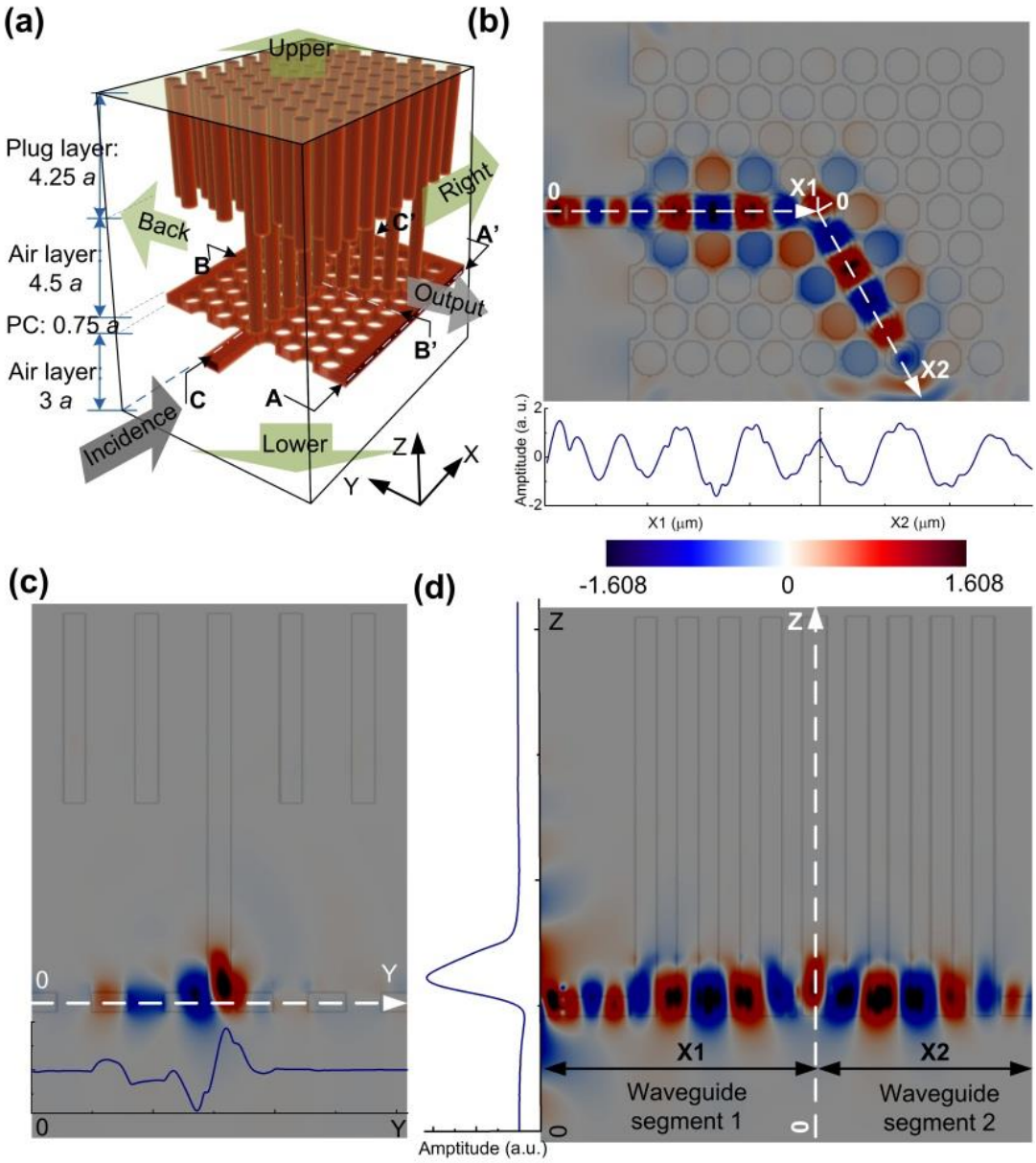

Figure 6.15 (a) Schematic representation for the computing region and detection planes used in the FDTD simulation for a configured PC waveguide bend. (b, c) E-field (amplitude) distributions of the guided mode (λ = 1553.5 nm) in the plane of X-Y (b) and Y-Z (c) at the cross section of A-A' and B-B', respectively. (d) E-field (amplitude) distribution of the guided mode in the vertical direction of the waveguide bend. This image was formed by combining the field distributions along the straight waveguide segment X1 in the X-Z plane and along X2 in the plane 60o off the X-Z plane. The insets in (b)-(d) show the field profiles along the corresponding dashed lines in the field distribution images. The intensity scale is an arbitrary unit (not shown in the insets).

Figure 6.17 shows the transmittance, loss, and reflectance spectra of the configured

PC waveguide bend. The peak transmittance of the waveguide bend was 0.68 locating at the mode wavelength of 1553.5 nm, with the FWHM of ~17 nm (Figure 6.17a). The loss power detected at the right, back, upper, and lower detection planes of the PC (see the locations of these planes in Figure 6.15a) was 17.6 %, 6.3 %, 4.3 %, and 1.4 %, respectively, at 1553.5 nm. The relatively large optical loss at the back and right sides was probably attributed to the coupling loss between the two straight PC waveguide segments at the bend corner.

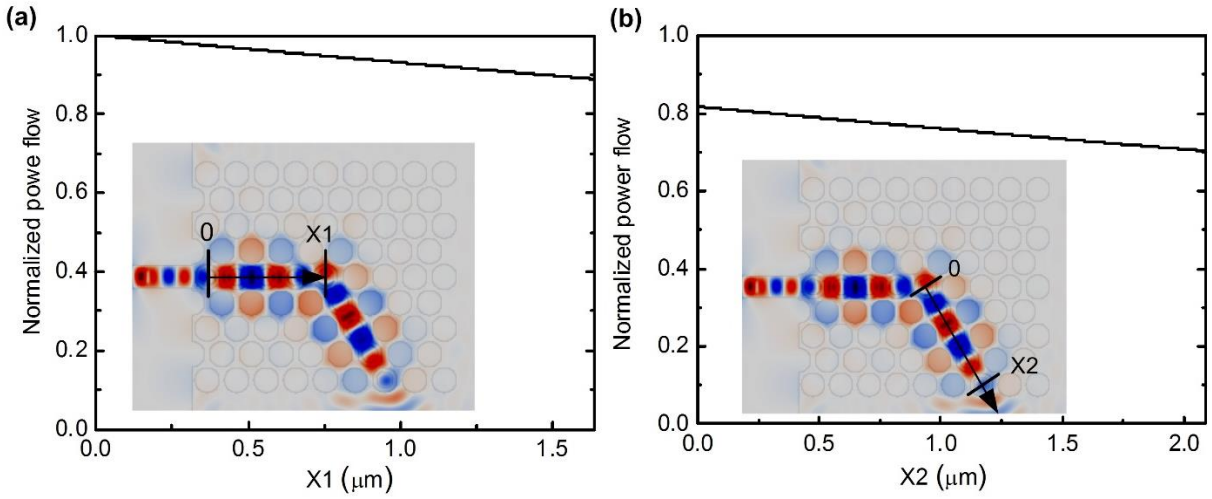

Figure 6.16 Normalized power flow of the guided mode (1553.5 nm) through the two straight waveguide segments X1 (a) and X2 (b), for the configured PC waveguide bend. The power detection plane was defined to be a square area with 2 a long on each side in the plane normal to the propagation direction.

Figure 6.18a shows that as the magnitude of possible fabrication error in the air hole diameter of the PC increased by 6 % of the air hole diameter at 328 nm, the peak transmittance decreased from 71 % to 30 % and the peak wavelength shifted by less than 10 nm. Similar to the aforementioned straight PC waveguide, the lateral alignment error of the actuated plugs caused a significant decrease in the peak transmittance. The peak transmittance deceased to 14 % when the magnitude of the lateral alignment random error of the plugs was 41 nm (Figure 6.18b). Furthermore, similarly, both the identical and random vertical position errors of the plugs resulted in a larger loss in the peak transmittance than the

errors in the air hole diameters and the lateral alignment between the air holes and plugs. Specifically, the peak transmittance deceased to ~5 % as the magnitude of the vertical identical position error of the plugs was at 308 nm (Figure 6.18c), and ~15% the random position error at 100 nm (Figure 6.18d).

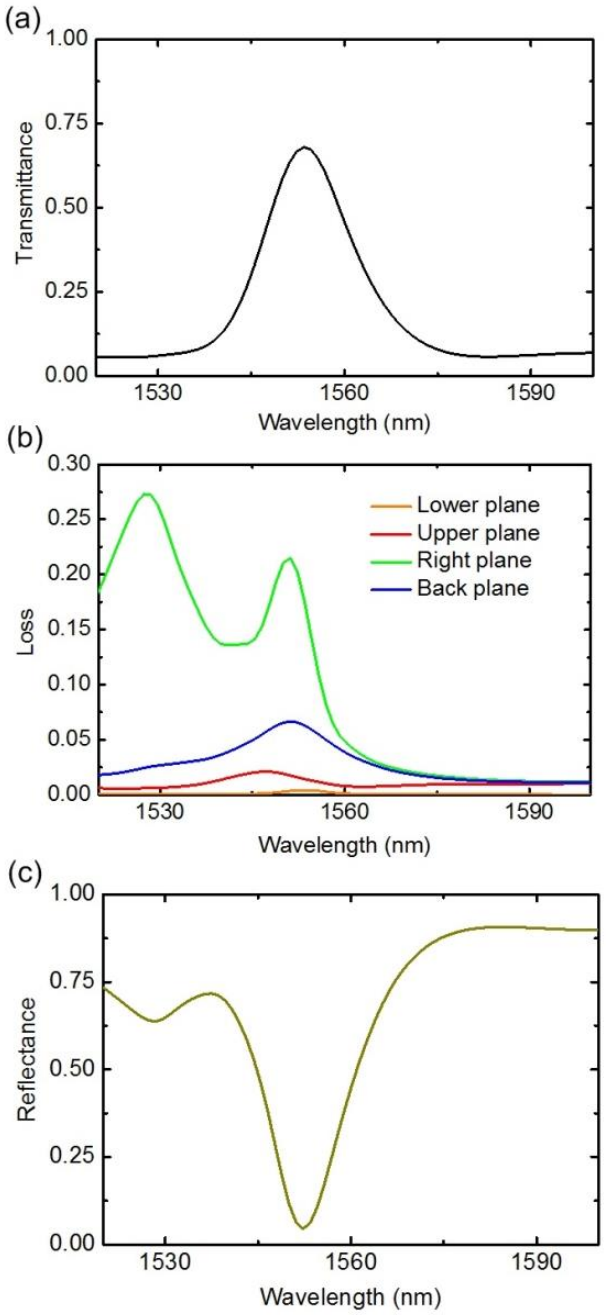

Figure 6.17 Transmittance (a), loss (b) and reflectance (c) spectra of the configured 60o waveguide bend with a TE wave incidence.

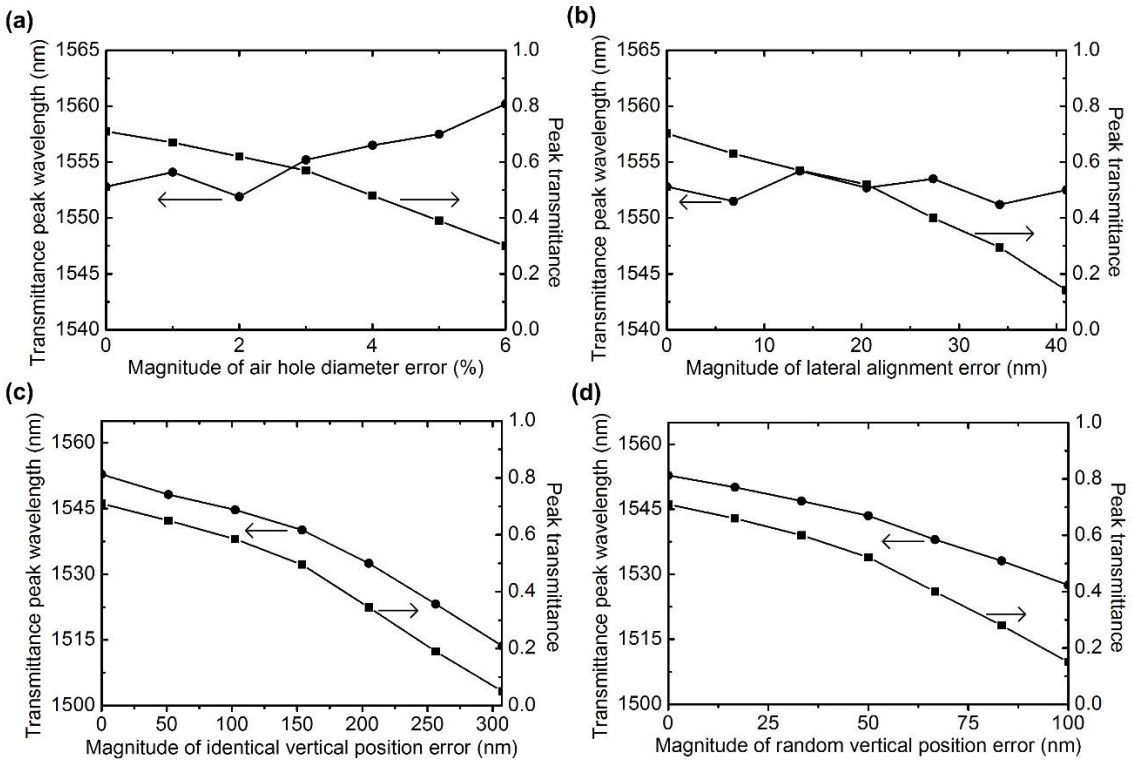

Figure 6.18 Transmittance peak wavelength (left) and peak transmittance (right) of the PC waveguide bend as function of air hole diameter randomness in the form of a percentage of the ideal air hole diameter (a), lateral alignment error or lateral offset of the actuated plugs with the center of corresponding air holes (b), identical vertical position error of the actuated plugs or the unexpected distance between the plugs and the bottom surface of corresponding air holes (c), and random vertical position error of the actuated plugs (d).

6.7 Conclusion

We studied a nano-opto-mechanical reconfigurable PIC device that consisted of an array of Si plugs and a conventional 2D Si PC. The simulation was based on the assumption that each plug could be individually introduced into its corresponding air hole in the PC. We showed that no TE-like band gap occurred when all plugs were placed $\leq 0.75\ a$ from the top surface of the PC and that the plugs had no influence on the band gap of the PC when they were placed $\geq 4.5\ a$ from the PC. A single-defect resonant cavity was configured, by inserting a plug into an air hole in the PC. As the plug diameter increased, the resonance wavelength of the cavity significantly red-shifted, while its Q factor was hardly influenced. As the plug length increased, the Q factor of the cavity reduced, while its resonance

wavelength only slightly red-shifted. A line-defect straight waveguide was configured by inserting a straight line of plugs into the corresponding air holes. 7.0 % of the power flow in the mode field was lost through upward leakage into the plugs. The peak transmittance of 78 % was achieved in the configured PC straight waveguide over nine lattice periods. Lastly, a PC waveguide bend was configured by inserting two straight lines of plugs into the air holes with the intersection angle of 60^{o}. The loss power through upward leakage into the plugs was 4.3 %. The peak transmission of the waveguide bend was 68 %. The coupling efficiency of the bend corner was 91%. By systematically investigating the influence of the possible fabrication, alignment, and mechanical actuation errors on the optical properties of the configured building blocks, we found that the mechanical actuation-induced errors of the plug position in the vertical direction could influence the optical properties of the configured PICs more significantly than the size error in the air hole diameter and the lateral alignment error between the air holes and plugs. Besides the three basic photonic building blocks, many other photonic functions can be realized on the PC via appropriate insertion of plugs into corresponding air holes. By combining these basic building blocks, a variety of basic and complex circuits (e.g., splitter, mirror, add-drop filter, Mach–Zehnder interferometer, wavelength-division multiplexer, etc.) can be formed in a single photonic chip.

We believe that this theoretical study can benefit our efforts toward realizing a fully reconfigurable nano-opto-mechanical PIC platform. Future work includes design and fabrication of an actuator for individual control of plugs, and integration of the actuator and PC slab to realize the proposed device. Actually, there are many existing remarkable MEMS/NEMS devices that use a 2D array of individually controlled micro/nanostructures. For example, in the Millipede MEMS-based scanning-probe data-storage device, a large

number of Si probes are used to address individual storage units below the probes based on a thermo-mechanical actuation and sensing mechanism [40-41]. Also, millions of micro-mirrors are individually controlled by a conventional electrostatic actuation mechanism [42]. These technologies provide important clues for the development of the movable plugs for the proposed device in the future.

References

[1] L. Thylen, M. Qiu, and S. Anand, "Photonic crystals - a step towards integrated circuits for photonics," *ChemPhysChem*, Vol. 5, pp. 1268−1283, 2004.

[2] X. Chen, C. Li, and H. K. Tsang, "Device engineering for silicon photonics," *NPG Asia Materials*, Vol. 3, pp. 34−40, 2011.

[3] Y. A. Vlasov, M. O'Boyle, H. F. Hamann, and S. J. McNab, "Active control of slow light on a chip with photonic crystal waveguides," *Nature*, Vol. 438, pp. 65−69, 2005.

[4] A. Vorckel, M. Monster, W. Henschel, P. H. Bolivar, and H. Kurz, "Asymmetrically coupled silicon-on-insulator microring resonators for compact add-drop multiplexers," *IEEE Photonic. Tech. Lett.*, Vol. 15, pp. 921−923, 2003.

[5] K. Hirabayashi, M. Wada, and C. Amano, "Liquid crystal variable optical attenuators integrated on planar lightwave circuits," *IEEE Photonic. Tech. Lett.*, Vol. 13, pp. 609−611, 2001.

[6] L. Chen, K. Preston, S. Manipatruni, and M. Lipson, "Integrated GHz silicon photonic interconnect with micrometer-scale modulators and detectors," *Opt. Express*, Vol. 17, pp.15248−15256, 2009.

[7] C. L. Smith, B. Uwe, S.Tomljenovic-Hanic, et al., "Reconfigurable microfluidic photonic crystal slab cavities," *Opt. Express*, Vol.16, pp. 15887−15896, 2008.

[8] D. Mao, P. Liu, and L. Dong, "All-optical programmable photonic integrated circuit: An optical analogy to electronic FPGA IEEE transducer," *The 16th International Conference on Solid-State Sensors, Actuators and Microsystems (TRANSDUCERS)*, pp. 2674−2677, 2011.

[9] J. D. Joannopoulos, S. G. Johnson, J. N.Winn, and R. D. Meade, *Photonic Crystals: Molding the Flow of Light, 2nd ed. Princeton*, NJ: Princeton Univ. Press, 2008.

[10] A. Mekis, J. C. Chen, I. Kurland, S. Fan, P. R. Villeneuve, and J. D. Joannopoulos, "High transmission through sharp bends in photonic crystal waveguides," *Phys. Rev. Lett.*, Vol. 77, pp. 3787−3790, 1996.

[11] H. Altug and J. Vuckovic, "Two-dimensional coupled photonic crystal resonator arrays," *Appl. Phys. Lett.*, Vol. 84, pp. 161−163, 2004.

[12] A. Baldycheva, V. A. Tolmachev, T. S. Perova, Y. A. Zharova, E. V. Astrova, and K. Berwick, "Silicon photonic crystal filter with ultrawide passband characteristics," *Opt. Lett.*, Vol. 36, pp. 1854−1856, 2011.

[13] J. J. Baumberg, N. M. B. Perney, M. C. Netti, M. D. C. Charlton, M. Zoorob, and G. J. Parker, "Visible-wavelength super-refraction in photonic crystal superprisms," *Appl. Phys. Lett.*, Vol. 85, pp. 354−356, 2004.

[14] S. W. Leonard, H. M. van Driel, J. Schilling, and R. B. Wehrspohn, "Ultrafast band-edge tuning of a two-dimensional silicon photonic crystal via free-carrier injection," *Phys. Rev. B*, Vol. 66, pp. 161102−1−4, 2002.

[15] F. Qin, Y. Liu, Z. Meng, and Z-Y. Li, "Design of Kerr-effect sensitive microcavity in nonlinear photonic crystal slabs for all-optical switching," *J. Appl. Phys.*, Vol. 108, pp. 053108−1−7, 2010.

[16] M. A. Dundar, B. Wang, R. Notzel, F.Karouta, and R. W. van der Heijden, "Optothermal tuning of liquid crystal infiltrated InGaAsP photonic crystal nanocavities," *J. Opt. Soc. Am. B*, Vol. 28, pp. 1514−1517, 2011.

[17] B. Maune, M. Loncar, J. Witzens, M. Hochberg, T. Baehr-Jones, D. Psaltis, and A. Scherer, "Liquid-crystal electric tuning of a photonic crystal laser," *Appl. Phys. Lett.*, Vol. 85, pp. 360−362, 2004.

[18] D. Erickson, T. Rockwood, T. Emery, A. Scherer, and D. Psaltis, "Nanofluidic tuning of photonic crystal circuits," *Opt. Lett.*, Vol. 31, pp. 59−61, 2006.

[19] M. Mohageg and L. Maleki, "Reconfigurable optical spectra from perturbations on elliptical whispering gallery resonances," *Opt. Express*, Vol. 16, pp. 2037−2047, 2008.

[20] C. H. Huang, H. F. Chou, and J. E. Bowers, "Dynamically reconfigurable optical packet switch (DROPS)," *Opt. Express*, Vol. 14, pp. 12008−12014, 2006.

[21] M. Lacolle, H. Sagberg, I. R. Johansen, O. Lovhaugen, O. Solgaard, and A. S. Sudbo, "Reconfigurable near-infrared optical filter with a micromechanical diffractive fresnel lens," *IEEE Photonic. Tech. Lett.*, Vol. 17, pp. 2622−2624, 2005.

[22] S. Iwamoto, S. Ishida, Y. Arakawa, M. Tokushima, A. Gomyo, H. Yamada, A. Higo, H. Toshiyoshi and H. Fujita, "Observation of micromechanically controlled tuning of photonic crystal line-defect waveguide," *Appl. Phys. Lett.*, Vol. 88, pp. 011104−1−3, 2006.

[23] T.Takahata, K. Matsumoto, and I. Shimoyama, "A wide wavelength range optical switch using a flexible photonic crystal waveguide and silicon rods," *J. Micromech. Microeng.*, Vol. 20, pp. 075009−1−6, 2010.

[24] S. M. C. Abdulla, L. J. Kauppinen, M. Dijkstra, E. Berenschot, M. J. de Boer, R. M. de Ridder, and G. J. M. Krijnen, "Mechano-optical switching in a MEMS integrated photonic crystal slab waveguide," *The 24th IEEE International Conference on Micro Electro Mechanical Systems*, pp. 9−12, 2011.

[25] W. Suh, M. F. Yanik, O. Solgaard, and S. Fan, "Displacement-sensitive photonic crystal structures based on guided resonance in photonic crystal slabs," *Appl. Phys. Lett.*, Vol. 82, pp. 1999−2001, 2003.

[26] W. Suh and S. Fan, "Mechanically switchable photonic crystal filter with either all-pass transmission or flat-top ref lection characteristics," *Opt. Lett.*, Vol. 28, pp. 1763−1765, 2003.

[27] W. Park and J. B. Lee, "Mechanically tunable photonic crystal structure," *Appl. Phys. Lett.*, Vol. 85, pp. 4845−4847, 2004.

[28] W. Zhou, D. M. Mackie, M. Taysing-Lara, G. Dang, P. G. Newman, and S. Svensson, "Novel reconfigurable semiconductor photonic crystal-MEMS device," *Solid-State Electron.*, Vol. 50, pp. 908−913, 2006.

[29] T. Takahata, K. Hoshino, K. Matsumoto, and I. Shimoyama, "Transmittance tuning of photonic crystal reflectors using an SPM cantilever," *Sens. Actuat. A*, Vol. 128, pp. 197−201, 2006.

[30] I. Marki, M. Salt, and H. P. Herzig, "Tuning the resonance of a photonic crystal microcavity with an AFM probe," *Opt. Express*, Vol. 14, pp. 2969−2978, 2006.

[31] B. Cluzell, L. Lalouat, P. Velha, E. Picard, D. Peyrade, J. C. Rodier, T. Charvolin, P. Lalanne, F. de Fornel, and E. Hadji, "A near-field actuated optical nanocavity," *Opt. Express*, Vol. 16, pp. 279−286, 2008.

[32] D. Mao, P. Liu, K.-M. Ho, and L. Dong, "A theoretical study of a nano-opto-mechanical sensor using a photonic crystal-cantilever cavity," *J. Opt.*, Vol. 14, pp. 075002−1−8, 2012.

[33] A. F. Oskooi, D. Roundy, M. Ibanescu, P. Bermel, J. D. Joannopoulos, and S. G. Johnson, "MEEP: A flexible free-software package for electromagnetic simulations by the FDTD method," *Comput. Phys. Commun.*, Vol. 181, pp. 687−702, 2010.

[34] V. A. Mandelshtam and H. S. Taylor, "Harmonic inversion of time signals and its applications," *J. Chem. Phys.*, Vol. 107, pp. 6756−6769, 1997.

[35] T. Yoshie, J. Vuckovic, A. Scherer, H. Chen and D. Deppe, "High quality two-dimensional photonic crystal slab cavities," *Appl. Phys. Lett.*, Vol. 79, pp. 4289−4291, 2001.

[36] J. Vuckovic, M. Loncar, H. Mabuchi, and A. Scherer, "Optimization of the Q factor in photonic crystal microcavities," *IEEE J. Quantum Elect.*, Vol. 38, pp. 850−856, 2002.

[37] Y. Akahane, T. Asano, B. Song, and S. Noda, "High-Q photonic nanocavity in a two-dimensional photonic crystal," *Nature*, Vol. 425, pp. 944−947, 2003.

[38] Y. Tanaka, T. Asano, and S. Noda, "Design of photonic crystal nanocavity with Q-factor of ~10^9," *J. Lightwave Technol.*, Vol. 26, pp. 1532−1539, 2008.

[39] K. Rivoire, S. Buckley, and J. Vuckovic, "Multiply resonant high quality photonic crystal nanocavities," *Appl. Phys. Lett.*, Vol. 99, pp. 013114−1−3, 2011.

[40] E. Eleftheriou, T. Antonakopoulos, G. K. Binnig, G. Cherubini, M. Despont, A. Dholakia, U. Dürig, M. A. Lantz, H. Pozidis, H. E. Rothuizen, and P. Vettiger, "Millipede - a MEMS-based scanning-probe data-storage system," *IEEE T. Magn.*, Vol. 39, pp. 938−945, 2003.

[41] P. Vettiger, G. Cross, M. Despont, U. Drechsler, U. Dürig, B. Gotsmann, W. Haberle, M. A. Lantz, H. E. Rothuizen, R. Stutz, and G. K. Binnig, "The "millipede" - nanotechnology entering data storage", *IEEE. T. Nanotechnol.*, Vol. 1, pp. 39−55, 2002.

[42] M.R. Douglass, "Lifetime estimates and unique failure mechanisms of the Digital Micromirror Device (DMD)," *The 36th Annual. IEEE International Reliability Physics Symposium Proceedings*, pp. 9−16, 1998.

CHAPTER 7. CONCLUSIONS AND FUTURE WORK

Nowadays high-speed silicon PICs have become strong candidates to replace many electronic ICs. As mentioned in Chapter 1, PCs play a key role in nanophotonics and high tunability and programmability are needed to expand applications of silicon PICs in the next-generation photonics. The main objective of this thesis is to develop several SOI-based reconfigurable and programmable PC devices.

In Chapter 2, we developed a relatively general nanofabrication process for integrating PC devices with movable mechanical components on SOI wafers. The process allowed us to release nanoscale mechanical structures while anchoring PC structures on the buried oxide layer of a SOI wafer. We also investigated grating coupling technology to facilitate coupling light into and out of the photonic chips.

In Chapter 3, we developed an all-optical programmable PC device that integrates DMD, photo-responsive LCs, and PC technologies together. Periodic air holes in a PC slab are infiltrated with photo-responsive LCs. Refractive index of each hole is individually modulated by light patterns projected from DMD. We demonstrated the functionality and programmability of the device by forming a point-defect cavity, a straight waveguide, and a waveguide bend on the single device. Future work includes realizing more complex photonic functions, such as add-drop filters and programmable lasers, on this PC platform.

In Chapter 4, we developed two reconfigurable PC devices that integrate optical nanobeam and NEMS technologies. The first device consists of an array of movable nanobeams. Each nanobeam is an electrostatically tunable photonic element in a PC waveguide. We both theoretically and experimentally demonstrated the capability of the device to tune its photonic bandgap, by tuning one unit in group of two neighboring

nanobeam units, tuning one or two in group of three units, and forming two reconfigurable PCs together. To achieve a higher-level integration, we also studied another reconfigurable PC integrating an array of mechanical tunable nanobeams with an array of fixed pillars into the top silicon layer of a SOI wafer. Theoretical analysis of bandgap engineering for this reconfigurable PC was conducted. Future work includes fabricating and characterizing this device.

In Chapter 5, we developed two tunable PC^3 resonators. The first device has an NEMS cantilever embedded into a L6 cavity in a PC slab, while the second device inserts a similar cantilever into a nanobeam-base waveguide. We studied the bending characteristic of the cantilever and the optical characteristics of these devices at different applied voltages. A maximum resonance wavelength shift of 15 nm and 13.5 nm is obtained for the L6 PC^3 and the nanobeam-based PC^3, respectively, at an applied voltage of 97 V. In the future we will use the PC^3 devices for biosensor applications.

In Chapter 6, we conducted theoretical investigation on a nano-opto-mechanical reconfigurable PIC device consisting of an array of silicon plugs and a 2D PC slab. We assume that each plug could be individually introduced into its corresponding air hole in the PC slab. We theoretically demonstrated that a point-defect cavity, a line-defect waveguide, and a waveguide bend can be configured in the PC slab, by inserting different plugs into an air hole, a straight line of holes, and an L-shape line of holes. This theoretical study will benefit our efforts toward realizing a fully reconfigurable PIC platform. Future work includes designing and fabricating an actuator for individual control of plugs, and then, integrating the actuator and a PC slab to realize this device.